STUDY OF SPIN-DEPENDENT TRANSITIONS AND SPIN COHERENCE AT THE (111) ORIENTED PHOSPHOROUS DOPED CRYSTALLINE SILICON TO SILICON DIOXIDE INTERFACE USING PULSED ELECTRICALLY DETECTED MAGNETIC RESONANCE

by

Seoyoung Paik

A dissertation submitted to the faculty of
The University of Utah
in partial fulfillment of the requirements for the degree of

Doctor of Philosophy

in

Physics

Department of Physics and Astronomy

The University of Utah

December 2011

The University of Utah Graduate School

STATEMENT OF DISSERTATION APPROVAL

The dissertation of **Seoyoung Paik**

has been approved by the following supervisory committee members:

Christoph Boehme	, Chair	**Aug 26, 2011** Date Approved
Z. Valy Vardeny	, Member	**Aug 26, 2011** Date Approved
Yong-Shi Wu	, Member	**Aug 26, 2011** Date Approved
Stephan LeBohec	, Member	**Aug 26, 2011** Date Approved
Debra J. Mascaro	, Member	**Aug 26, 2011** Date Approved

and by **David Kieda** , Chair of

the Department of **Physics and Astronomy**

and by Charles A. Wight, Dean of The Graduate School.

ABSTRACT

A study of spin-dependent electronic transitions at the (111) oriented phosphorous doped crystalline silicon (c-Si) to silicon dioxide (SiO_2) interface is presented for $[^{31}P] = 10^{15}$ cm^{-3} and $[^{31}P] = 10^{16}$ cm^{-3} and a temperature range between $T \approx 5$K and $T \approx 15$K.

Using pulsed electrically detected magnetic resonance (pEDMR), spin-dependent transitions involving ^{31}P donor states and two different interface states are observed, namely (i) P_b centers which can be identified by their characteristic anisotropy and (ii) the E' center which is attributed to defects of the near interface SiO_2 bulk. Correlation measurements of the dynamics of spin-dependent recombination confirm that previously proposed transitions between ^{31}P and the interface defects take place. The influence of these near interface transitions on the ^{31}P donor spin coherence time T_2 as well as the donor spin-lattice relaxation time T_1 is then investigated by comparison of spin Hahn echo decay measurements obtained from conventional bulk sensitive pulsed electron paramagnetic resonance and surface sensitive pEDMR measurements, as well as surface sensitive electrically detected inversion recovery experiments.

The measurements reveal that the T_2 times of both interface states and ^{31}P donor electrons spins in proximity of them are consistently shorter than the T_1 times, and both T_2 and T_1 times of the near interface donors are reduced by several orders of magnitude from those in the bulk, at $T \leq 13$ K. The T_2 times of the ^{31}P donor electrons are in agreement with the prediction by De Sousa that they are limited by interface defect-induced field noise.

To further investigate the dynamic properties of spin-dependent near interface processes, electrical detection of spin beat oscillation between resonantly induced spin-Rabi nutation is conducted at the phosphorous doped (10^{16}cm^{-3}) Si(111)/SiO_2 interface. Predictions of Rabi beat oscillations based on several different spin-pair

models are compared with measured Rabi beat nutation data. Due to the g-factor anisotropy of the P_b center (a silicon surface dangling bond), one can tune intra-pair Larmor frequency differences (Larmor separations) by orientation of the crystal with regard to an external magnetic field. Since Larmor separation governs the number of beating spin-pairs, crystal orientation can control the beat current. This is used to identify spin states that are paired by mutual electronic transitions.

Based on the agreement between hypothesis and data, the experiments confirm the presence of the previously observed ^{31}P-P_b transition and the previously hypothesized P_b to near interface SiO_2 bulk state (E' center) transition.

For my husband, Sang-Yun

CONTENTS

ABSTRACT . . . . . **iii**

LIST OF FIGURES . . . . . **ix**

LIST OF TABLES . . . . . **xv**

ACKNOWLEDGEMENTS . . . . . **xvi**

CHAPTERS

1. ELECTRON SPINS AT THE *c*-Si(111)/SiO_2 INTERFACE **1**

1.1 Introduction 1
1.2 The *c*-Si(111)/SiO_2 interface structure 3
1.2.1 Point defects in the interface: P_b center and E' center 3
1.3 Spin-dependent recombination at the *c*-Si/SiO_2 interface 5
1.4 Identification of spin-dependent interface transitions 6
1.5 Experimental details 9
1.5.1 Experimental confirmation of spin-dependent interface processes 11
1.6 References 15

2. IDENTIFICATION OF DANGLING BOND DEFECTS **18**

2.1 *g*-factor anisotropy of P_b center 18
2.1.1 Experimental data 18
2.1.2 Discussion 20
2.2 Identification of ^{31}P to interface-defect transitions 22
2.2.1 Experimental data 22
2.2.2 Discussion 25
2.3 References 27

3. T_1 AND T_2 COHERENCE TIMES OF ELECTRON SPINS AT THE *c*-Si/SiO_2 INTERFACE **28**

3.1 Electrical detection of spin coherence 28
3.1.1 Discussion 30

3.2 Comparison of the coherence time T_2 of ^{31}P donor electrons at the c-Si:P/SiO_2 interface and in the c-Si:P bulk . . . 31
3.2.1 pEDMR and pEPR-detected spin echoes . . . 31
3.2.2 Measurement of spin-echo decays . . . 34
3.2.2.1 Temperature dependence of T_2 times . . . 36
3.2.2.2 Discussion . . . 39
3.2.3 Comparison of T_2 and the longitudinal relaxation time T_1 of ^{31}P donor electrons at the c-Si:P/SiO_2 interface . . . 40
3.2.3.1 Electrical detection of spin inversion . . . 40
3.2.3.2 Inversion recovery of near interface defect ^{31}P donor electrons . . . 43
3.2.3.3 Discussion . . . 43
3.2.4 Comparison of T_2 and T_1 times at different interface defect densities and different pair-partner resonances . . . 45
3.2.4.1 Testing the independence of T_1 and T_2 relaxation times . . . 45
3.2.4.2 Discussion . . . 49
3.3 Conclusions . . . 49
3.4 Summary . . . 51
3.5 References . . . 53

4. ELECTRICALLY DETECTED CRYSTAL ORIENTATION DEPENDENT SPIN-RABI BEAT OSCILLATION OF c-Si(111)/SiO_2 INTERFACE STATES . . . 54

4.1 Experimental details . . . 54
4.2 Spin g factor distributions in the interface . . . 55
4.3 Electrically detected spin-Rabi beat effect . . . 57
4.3.1 FFT of Rabi beat nutation data . . . 57
4.4 Orientation dependence of spin-Rabi beating . . . 60
4.4.1 Predictions and pair transition models . . . 62
4.4.2 Comparison and discussions . . . 62
4.5 Conclusion . . . 65
4.6 References . . . 66

APPENDICES

A. THEORETICAL AND TECHNICAL FOUNDATIONS OF PULSED EDMR EXPERIMENTS . . . 67

B. ELECTRICAL DETECTION OF SPIN-RABI BEATING . . . 77

C. FIT PROCEDURE FOR LIGHTLY CONVOLUTED PEDMR SPECTRA 85

LIST OF PUBLICATIONS 88

LIST OF FIGURES

1.1 Ball and stick illustration of the atomic composition of the c-Si(111)/SiO_2 interface. (a) The ^{31}P donor state (large green shaded circle) is significantly larger than the P_b center. Exchange coupling between the two states is possible when they are sufficiently close to each other. The orientation of the interface is defined by the angle between the externally applied B_0 magnetic field and the (111) crystal axis which is perpendicular to the crystal surface. (b) Sketch of P_b defect center. P_b electron is localized on a silicon atom back bonded to three other silicon atoms. The main axis of the p-component of the P_b electron is perpendicular to the (111) interface.(c) Sketch of the dangling bond E' center localized on a silicon atom back bonded to three oxygen atoms. (d) Schematic diagram of a positively charged E' center, a hole trapped at an oxygen vacancy. 4

1.2 Band sketch illustrating the spin-dependent $^{31}P/P_b$ charge-carrier recombination transition. For details see the text. 7

1.3 Experimental setup and structure of the sample. (a) Experimental setup for pulsed EDMR experiments. It consists of a Bruker Elexsys E580 EPR spectrometer, an Oxord helium flow cryostat, a helium transfer tube, electronics for the application and detection of transient currents and an ultraviolet and infrared filtered spectral light source. (b) Picture of the Bruker Elexsys E580 EPR facility. (c) PEDMR sample connector, which consists of a printed circuit board (PCB) for the electric contact with the sample and a brass holder needed for geometric sample alignment. (d) Photo of the c-Si pEDMR sample. (e) Microscope picture of the c-Si resistor strcuture using an interdigitated grid system. Aluminum wires with $\sim 10\mu$m width are deposited between the 2 mm $\times$ 3 mm c-Si(111)/SiO_2 sample areas. 10

1.4 Plots of the microwave pulse (at $t = 0$) induced change ΔI of an interface photocurrent along a c-Si(111):P/sio interface as a function of time t and the applied magnetic field B_0. (a,c) Plots of ΔI as functions of B_0 for the times $t = 6.1$ μs and $t = 38$ μs, respectively, for which a quenching and an enhancement of the current changes reach their extrema. (b) Color contour plot of the entire data set $\Delta I(t, B_0)$ containing the data of the plots in (a), (c) and (d). (d) Plot of ΔI as a function of the time t for a magnetic field $B_0 = 350.5$ mT which was on resonance with the high field Phosphorous EPR line. 12

2.1 Crystal orientation dependencies of the g-factor distributions of electron spins in c-Si(111)/SiO_2 interface. (a) Plots of ΔI as functions of B_0 at arbitrary times t after a microwave pulse with arbitrary length τ, frequency $f \approx 9.5\ GHz$ and a power $P = 8$ W and under otherwise identical conditions as for the data in Fig. 1.4. The data were collected for five sample orientations θ and two ^{31}P concentrations. The displayed plots are normalized to the maximum of ΔI. The solid lines represent fits of the data consisting of four Gaussian peaks, two related to the ^{31}P hyperfine line and two peaks related to interface defects. The plot for $[^{31}\mathrm{P}] = 10^{16}\mathrm{cm}^{-3}$ and $\theta = 90°$ has the peak assignments to the low field (LF) and high field (HF) ^{31}P resonances, the P_b peak as well as peak 2. (b) Plots of the fit results of the g-factors for the two interface defect lines as a function of θ for the two ^{31}P concentrations. The solid lines indicate the literature values for the P_b center. 19

2.2 Plots of the zero crossing times τ_0 of magnetic resonantly induced photocurrent transients of the ^{31}P low or high field resonance (τ_0^A) versus the zero crossing times of magnetic resonantly induced current transients of the P_b/E' center resonances (τ_0^B) measured for a variety of different samples and sample conditions (temperature, offset current, illumination). The solid line is a linear function through the origin with slope 1. The two plots made for the two concentrations show a strong correlation of the zero crossing times of all three resonances. 24

3.1 Electrically detected spin-Rabi nutations. (a) Plot of the measured integrated charge $Q(\tau, B_0)$ as defined by Eq. (3.1) as a function of the magnetic field B_0 and the length τ of an applied microwave pulse with frequency $f = 9.7475$ GHz and power $P = 8$ W. (b) The symbols represent a plot of the measured charge $Q(\tau)$ for four different microwave powers at $B_0 = 347$ mT. Note that for the latter case, the pulse length was recorded up to $\tau = 120$ ns only as the measurement was limited by signal perturbation due to the pulse-induced microwave current artifacts. The blue lines represent fits of an integrated Bessel function to the experimental data. The Rabi-nutation frequencies obtained from these fits are displayed in the inset as a function of the applied B_1 field. The fit of a linear function through the origin (black line) shows good agreement. 29

3.2 Comparison of (a) an electrically detected spin-echo with $\tau = 300$ ns and (b) a conventional microwave detected Hahn echo with $\tau = 10$ μs. The data sets were recorded on the same sample, under identical sample conditions (T= 10 K, $I = 250$ μA, $\theta = 90°$) during the same experimental run on resonance with the low field phosphorous line. Both data sets were fit with Gaussian functions (solid line). Insets of the two plots show sketched timelines of the used pulse sequences. 32

3.3 Plot of integrated intensities of the electrically detected echoes as a function of 2τ recorded with pEDMR on a c-Si:P/SiO_2 sample with [P] = 10^{16} cm^{-3} on resonance with the low field ^{31}P line. The solid line represents a fit with a modified multi-exponential decay function (see text), the small inset plots represent plots of echo data sets. 35

3.4 Plot of the normalized integrated echo intensity of pEPR and pEDMR detected Hahn echoes as a function of the logarithms of the pulse separation time τ for various temperatures. The data sets were fit with the modified exponential function given by Eq. (3.3). All pEDMR and pEPR measurements were conducted on the same samples during the sample experimental run. Most of the data points were recorded on resonance with the low field phosphorous line except for the blue colored data points which were recorded on resonance with the low field phosphorous line. 37

3.5 Plot of the logarithm of coherence decay rate T_2^{-1} obtained from the data shown in Fig. 3.4 as a function of the inverse temperature T^{-1}. The solid lines are fits of the data. The pEDMR data are fit with a constant function. The pEPR is fit with a combination of a constant function and a temperature-activated Boltzmann factor. 38

3.6 Demonstration of an electrically detected spin inversion recovery experiment. The inset is a sketch of the inversion recovery pulse sequence which consists of the Hahn echo sequence that is preceded by an inversion (π-) pulse at a time τ'' before the Hahn echo sequence begins. Similar to the electrically detected Hahn echo shown in Fig. 3.2, a projection pulse is shifted through the sequence during different repetitions of the experiment. The main plot displays an echo recorded by plotting Q as a function of the difference $\tau' - 2\tau$ between the projection pulse begin τ' and the echo maximum at 2τ. 42

3.7 Plot of the integrated echo intensity detected with the pulse sequence shown in Fig. 3.6 as a function of the inversion recovery time τ''. The solid line represents a fit of the data with a single exponential function. Note that the inverted echo for small τ'' changes into a noninverted echo with equal magnitude for large τ''. The inset plots on the left show the raw data of the various echo measurements as well as fits with Gaussian functions which are the basis for the integrated echo intensities. 44

3.8 Electrically detected inversion recovery measurements of electron spins on the low field $^{31}P/P_b$ resonance and the high field ^{31}P resonance measured on an annealed sample at T = 5K. The values of τ'' are listed next to the plotted echoes. The data are normalized to the echo measured with large τ''. Within the given error ranges, the two data inversion recovery plots show similar T_1 time. This T_1 times are increased in comparison to the T_1 time of the nonannealed sample. 47

3.9 The results of electrically detected Hahn echo decay measurements of electrons spins at on the low field $^{31}P/P_b$ resonance and the high field ^{31}P resonance measured on an annealed sample at temperature between $T = 5K$ and $T = 12K$. 48

4.1 Atomic structure of the c-Si(111)/SiO_2 interface and the resultant spin-Rabi beat nutations. (a) Sketch of the atomic scale structure of the c-Si(111)/SiO_2 interface. The ^{31}P donor state (large green shaded circle) is significantly larger than the highly localized dangling bond defect states (blue balloons:P_b centers, purple balloons:E' centers). The orientation of the interface is defined by the angle between the externally applied B_0 magnetic field and the (111) crystal axis which is perpendicular to the crystal surface. (b) Electrically detected g-factor spectra of c-Si(111):P/SiO_2, measured at $\theta = 90°$ in temperature 5 K. Blue arrow represents that P_b resonance (blue line) shifts at different interface orientations. (c) Each linear plot represents B_1 field dependence of Rabi frequency of spin $\frac{1}{2}$(blue) and spin 1(red). Five plots of FFT (fast fourier transformation) of Rabi oscillation as a function of charge Q and Rabi frequency f_{Rabi}, which are measured with different B_1 field strengths. Solid curves in each plot are fit curves for spin $\frac{1}{2}$(blue) and spin 1 (red). 56

4.2 g-factor dependence of FFT of spin-Rabi oscillations measured at (a) 0° (upper) and (b) 90° (below) interface orientation. The plots present charge Q as a function of Rabi frequency (normalized by $\frac{2\pi}{\gamma B_1} f_{Rabi}$) and g-factors. Inset plots show the pEDMR spectra measured at each orientation (0° and 90°), in which one blue line, three green lines are Gaussian functions to fit data and the red line is resultant fit curve. 1.6 mT in (a) and 0.3mT in (b) represent Larmor separations between ^{31}P and P_b spins at 0° and at 90°. 58

4.3 FFTs of spin-Rabi oscillations measured at different orientations (0°, 14°, 43°, 65°, 73° and 90°) with same B_1 field strength.(B_1= 0.54(2) mT) Each Rabi oscillation is measured on the B_0 field where the Rabi beating signal is maximized. The black solid lines demonstrate final fit curves while the blue and red lines represent fit curve for spin 1/2 Rabi nutation and for spin 1, beat nutation. 61

4.4 Black dots show measured g-factors of spin-Rabi beat oscillations as a function of interface orientations. Each solid line represents literature g-factors of ^{31}P, P_b and E' defect, while red plot represents g-factors predicted based on the ^{31}P-P_b spin-pair transitions and blue plot shows g-factor predictions of P_b-E' pair transitions. 63

4.5 Fractions of beating spins in the excited spin-pairs. Black dots represent fraction of beating spin in the measured Rabi oscillation data at different orientations. Red plot shows the fraction of beating spins from the predicted spin-Rabi oscillation by ^{31}P-P_b pair transitions, while blue plot shows the predictions of beating spin fraction by P_b-E' pair transitions and green plot represents the prediction of ^{31}P-E' spin-pair transitions in the interface. 64

A.1 Sketch of the intermediate pair recombination model by Kaplan, Soloman, and Mott (KSM). The sketch illustrates triplet or singlet densities among the spin-pair ensemble which are influenced by constant generation rates G_t and G_s, respectively, and two different pair annihilation processes, namely recombination with recombination probabilities r_t, r_s and pair dissociation into free charge carriers with probabilities d_t and d_s. [1, 2]. Interactions of spin-pairs with their environment can cause spin-relaxation, also called spin mixing or intersystem-crossing (ISC, with rate k_{ISC}). 68

A.2 The experimental setup for pEDMR and pODMR experiments. (a) Schematic diagram of the optical setup. (b) Fiber bundle and the PCB sample holder with mirror. (c) Cross-sectional diagram of fiber bundle. (d), (e) Fiber bundle as aligned in the channel of the PCB. 72

A.3 PCB design for pEDMR and pODMR experiments. The PCB of pEODMR probehead consists of three different PCB layers which are called top PCB, bottom PCB (1) and bottom PCB (2). For pEDMR or pODMR experiments, the sample is placed between the top PCB and the bottom PCB (1). The top PCB has an extension with a small mirror (on the right side in the figure) to attach an optical fiber bundle. Two pairs of metal pads and thin silver wires for electric circuit combination are located on the surfaces of the top and bottom PCBs. The bottom PCB (2) is made to support the sample and the other PCBs. It is connected by four screws to the brass holder of the probehead. 73

A.4 Assembling procedure of EODMR sample holder, which is combined with three kinds of PCBs and a tuning fork shaped brass part. For details see text. 75

B.1 Rabi-beat nutation (a) B_0 field spectrum of c-Si(111)/SiO_2 interface. Grey colored Lorentzian line represent excitation B_1 field. The weak B_1 field excites small portion of spins inside the line area. (b) Strong B_1 field excitation. (c) Conceptual sketch of spin-Rabi nutation for the weakly coupled spin-pair. With weak B_1 field excitation, only a spin in the pair nutates with Rabi frequency. (d) Both spins in the pair are excited at the same time by the strong B_1 field (spin beating). (e) Evolution of spin orientations during B_1 pulse excitation and electrically measured recombination current for the weak B_1 field and (f) for the strong B_1 field. 78

B.2 Plot of the fraction of spin-pairs exhibiting spin-Rabi beating as a function of B_1. The blue dots represent the fractions of pairs which do not exhibit beating, the red dots represent the fractions of spin-pairs which do exhibit beating. The blue and red solid lines show the predicted values for the respective spin-pair fractions based on the g-factor distributions. 83

C.1 Black dots display measured g-factors where a maximal spin-Rabi beat oscillation is observed, as a function of the interface orientation. Each solid line represents literature g-factors of ^{31}P, P_b and E' defect, respectively. The red plot represents g-factors predicted by the ^{31}P-P_b transition, the blue plot represents g-factors predicted by the P_b-E' transition. 87

LIST OF TABLES

3.1 Expectation for the observed time constants in electrically detected inversion-recovery and Hah-echo experiments for a number of different relationships between the T_1, T_2 and electronic transition times. We note that in the main text, the expected results are refereed to as T_1 and T_2, respectively, even when they may be due to electronic transitions. 41

3.2 PEDMR detected inversion recovery times (T_1) and Hahn echo decay times (T_2) recorded on the high and low field resonances at a temperature $T = 5$K for both the nonannealed (native) and the annealed silicon-to-silicon dioxide interface. 50

ACKNOWLEDGEMENTS

I would like to express my gratitude to the people who have been my mentors, advisor, and colleagues during my Ph.D. studies. I appreciate my great adviser, Christoph Boehme. He guided me in the research with professional knowledge of science and with passion. Especially, whenever I faced hard obstacles in research, he encouraged me and made me redouble efforts to overcome them. I am deeply impressed that he is entirely devoted to his family and impressed by how much he finds it a pleasure to work very hard in physics, often harder than anyone else.

Dr. Dane McCamey, who had been a postdoctoral researcher in Christoph Boehme's group, was a colleague and a mentor for me, providing a lot of help in research to me who had just begun Ph.D. studies. Since he usually showed us various ideas and great imagination in discussions, we could accomplish excellent academic achievements together while he stayed in Utah.

Sang-Yun Lee, one of my best colleagues and my beloved husband, has always worked with me whenever I had to sit up for very long experiments. It was a great fortune that I could work with him, since the strong partnership in the research made us much more productive. We collaborated on much research about *c*-silicon, organic semiconducting materials, and the pEODMR experimental setup. He has excellent talents on mathematical calculation and computer programming, which helped us to solve many difficult problems in the research. Also, he faithfully supported me as my husband whenever I passed through the hard paths of life.

Prof. Valy Vardeny, Prof. Yong-Shi Wu, Prof. Stephan Lebohec, and Prof. Debra J. Mascaro have gladly participated in my supervisory committee and provided me with advice.

Willian Baker, one of my colleagues, made a contribution for the study of spin coherence time at the *c*-Si(111)/SiO_2 interface and the building of a new sample holder for pEODMR experiments.

Eric Sorte, a friend who works in Prof. Brian Saam's group, helped me handle the LaTeX program for writing this thesis.

Finally, I would like to thank my parents who have supported me with great love.

CHAPTER 1

ELECTRON SPINS AT THE *c*-Si(111)/SiO_2 INTERFACE

The following three chapters (Chapters 1 to 3) are based on a journal article published in Physical Review B in the year 2010 coauthored by Seoyounng Paik, Sang-Yun Lee, William J. Baker, Dane R. McCamey, and Christoph Boehme.[1] Chapter 4 is then an extension of this work which addresses the question of whether spin-dependent electronic transitions other than the known ^{31}P-P_b transitions are present at the *c*-Si/SiO_2 interface and whether these transitions are potentially suitable for the coherent spin-readout too.[2]

1.1 Introduction

Due to their technological importance, the properties of phosphorous (^{31}P) donors in crystalline silicon have been investigated extensively for more than half a century. During this time, magnetic resonance-based methods have revealed many aspects of the microscopic nature of ^{31}P as well as the electronic processes in which it is involved. Since the first mapping of a donor wavefunction using electron nuclear double resonance spectroscopy [1], a large and diverse amount of information regarding the electronic and quantum mechanical properties of such systems has been reported [2].

This wealth of information has contributed to the technological exploitation of silicon to the extent that it has become the most widely utilized semiconductor in the global electronics industry. However, even with all the information regarding

[1]Reprinted with permission from [S.-Y. Paik, S.-Y. Lee, W. J. Baker, D. R. McCamey, and C. Boehme, Physical Review B 81 (7), 075214 (2010)]. Copyright 2010 by the American Physical Society.

[2]This work is currently submitted for publication and has been coauthored by Seoyoung Paik, Sang-Yun Lee, Dane R. McCamey, and Christoph Boehme.

silicon available to us, there are still questions regarding the ability to exploit the quantum mechanical nature (specifically spin) of dopants and charge carriers for technological applications such as spin transistors [3] or quantum computers [4], the latter of which are proposed to utilize electron or nuclear spins of phosphorus donors in silicon as quantum bits. While there has been significant experimental effort toward the implementation of these and other concepts [5], challenges remain in a number of different areas, the most pressing being the difficulty in detecting the spin of individual donors without reducing its quantum memory time (the coherence time, T_2) [6]. Nevertheless, donors in silicon retain promise in this area due to their extremely long phase coherence times, with T_2 exceeding 60 ms for the electron spin [7] and 1 second for the nuclear spin [8] at liquid He temperatures.

Many of the recent schemes for silicon-based spin or quantum devices involve electronic processes occurring at or near interfaces, particularly the (111) oriented phosphorous doped crystalline silicon to silicon dioxide (c-Si(111)/SiO_2) interface. This presents advantages since locating spins near interfaces allows them to be controlled with surface gates [4], and detected with surface electronics [9–13]. However, it may also lead to a decrease in spin coherence due to the spin-spin interactions with surface states [14, 15], as well as to the loss of quantum information following spin-dependent recombination through surface states. Since it is not possible to obtain defect free c-Si(111)/SiO_2 interfaces [16] (we note that work is currently being undertaken to obtain defect free interfaces using H-termination but it is in the early stages [17, 18]), the understanding of interface electron and spin transitions has become important.

While interfaces and interface defects have a detrimental effect on coherence times of near interface spin-qubits, they may also have a benefit for quantum devices: It has been proposed to use interface defects as probe spins to readout [9] single donor ^{31}P spin states. This idea is based on bringing a highly localized, energetically lower, paramagnetic probe state into the vicinity of the ^{31}P donor spin [9]. Since the first experimental demonstration of this readout approach by Stegner et al. [10] using c-Si/SiO_2 interface dangling bonds (P_b states), many experimental studies have been performed which corroborated its extraordinary sensitivity [19], the physical nature

of the donor-interface spin-pair states [20], the ability to use this electrical readout approach for donor nuclear spin readout via hyperfine interactions [21]. As a result of these studies, the existence and nature of the ^{31}P-P$_b$ transition is known and understood; however, the exact role of other interface and other near interface states as well as spin-relaxation limitations imposed on ^{31}P qubits due to the spin-dependent electronic readout transitions and magnetic noise of the interface defects has remained mostly elusive.

In the following, pulsed electrically detected magnetic resonance (pEDMR) and pulsed electron paramagnetic resonance (pEPR) measurements performed on (111) surface oriented *c*-Si samples with [P]=10^{15} cm^{-3} and [P]=10^{16} cm^{-3} at temperatures between $T = 5$ K and $T = 15$ K are presented. The data were collected in order to elucidate the nature of spin-dependent electronic interface transitions involving ^{31}P donor and interface states and to then determine how these processes influence the coherence time of the ^{31}P donor electron spins in proximity of these interface defects. The latter was accomplished by comparison of the interface sensitive pEDMR measurements to bulk sensitive pEPR measurements of ^{31}P donors. Our results are discussed with regard to their implications for the ability of spin qubit readout using interface defect probe spins whilst maintaining long coherence times.

The key questions motivating this study are centered about ^{31}P qubit coherence times. It follows an extensive number of previous EPR [22–28], EDMR [10, 19, 28–30], and pEDMR [31–33] studies carried out on various *c*-Si(111)/SiO$_2$ interface defects as well as electronic trapping and recombination processes of interfaces with different surface orientations and ^{31}P doping concentrations. Most of these studies aimed to enhance the understanding of electronic processes relevant for materials systems used in conventional *c*-Si-based microelectronics and photovoltaic devices. Thus, the study presented here may also be of relevance for conventional silicon technologies.

1.2 The *c*-Si(111)/SiO$_2$ interface structure

1.2.1 Point defects in the interface: P$_b$ center and E' center

Fig. 1.1 shows the atomic-scale structure of the *c*-Si(111)/SiO$_2$ interface geometry as a stick and ball sketch. Some of the *c*-Si(111) surface atoms possess unsaturated bonds called silicon dangling bonds. These unpaired electrons have highly localized

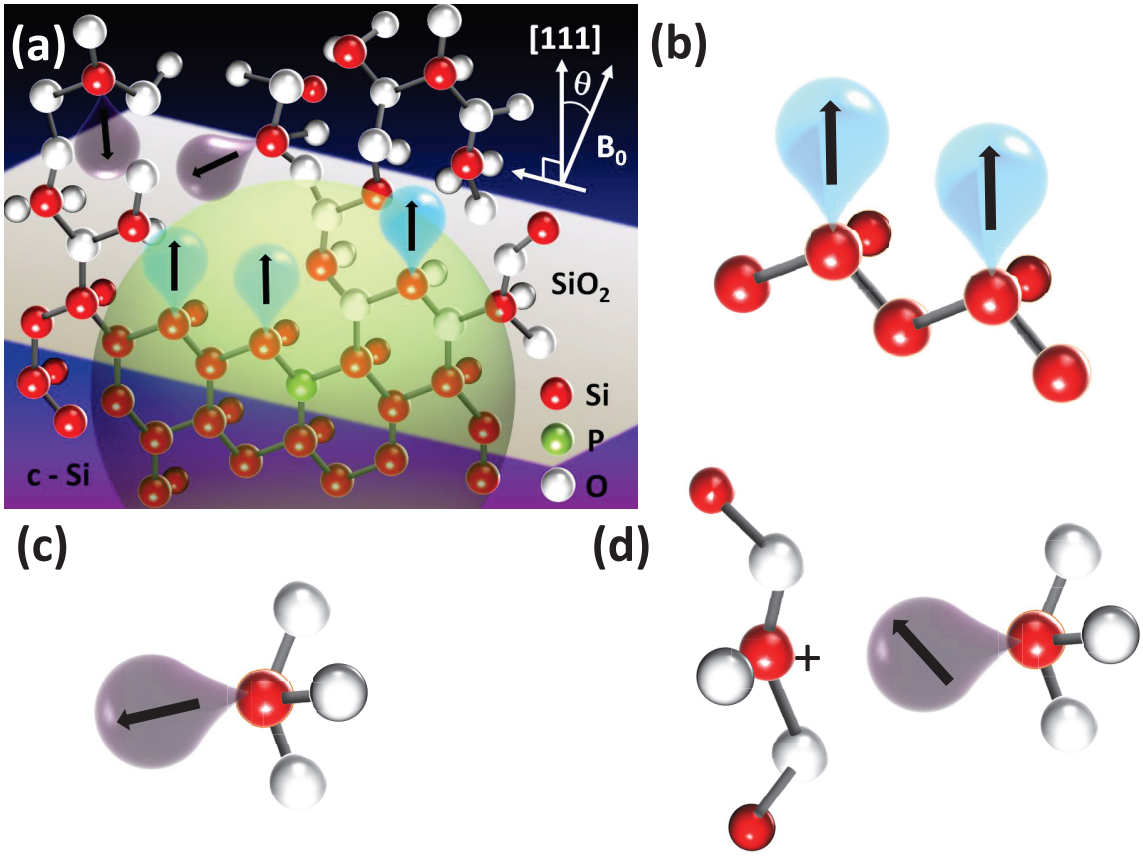

Figure 1.1: Ball and stick illustration of the atomic composition of the *c*-Si(111)/SiO_2 interface. (a) The ^{31}P donor state (large green shaded circle) is significantly larger than the P_b center. Exchange coupling between the two states is possible when they are sufficiently close to each other. The orientation of the interface is defined by the angle between the externally applied B_0 magnetic field and the (111) crystal axis which is perpendicular to the crystal surface. (b) Sketch of P_b defect center. P_b electron is localized on a silicon atom back bonded to three other silicon atoms. The main axis of the p-component of the P_b electron is perpendicular to the (111) interface.(c) Sketch of the dangling bond E' center localized on a silicon atom back bonded to three oxygen atoms. (d) Schematic diagram of a positively charged E' center, a hole trapped at an oxygen vacancy.

states with much p content and a little bit of s-content [28]. In contrast to the P_b state, the shallow (this means it is energetically only slightly below the conduction band energy) ^{31}P donor electron state (illustrated by the large shaded green circle in Fig. 1.1) possesses an s-like envelope function with a localization length of approximately ∼3nm. The s-like wave function envelope is strongly modulated by the periodic crystalline structure of its host environment. Thus, the wave function of the ^{31}P donor electron covers thousands of neighboring silicon atoms.

Two types of silicon dangling bonds dominate the electronic properties of the *c*-Si(111)/SiO_2 interface. Silicon dangling bonds oriented along the (111) direction are called P_b centers (Fig. 1.1 (b)). They are Si/SiO_2 interface traps which are highly anisotropic with regard to the angle between the external magnetic B_0 field and the electron p-state.

The other important silicon dangling bond defect is the E' center. E' centers occur at silicon atoms that are back bonded to the three oxygen atoms [34–36] (Fig. 1.1 (c)). E' centers can also act as interface traps. The bonding stoichiometry of the E' center illustrated in Fig. 1.1 (c) is only one example. Several other E' variants are known which involve nearby oxygen and hydrogen atoms. Sometimes, the paramagnetic silicon is coupled to a positively charged diamagnetic silicon (Fig. 1.1 (d)).

Since most silicon dangling bond defects are paramagnetic when uncharged due to their positive correlation energy, electron paramagnetic resonance spectroscopy (EPR) can provide information about the structure and electronic properties of these defects. As the *g*-factor anisotropy of P_b centers is well known ($g_\perp \approx 2.0081$, $g_\parallel \approx 2.0014$ [28]), we can unambiguously identify these centers with magnetic resonance spectra. *g*-factors of E' centers are also weak axial anisotropic. However, because there are various different E' centers, the corresponding E' lines are usually well approximated by a randomly oriented array of defects with $g_\parallel \approx 2.0018$ and $g_\perp \approx 2.0004$ [37, 38]. The $g_\parallel \approx 2.0018$ is very close to the free electron $g_e = 2\ .002319$.

1.3 Spin-dependent recombination at the *c*-Si/SiO_2 interface

In the presence of exchange between near-surface ^{31}P donors and dangling bond defects, charge transfer of the donor electron into the energetically lower interface

state can occur. This transition is sketched in Fig. 1.2 for the example of a $^{31}P/P_b$ defect pair. The figure shows the band diagram of this interface for flat band conditions. In the weakly coupled crystalline silicon, the donor-defect transition will be spin-conserved. Therefore, since a negatively charged, doubly occupied silicon dangling bond exists only in a singlet spin state, the transition probability

$$0 \leq P = |\langle S|\psi\rangle|^2 \leq \frac{1}{2} \tag{1.1}$$

of the charge transfer will strongly depend on the permutation symmetry of the two electrons before the transition takes place. Figure 1.2 shows how this phenomenon can lead to a control of the macroscopic excess charge carrier current by the spin-pair state of the two electrons in the two defects. In presence of excess charge carriers, pairs of ^{31}P and silicon dangling bonds will be quickly assumed to be one of the triplet states $|T+\rangle$ or $|T-\rangle$ since spin-pair states with singlet content ($|\uparrow\downarrow\rangle$ or $|\downarrow\uparrow\rangle$) are short lived. The electronic interface transition is therefore oppressed due to the Pauli blockade. When a magnetic resonant excitation (using EPR) will increase the singlet content, the transition will become allowed. Since the ^{31}P-silicon dangling bond transition charges the ^{31}P state positively and the silicon dangling bond negatively, it can be detected electrically by measurement of excess charge carrier currents. In presence of excess electrons and holes, these charge carriers will discharge the two oppositely charged defect states and reinitialize the pair under annihilation of the excess charge carrier pair. Thus, the spin-dependent transition described in Fig. 1.2 is a spin-dependent charge carrier recombination process. It provides a spin-to-charge conversion mechanism as a result, since the charge of the $^{31}P/P_b$ can be detected through the measurement of recombination currents. $^{31}P/P_b$ pairs have been proposed as electric readout mechanism for ^{31}P qubits [9].

1.4 Identification of spin-dependent interface transitions

The effect of an electric current control through spin-pair states of localized paramagnetic states can be studied by conductivity measurements under simultaneous manipulation of the involved spin states. When this spin manipulation is done though magnetic resonance, electrically detected magnetic resonance (EDMR) becomes pos-

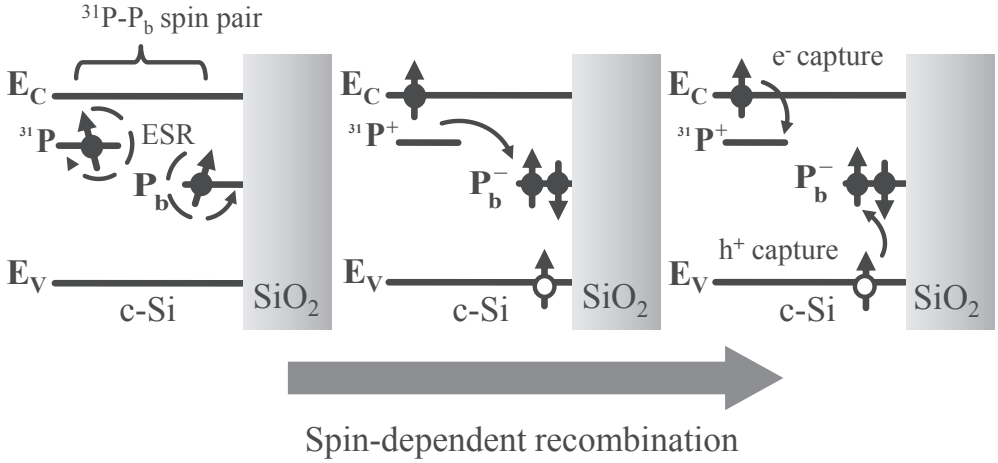

Figure 1.2: Band sketch illustrating the spin-dependent $^{31}\mathrm{P}/\mathrm{P}_b$ charge-carrier recombination transition. For details see the text.

sible. EDMR of c-Si(111)/SiO_2 interface transitions has previously been conducted on (100) oriented silicon surfaces with high ^{31}P concentration ($\approx 10^{17}$cm^{-3})[6, 10]. In these measurements, two well-known hyperfine resonances of the ^{31}P electron were observed as well as additional peaks corresponding to a variety of interface defect resonances.

In the following chapter, EDMR experiments on c-Si(111)/SiO_2 interface transitions are presented which follow a similar experimental approach. However, in contrast to these studies, the experiments reported here are performed on (111) oriented c-Si with a significantly low ^{31}P concentration. The aim of this study was to address the following questions:

(i) Is the EDMR signal that has previously been observed at magnetic fields between the two hyperfine split lines of the ^{31}P truly due to P_b states or are other interface defects involved in spin-dependent transitions? Are P_b states the only interface states involved in spin-dependent transitions as illustrated in Fig. 1.2 or are there other states at or near the interface, or even in the bulk, which could contribute to the observed signals? To address this question, a systematic study of the EDMR spectrum of the magnetic field dependence as a function of the interface orientation angle was made in order to observe all g-factors involved in spin-dependent recombination and to detect possible anisotropies of these centers.

(ii) As an understanding about the nature of the interface defects and the transitions between interface defects and the ^{31}P donor electrons is established, the main question of this study is addressed: Are the coherence times of ^{31}P donors near interface defects compromised? For this, a series of coherence time (T_2) measurements are carried out on ^{31}P donors in proximity to interface states and with the same samples, under the same conditions (in fact, during the same experimental runs), the coherence time of bulk ^{31}P was measured for comparison. For the interface T_2 measurements, modified Hahn echoes, detected with pEDMR, were used, in a similar way as recent studies of ^{31}P doped c-Si samples with (100) orientation [6] and spin-dependent ^{31}P bulk processes at very high magnetic fields [39]. For the bulk T_2 measurements, conventional EPR detected Hahn echo experiments were carried out. This comparative study of T_2 times was made as a function of the temperature for 5

K $\leq T \leq$ 13 K.

(iii) Finally, in order to obtain information on whether the spin-coherence times T_2 of near interface defect ^{31}P are determined by the electronic transitions between ^{31}P and interface states or by the interface defect-induced spin-spin relaxation processes as suggest by de Sousa [15], a comparison of electrically detected T_2 times and T_1 times was made for a temperature of $T = 5$K. In order to measure T_1, electrically detected inversion recovery measurements were performed. To the knowledge of the authors, this is the first time that such an experiment is demonstrated.

1.5 Experimental details

For the experiments presented in the following, we used 300 μm thick, (111) surface oriented silicon since P_b centers for this surface are all identically oriented. This is in contrast to the previously used (100) surface [6, 10] as the (100) surface allows silicon dangling bonds (here they are called P_{b0} states) to exist in two orientations at the same time which makes their mutual EPR spectroscopic distinction as well as their distinction from other possible interface defects very difficult. The experiments were conducted with dopant concentrations of [P] = 10^{15} cm^{-3} and 10^{16} cm^{-3}, less than the 10^{17} cm^{-3} of previous EDMR studies [6, 10]. The lower concentrations ensured that interactions between neighboring ^{31}P atoms which are known to exist [40] at [P] = 10^{17} cm^{-3} can be neglected.

In order to enable the electrical detection of spin-coherence, the *c*-Si samples required contact structures which would not strongly distort the homogeneity of the spin resonant microwave fields B_1. This problem was solved using a method similar to previous pEDMR studies at X-band [10, 41] - we designed long match-like sample substrates on which electrical sample contacts as shown in Fig. 1.3 (d), (e) outside of the microwave field are connected to the sample via $\sim$ 50 mm long thin-film Al wires whose thickness of 100 nm is below the penetration depth of the applied microwave radiation. The contact structures were fabricated using a photolithographical lift-off process that was carried out after the Al film was evaporated on the H-terminated silicon (111) surface of the *c*-Si samples that had been prepared by a wet treatment with hydrofluoric acid. In order to maximize the density of interface states, a native

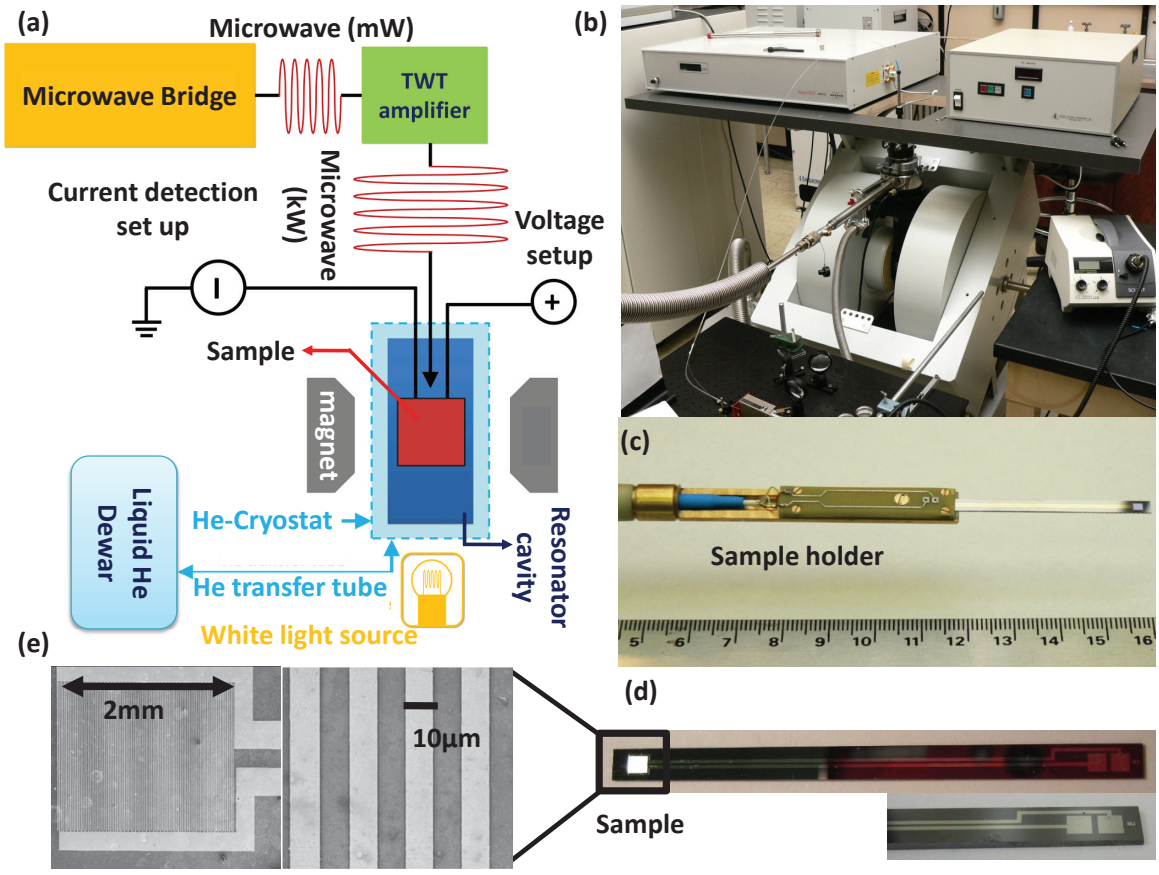

Figure 1.3: Experimental setup and structure of the sample. (a) Experimental setup for pulsed EDMR experiments. It consists of a Bruker Elexsys E580 EPR spectrometer, an Oxord helium flow cryostat, a helium transfer tube, electronics for the application and detection of transient currents and an ultraviolet and infrared filtered spectral light source. (b) Picture of the Bruker Elexsys E580 EPR facility. (c) PEDMR sample connector, which consists of a printed circuit board (PCB) for the electric contact with the sample and a brass holder needed for geometric sample alignment. (d) Photo of the *c*-Si pEDMR sample. (e) Microscope picture of the *c*-Si resistor strcuture using an interdigitated grid system. Aluminum wires with $\sim 10\mu$m width are deposited between the 2 mm $\times$ 3 mm *c*-Si(111)/SiO_2 sample areas.

oxide was grown on the (111) surface after the contact deposition by exposure of the sample to ambient air.

All EDMR and EPR experiments were carried out at X-band using a cylindrical dielectric low-Q pulse resonator which was part of a Bruker Elexsys E580 EPR spectrometer, which is shown in Fig. 1.3 (a), (b). The sample temperatures were obtained with a ^{4}He flow cryostat, and the excess charge carriers were induced through a spectral cold light source (IR and UV filtered spectral light) with an incandescent light source (Schott KL 2500 LCD) with lamp temperature of about 3000 K producing an integrated spectral intensity of approximately 5 Wcm^{-2} at the sample surface. The EDMR experiments were conducted by establishing a constant offset photocurrent using a constant current source with a time constant in excess of the experimental shot repetition time. Current transients were digitized and recorded following current amplification by a Stanford Research SR570.

The raw data recorded for the presented measurements were a combination of spin-dependent currents and microwave-induced artifact currents. The latter can be recorded separately by measurement of the current response at off-spin resonant B_0-fields. Magnetoresistance effects on the microwave-induced currents can be linearly extrapolated for *c*-Si at the given magnetic fields. The microwave current transients obtained from this procedure were subtracted from the raw data in order to reveal the current transients solely caused by spin-dependent transitions.

1.5.1 Experimental confirmation of spin-dependent interface processes

Transient measurements of photocurrent changes ΔI were recorded under various illumination conditions and temperatures. Fig. 1.4 displays a data set of ΔI(B_0,t) recorded as a function of the magnetic field B_0 and the time t after a 96-ns-long microwave pulse with a frequency of f =9.749 GHz and a power of $P \approx 8$ W for T =5 K and a constant photocurrent of $I = 270\mu$A. The sample orientation was $\theta = 0°$. The data set clearly confirms the expected EPR-induced currents with three local response maxima at B_0 = 346.37, 347.9, and 350.55 mT. The two outer peaks which are separated by a magnetic field of 4.2 mT are the two hyperfine lines of the ^{31}P donor electron while the peak close to the low-field (LF) ^{31}P line has been

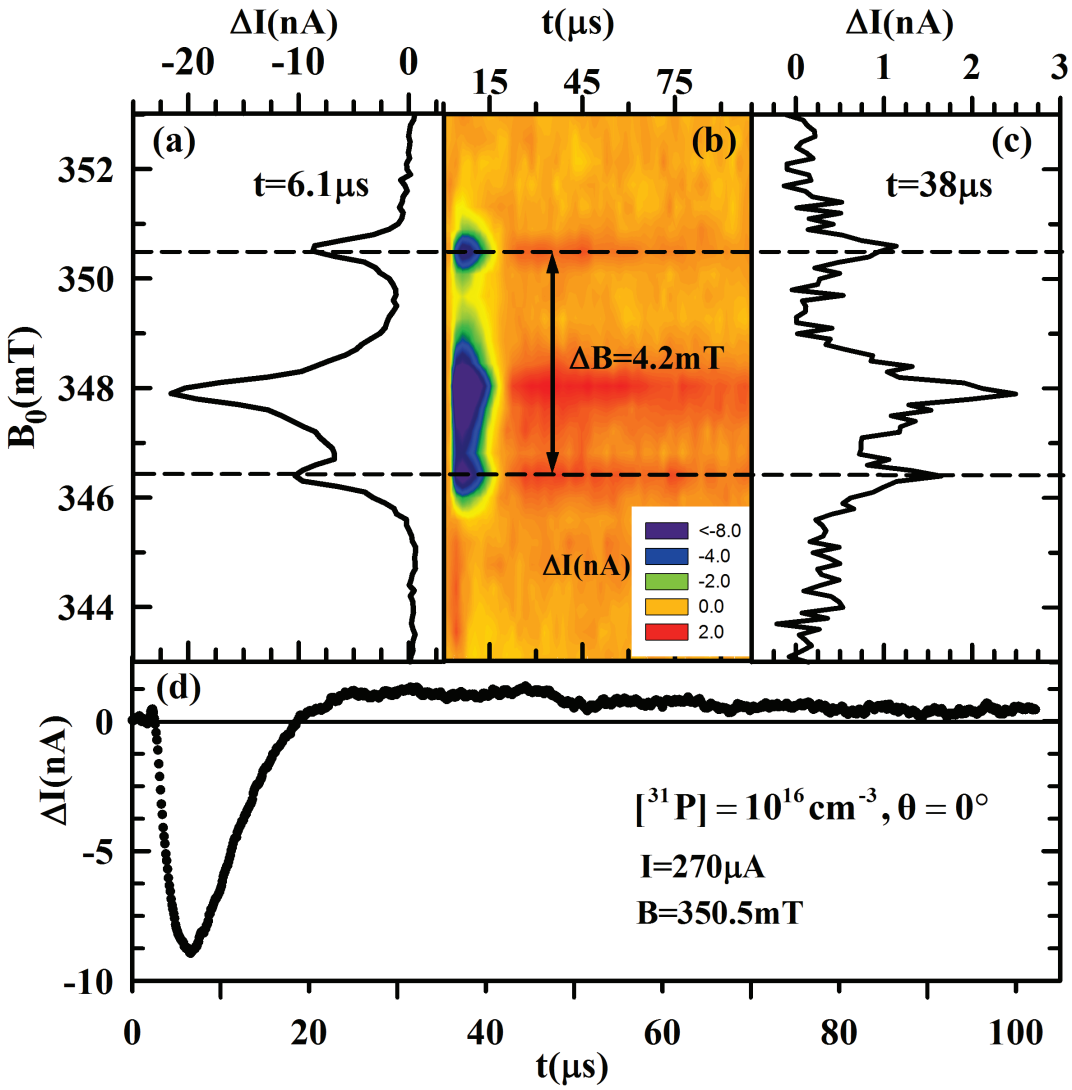

Figure 1.4: Plots of the microwave pulse (at $t = 0$) induced change ΔI of an interface photocurrent along a c-Si(111):P/sio interface as a function of time t and the applied magnetic field B_0. (a,c) Plots of ΔI as functions of B_0 for the times $t = 6.1$ μs and $t = 38$ μs, respectively, for which a quenching and an enhancement of the current changes reach their extrema. (b) Color contour plot of the entire data set $\Delta I(t, B_0)$ containing the data of the plots in (a), (c) and (d). (d) Plot of ΔI as a function of the time t for a magnetic field $B_0 = 350.5$ mT which was on resonance with the high field Phosphorous EPR line.

attributed to interface-defect states. Fig. 1.4 confirms the previous measurement of Stegner et al. Short microwave pulses change electronic transition rates between electronic interface states. This causes a quick quenching of the sample current due to the enhanced recombination of excess electrons and holes. Fig. 1.4 (d) shows that after the current is quenched, it first changes into a longer lived current enhancement before it returns to the steady state. This enhancement/quenching behavior is well known for the transient behavior of spin-dependent pair processes [42–44]. It reflect the different electronic relaxation times of spin-pairs with different spin-permutation symmetry state. In a simplified picture, the transient behavior of the current change ΔI can be described by the superposition (the sum) of two simple exponential decay functions with two different time constants and prefactors

$$\Delta I = Ae^{-m_s t} - Be^{-m_t t} \tag{1.2}$$

where the first exponential decay with the shorter constant $m_s = r_s + d_s$ is related to the singlet pair recombination rate (r_s) and dissociation rate (d_s) while the second exponential decay with longer time constant ($m_t = r_t + d_t$) is related in the same way to triplet pairs. Since any magnetic resonance-induced change of singlet and triplet densities leads to changes of opposite sign for the singlet and triplet densities (note that the spin-pair ensemble size is conserved during sufficiently short excitations), the coefficients A, B have opposite signs. Analytical solutions of this effect for EDMR or ODMR experiments have been studied by Boehme and Lips [42, 44], McCamey et al. [45], and Lee [46]. Note that changes to experimental parameters such as variations of temperature, sample voltage, the photocurrent, or the illumination change the quantitative dynamics of the observed transients. However, these changes do not alter the qualitative quenching/enhancement behavior displayed by the data set in Fig. 1.4 (d). This is consistent with previously reported measurements on c-Si(100):P/SiO_2 with [P]=10^{17} cm^{-3}. The transient current behavior shown in Fig. 1.4(d) is qualitatively in agreement with the observation of Stegner et al.

The observation that the transient current changes due to ^{31}P-silicon dangling bond pairs is accurately described by simple exponential functions is somewhat counterintuitive since the random spatial distribution of the paramagnetic states involved in these transitions suggests that the pair-partner distances within these pairs are

widely distributed. This distance distribution of states implies a distribution of transition times, which suggests that the observed current transients should follow distributions of exponential functions for which fits with single exponentials would be poor. In contrast, the observed quenching and enhancement transients are well fit by two single exponentials, which suggests that only a narrow range of transition times exists and, therefore, only pairs with a narrow range of intrapair distances contribute to the observed signals. We attribute the existence of a "main-pair distance" which dominates the observed signals to two factors: first, pEDMR signals vanish for pairs with very large distances (larger than the localization length of the two paramagnetic states) as the probability for recombination is greatly diminished and, second, for very short distances, where the exchange between the two states exceeds the Larmor frequency difference within the pair [42], the signal vanishes as the resonantly induced change in spin-pair states between singlet and triplet configurations becomes increasingly forbidden. Thus, there will always be a finite main-pair distance where spin-resonance-induced rate changes become maximal and pairs around this distance will dominate the observed spin-dependent currents.

1.6 References

[1] G. Feher and E. A. Gere. *Physical Review*, 103:501, 1956.

[2] G. Feher and E. A. Gere. *Physical Review*, 114:1245, 1959.

[3] I. Appelbaum, B. Huang, and D. J. Monsma. *Nature*, 447:295–298, 2007.

[4] B. E. Kane. *Nature*, 393:133–137, 1998.

[5] R. G. Clark, R. Brenner, T. M. Buehler, V. Chan, N. J. Curson, A. S. Dzurak, E. Gauja, H. S. Goan, A. D. Greentree, T. Hallam, A. R. Hamilton, L. C. L. Hollenberg, D. N. Jamieson, J. C. McCallum, G. J. Milburn, J. L. O'Brien, L. Oberbeck, C. I. Pakes, S. D. Prawer, D. J. Reilly, F. J. Ruess, S. R. Schofield, M. Y. Simmons, F. E. Stanley, R. P. Starrett, C. Wellard, and C. Yang. *Philosophical Transactions of the Royal Society of London. Series A: Mathematical, Physical and Engineering Sciences*, 361:1451–1471, 2003.

[6] H. Huebl, F. Hoehne, B. Grolik, A. R. Stegner, M. Stutzmann, and M. S. Brandt. *Physical Review Letters*, 100:177602, 2008.

[7] A. M. Tyryshkin, S. A. Lyon, A. V. Astashkin, and A. M. Raitsimring. *Physical Review B*, 68:193207, 2003.

[8] J. J. L. Morton, A. M. Tyryshkin, R. M. Brown, S. Shankar, B. W. Lovett, A. Ardavan, T. Schenkel, E. E. Haller, J. W. Ager, and S. A. Lyon. *Nature*, 455:1085–1088, 2008.

[9] C. Boehme and K. Lips. *Physica Status Solidi (b)*, 233:427–435, 2002.

[10] A. R. Stegner, C. Boehme, H. Huebl, M. Stutzmann, K. Lips, and M. S. Brandt. *Nature Physics*, 2:835, 2006.

[11] T. Schenkel, J. A. Liddle, J. Bokor, A. Persaud, S. J. Park, J. Shangkuan, C. C. Lo, S. Kwon, S. A. Lyon, A. M. Tyryshkin, I. W. Rangelow, Y. Sarov, D. H. Schneider, J. Ager, and R. de Sousa. *Microelectronic Engineering*, 83:1814–1817, 2006.

[12] V. C. Chan, T. M. Buehler, A. J. Ferguson, D. R. McCamey, D. J. Reilly, A. S. Dzurak, R. G. Clark, C. Yang, and D. N. Jamieson. *Journal of Applied Physics*, 100:106104, 2006.

[13] T. M. Buehler, V. Chan, A. J. Ferguson, A. S. Dzurak, F. E. Hudson, D. J. Reilly, A. R. Hamilton, R. G. Clark, D. N. Jamieson, C. Yang, C. I. Pakes, and S. Prawer. *Applied Physics Letters*, 88:192101, 2006.

[14] T. Schenkel, J. A. Liddle, A. Persaud, A. M. Tyryshkin, S. A. Lyon, R. de Sousa, K. B. Whaley, J. Bokor, J. Shangkuan, and I. Chakarov. *Applied Physics Letters*, 88:112101, 2006.

[15] R. de Sousa. *Physical Review B*, 76:245306, 2007.

[16] G. Lucovsky, Y. Wu, H. Niimi, V. Misra, and J. Phillips. *Applied Physics Letters*, 74:2005, 1999.

[17] K. Eng, R. N. McFarland, and B. E. Kane. *Applied Physics Letters*, 87:052106, 2005.

[18] K. Eng, R. N. McFarland, and B. E. Kane. *Physical Review Letters*, 99:016801, 2007.

[19] D. R. McCamey, H. Huebl, M. S. Brandt, W. D. Hutchison, J. C. McCallum, R. G. Clark, and A. R. Hamilton. *Applied Physics Letters*, 89:182115–3, 2006.

[20] F. Hoehne, H. Huebl, B. Galler, M. Stutzmann, and M. S. Brandt. *Physical Review Letters*, 104:046402, 2010.

[21] F. Hoehne, L. Dreher, H. Huebl, M. Stutzmann, and M. S. Brandt. *Physical Review Letters*, 106:187601, 2011.

[22] Y. Nishi. *Japanese Journal of Applied Physics*, 10:52, 1971.

[23] E. Poindexter, P. Caplan, B. Deal, and R. Razouk. *Journal of Applied Physics*, 52:879, 1981.

[24] E. Poindexter, G. Gerardi, M. Rueckel, P. Caplan, N. Johnson, and D. Biegelsen. *Journal of Applied Physics*, 56:2844, 1984.

[25] A. Stesmans. *Zeitschrift för Physikalische Chemie Neue Folge*, 151:191, 1987.

[26] Y. Kim and P. Lenahan. *Journal of Applied Physics*, 64:3551, 1988.

[27] A. Stesmans and K. Vanheusden. *Physical Review B*, 44:11353, 1991.

[28] P. M. Lenahan and J. J. F. Conley. *Journal of Vacuum Science and Technology B*, 16:2134–2153, 1998.

[29] R. Mller, P. Kanschat, S. von Aichberger, K. Lips, and W. Fuhs. *Journal of Non-Crystalline Solids*, 266-269:1124–1128, 2000.

[30] D. R. McCamey, G. W. Morley, H. A. Seipel, L. C. Brunel, J. van Tol, and C. Boehme. *Physical Review B*, 78:045303, 2008.

[31] F. Friedrich, C. Boehme, and K. Lips. *Journal of Applied Physics*, 97:056101, 2005.

[32] C. Boehme, F. Friedrich, T. Ehara, and K. Lips. *Thin Solid Films*, 487:132, 2005.

[33] C. Boehme and K. Lips. *Physica B: Condensed Matter*, 376-377:930–935, 2006.

[34] P. Lenahan and P. Dressendorfer. *Applied Physics Letters*, 44:96, 1984.

[35] R. Silsbee. *Journal of Applied Physics*, 32:1459, 1961.

[36] B. Triplett, T. Takahashi, and T. Sugano. *Applied Physics Letters*, 50:1663, 1987.

[37] P. J. Caplan, E. H. Poindexter, B. E. Deal, and R. R. Razouk. *Journal of Applied Physics*, 50:5847–5854, 1979.

[38] E. H. Poindexter, P. J. Caplan, B. E. Deal, and R. R. Razouk. *Journal of Applied Physics*, 52:879–884, 1981.

[39] G. W. Morley, D. R. McCamey, H. A. Seipel, L. C. Brunel, J. van Tol, and C. Boehme. *Physical Review Letters*, 101:207602, 2008.

[40] G. Feher. *Journal of Physics and Chemistry of Solids*, 8:486–486, 1959.

[41] D. R. McCamey, H. A. Seipel, S.-Y. Paik, M. J. Walter, N. J. Borys, J. M. Lupton, and C. Boehme. *Nature Materials*, 7:723, 2008.

[42] C. Boehme and K. Lips. *Physical Review B*, 68:245105, 2003.

[43] D. R. McCamey, K. J. v. Schooten, W. J. Baker, S.-Y. Lee, S.-Y. Paik, J. M. Lupton, and C. Boehme. *Physical Review Letters*, 104:017601, 2010.

[44] C. Boehme and K. Lips. *Applied Physics Letters*, 79:4363–4365, 2001.

[45] D. R. McCamey, S. Y. Lee, S. Y. Paik, J. M. Lupton, and C. Boehme. *Physical Review B*, 82:125206, 2010.

[46] S.-Y. Lee. *Pulsed electrically and optically detected magnetic resonance specgtroscopy of disordered semiconductors*. PhD thesis, 2011.

CHAPTER 2

IDENTIFICATION OF DANGLING BOND DEFECTS

The data presented in Fig. 1.4 confirm that spin-dependent interface recombination processes can be observed with pEDMR at the c-Si(111):P/SiO_2 interface. The observed signals qualitatively similar to those seen previously at the c-Si(100):P/SiO_2 interface with higher ^{31}P concentration. It is therefore possible to systematically study the nature and the origin of these processes with pulsed (p) EDMR at the (111) interface, too. Fig. 1.4 (a) is a plot of the pulse-induced photocurrent change $\Delta I(B_0)$ as a function of B_0 at $t = 6.1\mu$s after the pulse, when the photocurrent changes are maximal. As already seen for (100) interfaces, three resonance peaks are present. The shape of the B_0-spectrum does not significantly change at other time slices (see Fig. 1.4 (c)), yet the magnitude and the sign of the ΔI does; it follows the quenching/enhancing behavior discussed above.

2.1 g-factor anisotropy of P_b center

2.1.1 Experimental data

The data displayed in Fig. 2.1 represent the measured spectra normalized to their respective extrema. The normalization was made for better comparison of the data sets since the signals obtained from samples with [P]=10^{16} cm^{-3} were significantly stronger compared to signals from samples with [P]=10^{15} cm^{-3} (note the higher relative noise in the latter spectra). The spectra are measured with various interface orientations for the two ^{31}P concentrations. In order to fit these spectra, four different Gaussian functions are needed. However, since the free fit of four partially overlapping Gaussian functions has much ambiguity due to the 12 fit parameters (peak centers, width, and magnitude for all four lines), a well-defined, stepwise, fit of the spectra was employed: First, the outer two peaks as the two hyperfine split resonances of the ^{31}P

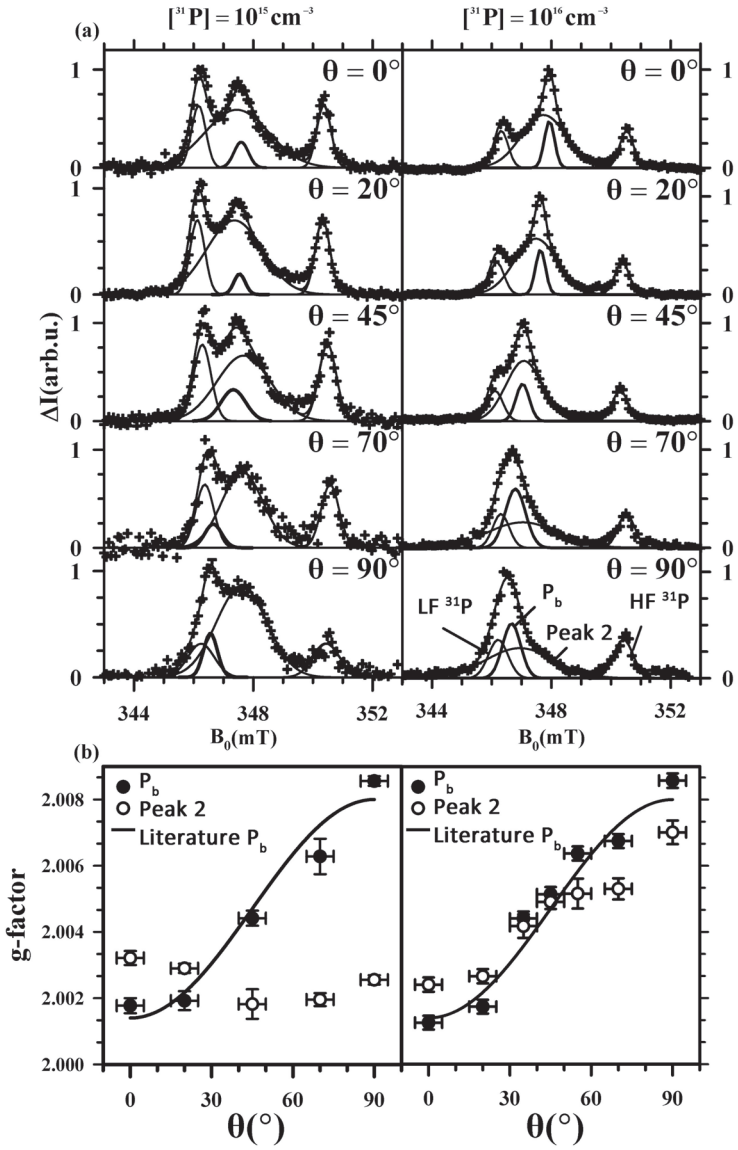

Figure 2.1: Crystal orientation dependencies of the g-factor distributions of electron spins in c-Si(111)/SiO_2 interface. (a) Plots of ΔI as functions of B_0 at arbitrary times t after a microwave pulse with arbitrary length τ, frequency $f \approx 9.5\,GHz$ and a power $P = 8$ W and under otherwise identical conditions as for the data in Fig. 1.4. The data were collected for five sample orientations θ and two ^{31}P concentrations. The displayed plots are normalized to the maximum of ΔI. The solid lines represent fits of the data consisting of four Gaussian peaks, two related to the ^{31}P hyperfine line and two peaks related to interface defects. The plot for $[^{31}\mathrm{P}] = 10^{16}\mathrm{cm}^{-3}$ and $\theta = 90°$ has the peak assignments to the low field (LF) and high field (HF) ^{31}P resonances, the P_b peak as well as peak 2. (b) Plots of the fit results of the g-factors for the two interface defect lines as a function of θ for the two ^{31}P concentrations. The solid lines indicate the literature values for the P_b center.

state were identified. They are known to be separated by 4.2 mT [1]. The low field ^{31}P resonance is at $\sim$ 346 mT and the high field ^{31}P peak is at $\sim$ 350 mT. The averaged g-factor of the ^{31}P donor electron is 1.9985. This g-factor can be used as a reference value for the calibration of the B_0 measurements. By doing this, it was found that the B_0 magnetic field offset for the EPR measurements with the used Bruker Elexsys E580 EPR spectrometer was typically $\sim$ 0.2 mT. Two more Gaussian peaks are needed to fit the entire spectrum. To do this, the two ^{31}P hyperfine resonances were assigned first before the two additional peaks were fit to the E' and P_b resonances. The fit results for all displayed spectra, as well as the four constituent peaks, are shown in Fig. 2.1. Fig. 2.1 (b) shows the g-factors of the non ^{31}P lines as a function of the angle θ, obtained from the fit. It also displays a solid line which represents literature values for EPR [2] and EDMR [3, 4]-detected P_b centers.

2.1.2 Discussion

The fit results discussed above show that the anisotropy and absolute values of one of the two non phosphorous peaks are in good agreement with the literature anisotropy of the P_b center. Therefore, based on this agreement, this peak can be assigned to spin-dependent transitions (recombination) involving P_b centers. Previous pEDMR measurements on c-Si(111)/SiO_2 interfaces with no ^{31}P doping also have shown P_b signals [3, 4]. Since there are no ^{31}P pEDMR lines in intrinsic c-Si, spin-dependent P_b interface recombination does not necessarily require the presence of ^{31}P atoms. Thus, the P_b involvement revealed by the data in Fig. 2.1 may either involve ^{31}P as illustrated in Fig. 1.1 or be due to a different interface recombination process such as spin-dependent P_b-E' or P_b-P_b transitions.

In contrast to the P_b resonance line, the assignment of the second non ^{31}P peak (referred to as peak 2; see peak assignment in Fig. 2.1 (a)) is less straightforward. The fit results for $[^{31}] = 10^{15}$ cm^{-3} suggest that peak 2 is isotropic, or only weakly anisotropic, whereas the data for [P]=10^{16} cm^{-3} are consistent with a slight anisotropy, yet this observation is ambiguous due to the given error margins. Previous pEDMR spectra on intrinsic c-Si have shown a second isotropic recombination signal with g $\approx$ 2.0023(6) [3], in good agreement with peak 2 observed on the c-Si sample with

[p]=10^{15} cm^{-3}. There are two possible explanations for the observed differences between the two sets of spectra in Fig. 2.1 (b): (i) The nature of peak 2 is different at higher ^{31}P concentrations, suggesting that the observed processes may be different. (ii) The observed resonance is isotropic for both samples and the increasing fit error of the center g factor for larger values of θ causes a systematic shift of the measured g-factor. The larger error is due to the orientation-dependent width of peak 2 and the overall relative intensity in comparison to the P_b and ^{31}P signals at higher dopant concentrations. The fits become increasingly ambiguous for large θ as three resonances (low-field ^{31}P, P_b, and peak 2) have larger overlap. Note that the error ranges given in the plots in Fig. 2.1 (b) are based on the uncertainty estimates of the fit routines. Additional uncertainties such as fit-induced systematic errors may exist. Thus, it is not clear whether the different results for g-factors of peak 2 obtained for different ^{31}P concentrations are real or fit artifacts and therefore an unambiguous statement about the anisotropy of peak 2 is not possible.

Given the pEDMR measurements on [^{31}P]-doped c-Si(111)/SiO_2 samples in Fig. 2.1, it is difficult to unambiguously assign peak 2 to a particular interface-defect type. Due to its strong inhomogeneity (the large line width) and its overall magnitude in comparison to the other pEDMR lines, it is possible that peak 2 is due to one or more randomly oriented anisotropic centers whose powder spectra would cause a macroscopically isotropic wide resonance line. As discussed above, there exist several different kinds of E' [2] centers such as E' centers with different back bonds and different relaxation states (e.g. the unrelaxed E' center which is called E'_δ). If we assume peak 2 consists of E' centers, it is natural that the line width of peak 2 is large due to randomly oriented E' defects, which have different bonding structures and g-factors ($g_{\|} \approx 2.0018$ and $g_{\perp} \approx 2.0004$.). The g-factor of undoped c-Si samples ($g \approx 2.0023(6)$) is very close to the literature g-factor of E' center and to the data presented here. Furthermore, the g-factor and the linewidth of the data in Fig. 2.1 are close (yet not equal) to the g factor and the linewidth of E' centers in amorphous SiO_2. Thus, it is concluded that the observed pEDMR data are due to transitions involving E' centers in proximity to the c-Si:P/SiO_2 interface.

Charge carrier trapping and recombination may work in a similar way for both P_b

centers with well-defined orientation as well as the randomly oriented E' centers. Due to the slight delocalization of the ^{31}P donor electron state [5], it is conceivable that transitions between the donor states and the E' are possible. This again is consistent with the hypothesis that peak 2 is due to E' centers in proximity of the c-Si:P/SiO_2 interface. This hypothesis will be scrutinized in the following chapters (4, 5).

2.2 Identification of ^{31}P to interface-defect transitions

2.2.1 Experimental data

The plots in Fig. 2.1 demonstrate the involvement of at least three qualitatively different paramagnetic states in spin-dependent charge-carrier transitions, the ^{31}P, the P_b, and the E' state. This observation, however, does not prove that the observed recombination transitions take place between these different states. For spin-dependent transitions between localized states, spin-pairs may be formed by identical defect states (e.g. P_b-P_b pairs) or different spin states (e.g. the ^{31}P-P_b pairs). It is known that spin-dependent resonant tunneling between P_b centers becomes significant at high magnetic fields [6]. Because there are six conceivable pair combinations for the the three states, the detection of multiple EDMR lines as in Fig. 1.4 and 2.1 leaves the exact nature of these transitions elusive.

In order to get insight into the pair combinations, the dynamics of the spin-dependent processes associated with the observed resonances was analyzed. Since spin-selection rules discriminate between permutation symmetries of spin s $=\frac{1}{2}$ pairs, [7, 8] (which means the mutual orientation of the two spins), the transient behavior of spin-dependent transitions exhibits is identical after a spin-resonant manipulation of either one of the two pair-partners. In contrast, if two EDMR-detected resonances exhibit a different transient behavior after the same pulsed excitation, the spin-dependent transitions corresponding to these resonances must be different as well. Thus, the dynamics of spin-dependent transition rates for different g-factors given insight on whether these g-factors belong to different processes or not. If the transient behavior is identical, the two resonances may belong to identical transitions. If the transient behavior is different, the two resonance cannot belong to the same process. It is conceivable that two observed resonances have the same transient

behavior coincidentally, even though the transition processes are different. Therefore, the comparison of current transients can only refute but not unambiguously confirm spin-dependent transitions, even though the coincidental identity of two independent current transients is usually rather unlikely. In any case, the observation of identical transients requires further testing of the correlation under varying experimental conditions or other experiments which confirm a pair mechanism independently (see Chapter 4).

We compare the "zero-crossing time" τ_0, defined as the time after the pulsed excitation of a spin-resonance-induced current transient when the quenching and enhancement are identical. The comparison as shown in Fig. 1.4 (b) clearly reveals identical $\tau_0 \approx 18$ μs with an error of 1μs. This suggests that the processes connected to these resonances are due to transitions involving both the ^{31}P donor states as well as the P_b interface state or the E' near interface state in the way depicted in the sketch in Fig. 2.2.

In order to test whether τ_0 for the interface defects and the ^{31}P remained identical when the dynamics of the spin-dependent current signal is changed, the experiment presented in Fig. 1.4 (b) was repeated under various combinations of temperatures (5, 8, 10, 13, and 15 K), sample currents [10-300 μA (and therefore different electric fields)], and sample surface orientations for the two different ^{31}P doping concentrations mentioned above. Due to the variation in charge-carrier concentration as well as Fermi and quasi-Fermi energies caused by changing these experimental parameters, the dynamics of the observed spin-dependent recombination transitions, and therefore the dynamics of the observed current signals, changed significantly between measurements. For all data sets, τ_0 was determined for transients recorded at magnetic fields corresponding to the two ^{31}P hyperfine resonances as well as at the maximum of the overlapping interface-defect signals. The results of this procedure are displayed in Fig. 2.2 in two correlation graphs, for samples with the two different donor concentrations. Each graph displays a plot of τ_0^A versus τ_0^B with A and B corresponding to the ^{31}P low-field and the 31P high-field resonances, respectively represented by the circles; the ^{31}P low-field and the interface state resonances, respectively represented by the squares; and the ^{31}P high-field and the interface state resonances, respectively

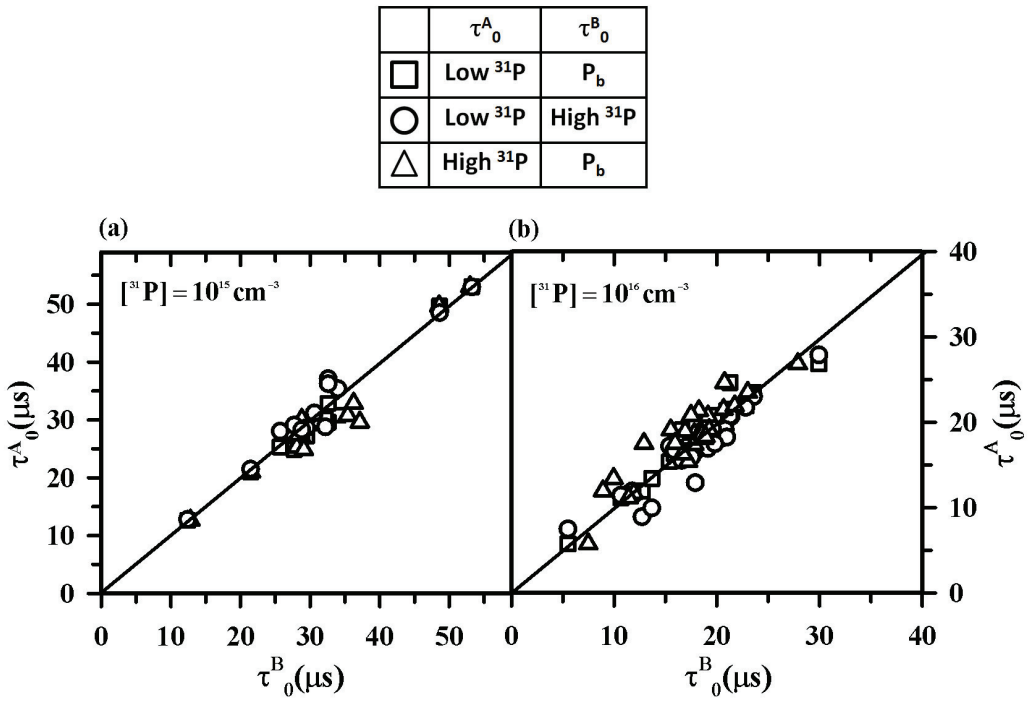

Figure 2.2: Plots of the zero crossing times τ_0 of magnetic resonantly induced photocurrent transients of the ^{31}P low or high field resonance (τ_0^A) versus the zero crossing times of magnetic resonantly induced current transients of the P_b/E' center resonances (τ_0^B) measured for a variety of different samples and sample conditions (temperature, offset current, illumination). The solid line is a linear function through the origin with slope 1. The two plots made for the two concentrations show a strong correlation of the zero crossing times of all three resonances.

represented by the triangles.

2.2.2 Discussion

The data in Fig. 2.2 reveal three observations:

(i) As anticipated, the variation of experimental parameters clearly varies the dynamics of the observed signals.

(ii) While similar combinations of experimental parameters were used for the two concentrations, the times τ_0 of the samples with P $=10^{15}$ cm^{-3} are generally slower than the τ_0 obtained for P $=10^{16}$ cm^{-3}. This observation shall not be discussed quantitatively in the following; however, it is conceivable that as an increase in the ^{31}P doping concentration leads to a smaller main-pair distance (note the definition of main-pair distance given in Sec. 1.4) for ^{31}P to interface-defect pairs as well as ^{31}P to ^{31}P pairs, it should not lead to a change in the main-pair distance of interface-defect pairs. The observed general decrease in the transition time with an increase in the ^{31}P concentration therefore suggests that the observed signals are predominantly due to transitions involving ^{31}P and not transitions between two interface defects. We note that there may be other reasons for this decrease in transition times with increasing doping density: one such possibility is that different internal fields may lead to different energy separations between pair-partners with different intrapair distance, with a corresponding change in transition probability.

(iii) The entire set of data reveals a strong correlation of τ_0 between any combinations of signals, whether it is between the two ^{31}P hyperfine signals or between the interface signals and either one of the two ^{31}P hyperfine signals. The correlation between the two ^{31}P hyperfine peaks is expected as the only difference between ^{31}P atoms contributing to these two peaks is the nuclear-spin state, which has little influence on electronic transitions times. The strong correlation between the 31P peaks and the interface states is again strong evidence that the spin-dependent transitions measured involve ^{31}P interface-defect pairs in the way sketched in Fig. 1.1.

It was not possible to obtain unambiguous correlation plots similar to those in Fig. 2.2 for the two different interface and near interface defects discussed above. It is therefore not possible to verify whether the observed correlation between the ^{31}P and the interface defects applies to both interface centers or only to the one which

dominated under the observed conditions. However, we point out that the strong correlation seen in the plots of Fig. 2.2 is consistent with the assumption that the dynamics of both defects correlates with the ^{31}P dynamics and, thus, spin-dependent recombination through both interface defects in the manner sketched in Fig. 1.1 seems to be possible. The correlation data in Fig. 2.2 raise a question about the presence of spin-dependent transitions between interface defects. It is known from previous pEDMR studies of (111) oriented nominally intrinsic c-Si(111)/SiO_2 interfaces at X band [3, 4, 9], as well as from recent pEDMR studies at high magnetic fields ($\approx$ 8.5 T) [6], that spin-dependent transitions involving only interface defects but not ^{31}P are possible and that these transitions can be due to spin-dependent resonant tunneling between two interface states in sufficient spatial and energetic proximity.

We conclude from the data seen in Fig. 2.2 that, while such interface-defect-only processes may or may not have been present at the investigated c-Si:P/SiO_2 interfaces, they did not dominate the observed spin-dependent rates, consistent with the very weak signal strength of previous pEDMR measurements on intrinsic c-Si(111)/SiO_2 interfaces conducted at X band [3]. The interface-defect signals are weak in spite of the presence of a significantly higher interface-defect density compared to the areal density of ^{31}P close to the interface. This may be explained by considering the signal from interface-defect pairs, which have almost identical g-factors and therefore stronger coupling, leading to lower pEDMR signals than those seen from the interface ^{31}P-defect pairs which have quite different g-factors and weaker, but still finite, coupling [8], and therefore dominate the signal. Another possibility that could account for the weakness of interface-interface transitions is simply the significantly smaller geometrical size of the interface states in comparison to the large ^{31}P donor wave function which extends over several nm.

2.3 References

[1] G. Feher and E. A. Gere. *Physical Review*, 114:1245, 1959.

[2] P. M. Lenahan and J. J. F. Conley. *Journal of Vacuum Science and Technology B*, 16:2134–2153, 1998.

[3] C. Boehme and K. Lips. *Physica B: Condensed Matter*, 376-377:930–935, 2006.

[4] F. Friedrich, C. Boehme, and K. Lips. *Journal of Applied Physics*, 97:056101, 2005.

[5] B. Koiller, X. Hu, and S. Das Sarma. *Physical Review B*, 66:115201, 2002.

[6] D. R. McCamey, G. W. Morley, H. A. Seipel, L. C. Brunel, J. van Tol, and C. Boehme. *Physical Review B*, 78:045303, 2008.

[7] C. Boehme and K. Lips. *Physical Review B*, 68:245105, 2003.

[8] A. Gliesche, C. Michel, V. Rajevac, K. Lips, S. D. Baranovskii, F. Gebhard, and C. Boehme. *Physical Review B*, 77:245206, 2008.

[9] C. Boehme, F. Friedrich, T. Ehara, and K. Lips. *Thin Solid Films*, 487:132, 2005.

CHAPTER 3

T_1 AND T_2 COHERENCE TIMES OF ELECTRON SPINS AT THE *c*-Si/SiO_2 INTERFACE

The ability to perform spin-Rabi nutation is a crucial prerequisite for the coherence time measurements using echo pulse sequences as it reveals the resonantly induced Rabi frequency for a given set of experimental conditions, e.g. for the applied microwave power. The Rabi frequency is needed to determine the pulse lengths required to obtain the correct nutation angles during the pulse sequences.

3.1 Electrical detection of spin coherence

We performed transient nutation style experiments for the electrical detection of spin-Rabi nutation. For these measurements, the photocurrent change ΔI was integrated between two appropriately chosen integration times T_1 and T_2 after the microwave pulse, so we obtain a charge

$$Q = \int_{t_1}^{t_2} \Delta I(t) dt \tag{3.1}$$

that is proportional to the number of spin-dependent transitions induced by the resonant excitation [1]. As Q is proportional to the projection of the resonantly prepared coherent spin state at the end of the excitation pulse of length onto the singlet state $|S\rangle$ [2, 3] the measurement of $Q(\tau) \propto |\langle S|\psi(\tau)\rangle|^2$ reveals the propagation of the singlet content during the pulse in a transient nutation-style experiment. Fig. 3.1 (a) displays the measurement of $Q(\tau,B_0)$ as a function of the pulse length and the magnetic field B_0 for a *c*-Si sample with P = 10^{16} cm^{-3}, a temperature T = 5 K, θ =90°, and integration times $T_1 = 6$ μs and $T_2 = 16$ μs.

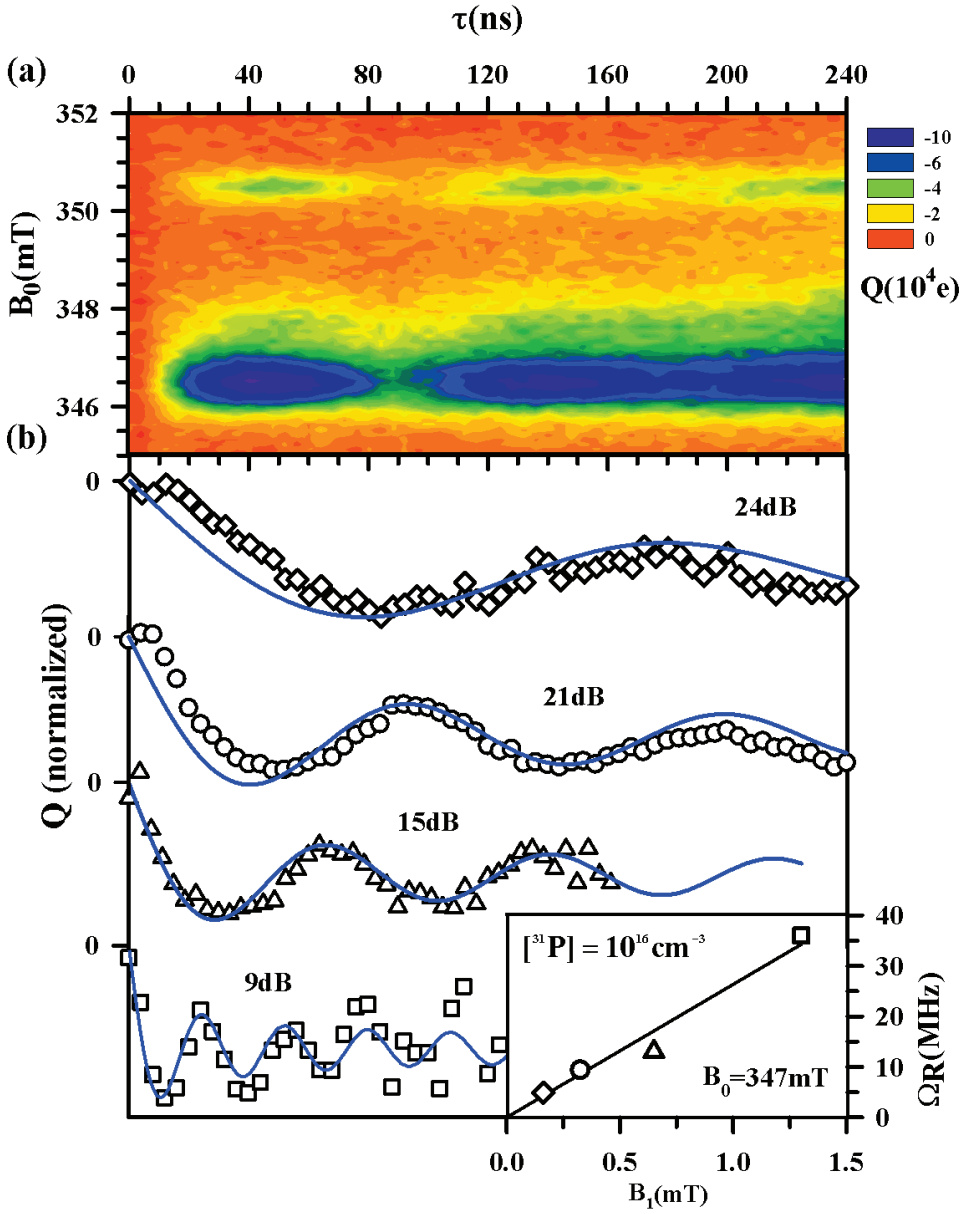

Figure 3.1: Electrically detected spin-Rabi nutations. (a) Plot of the measured integrated charge $Q(\tau, B_0)$ as defined by Eq. (3.1) as a function of the magnetic field B_0 and the length τ of an applied microwave pulse with frequency $f = 9.7475$ GHz and power $P = 8$ W. (b) The symbols represent a plot of the measured charge $Q(\tau)$ for four different microwave powers at $B_0 = 347$ mT. Note that for the latter case, the pulse length was recorded up to $\tau = 120$ ns only as the measurement was limited by signal perturbation due to the pulse-induced microwave current artifacts. The blue lines represent fits of an integrated Bessel function to the experimental data. The Rabi-nutation frequencies obtained from these fits are displayed in the inset as a function of the applied B_1 field. The fit of a linear function through the origin (black line) shows good agreement.

3.1.1 Discussion

The data set displayed in Fig. 3.1 shows that Q has an oscillating behavior around the same magnetic fields which produced local current response maxima in the data set displayed in Fig. 1.4. The oscillatory dependence is due to the dephasing spin-Rabi nutations as demonstrated, for the magnetic field $B_0 = 348$ mT, by the data sets displayed in Fig. 3.1 (b): the four plots show Q for four different micro-wave powers B_1 field strengths. We anticipate [2] the spin-Rabi-nutation signal of an inhomogeneously broadened spin ensemble to follow the integral of a first kind Bessel function,

$$Q(\tau) \propto \int_0^{\gamma B_1 \tau} J_0(2x)dx = \frac{1}{\pi}\int_{-\infty}^{\infty} \frac{\sin^2\left(\gamma B_1 \tau\sqrt{1+x^2}\right)}{1+x^2}dx \tag{3.2}$$

in which $\gamma \approx 2.8\ MHz/G$ is the gyromagnetic ratio. A fit of the four data sets in Fig. 3.1 (b) with Eq.(2) shows a good agreement and provides values for the nutation frequencies $\Omega_R = \gamma B_1$ for the four different powers. A plot of Ω_R versus the B_1 fields obtained from the relative microwave attenuation used for the four measurements shows that the expected linearity of the spin-Rabi nutation is given.The data in Fig. 3.1 are thus shown to be due to the spin-Rabi nutation of ^{31}P donor and interface electron spins, confirming the previously reported observation made for c-Si(100):P/SiO_2 interface with higher ^{31}P concentration. Note that with the data obtained from the transient nutation measurement, it is possible to determine the length of π and $\frac{\pi}{2}$ pulses as needed for the T_2 measurements in the following. The latter will be necessary since the decay of the Rabi nutation as displayed in Fig. 3.1 is not a measure for spin coherence.

The agreement of the nutation data with the integrated Bessel function is indicative of coherent dephasing, not coherence decay, being the dominant source of the observed nutation decay. This assumption is confirmed by the electrically and pEPR detected echo data discussed below, which show that the real T_2 spin-coherence time of the ^{31}P donor electrons is significantly longer than the decay of the nutation signal.

3.2 Comparison of the coherence time T_2 of ^{31}P donor electrons at the *c*-Si:P/SiO_2 interface and in the *c*-Si:P bulk

3.2.1 pEDMR and pEPR-detected spin echoes

The data presented in Secs. 1.4 and 2.2 showed that the spin-dependent current observed at *c*-Si:P/SiO_2 interfaces are due to transitions that take place between ^{31}P donor electron states and *c*-Si:P/SiO_2 interface states in their proximity. A measurement of the ^{31}P donor electron-spin-coherence time T_2 using pEDMR will therefore reveal only T_2 of ^{31}P donor electrons in close proximity to the *c*-Si:P/SiO_2 interface defects. In contrast, a T_2 measurement using conventional microwave-detected pEPR will reveal the coherence time of ^{31}P donors in the bulk as the contribution of near-surface ^{31}P atoms in the pEPR signal will be negligible in comparison to the magnitude of the bulk ^{31}P signal. Thus, the comparison of T_2 times measured by pEDMR and pEPR allows the influence of interface defects on the ^{31}P donor electron-spin-coherence times to be studied. It shall be noted that, in the following, the constant T_2 is used for all decay time measurements of Hahn echo decays as the pEPR detected Hahn echo decays represent the transverse relaxation T_2 for the bulk donor electrons. It must be emphasized though that the nature of the observed transition may be of completely different physical origin than transverse spin relaxation and the identification of the nature of this process is the motivation for these experiments.

The pEPR and pEDMR experiments require different approaches to the measurement of T_2 times: with pEPR, the T_2 times of paramagnetic centers can be determined most easily using a Hahn echo pulse sequence [4]. Hahn echoes are a temporary rephasing of a spin ensemble due to a pulse sequence consisting of an initial $\frac{\pi}{2}$ pulse which turns the ensemble polarization into the plane perpendicular to the B_0 field and a subsequent pulse which initiates the phase reversal [5]. As illustrated in the inset sketch in Fig. 3.2 (b), when the echo pulse sequence consists of the $\frac{\pi}{2} - \pi$ pulses with a duration τ between the pulses, a Hahn echo can be observed at a time τ after the second pulse, which is the time 2 τ after the first pulse. When a Hahn echo is observed, T_2 times can be measured by determining the decay of the Hahn echo as a function of twice the pulse separation time 2τ.

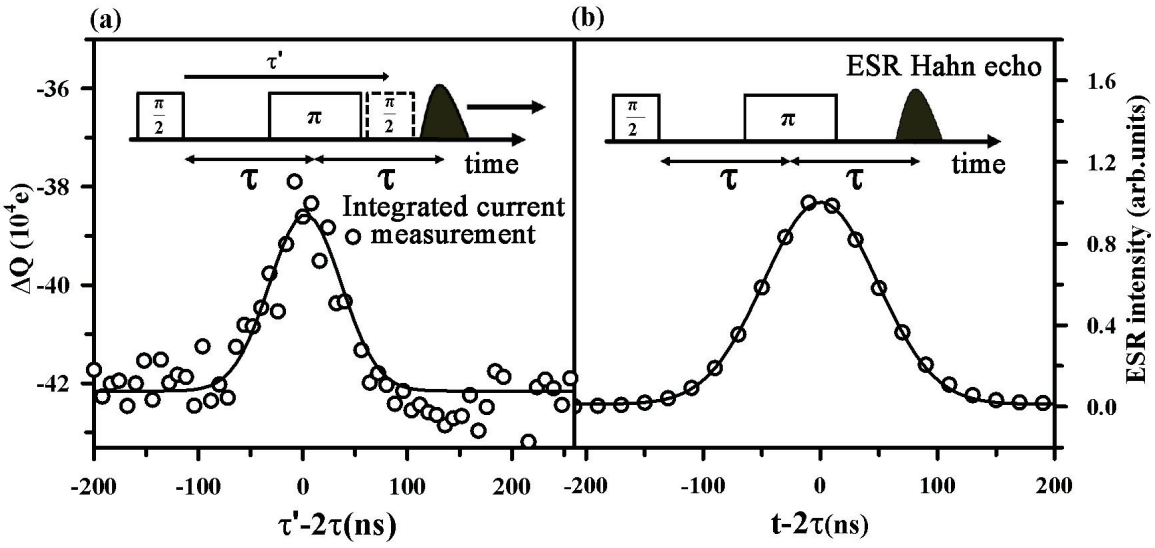

Figure 3.2: Comparison of (a) an electrically detected spin-echo with $\tau = 300$ ns and (b) a conventional microwave detected Hahn echo with $\tau = 10$ μs. The data sets were recorded on the same sample, under identical sample conditions (T= 10 K, $I = 250$ μA, $\theta = 90°$) during the same experimental run on resonance with the low field phosphorous line. Both data sets were fit with Gaussian functions (solid line). Insets of the two plots show sketched timelines of the used pulse sequences.

Fig. 3.2 (b) shows a data set for a Hahn echo transient obtained from a ^{31}P-doped c-Si sample with $^{31}\mathrm{P} = 10^{16}\ cm^{-3}$ at a temperature T = 10 K and with $\theta = 90°$. One can clearly see a local maximum of the transient microwave signal at a time t = 2τ. The data set was well fit by a Gaussian function with a half width of σ =24.4(2) ns. In the following, Gaussian fits are used to determine the integrated intensities of all pEPR and pEDMR detected Hahn echoes.

In contrast to pEPR measurements, pEDMR does not allow direct observation of Hahn-spin echoes through real time transient measurements as the integrated sample current Q always represents a projection of the spin state at the end of the pulse sequence onto a singlet state. Therefore, the T_2 time measurement using pEDMR requires the utilization of a modified Hahn echo pulse sequence that is illustrated in the inset of Fig. 3.2 (a) [4].

In order to resolve the dynamics of the spin ensemble during and after the $\frac{\pi}{2} - \pi$ pulse sequence, a third pulse with length $\frac{\pi}{2}$ is applied at a time after the beginning of a conventional Hahn echo pulse sequence. The third pulse projects the spin ensemble at the time $\tau^{'}$ onto the $\hat{z}$ direction, which in turn determines the singlet content of the ^{31}P interface-defect pair. The charge Q integrated following this pulse therefore represents the polarization of the spin ensemble along the $\hat{x}$ axis ($\hat{y}$ axis) at the time $\tau^{'}$ (assuming the B_1 field is directed along the $\hat{y}$ axis ($\hat{x}$ axis)). The measurement of the entire echo transient using the pEDMR detection requires repetition of the echo sequence for various $\tau^{'}$: the third pulse (also called the detection pulse) is swept through the time range which covers the Hahn echo maximum as well as the echo base line. While this procedure makes the time needed for T_2 measurements significantly longer, it allows the measurement of a T_2 using pEDMR. The plot displayed in Fig. 3.2 (a) shows an electrically detected spin echo measured on the same sample and under identical conditions, recorded during the same experimental run as the measurements shown in Fig. 3.2 (b). The data clearly show the echo whose fit with a Gaussian function is displayed by the solid line. The fit revealed a half width of =192 ns. The comparison of the two echo functions shows that the electrically detected echo is narrower than the microwave-detected echo, indicating that the former is due to a more heterogeneous spin ensemble.

The use of two different measurement techniques (pEDMR and pEPR) raises the question of whether both methods probe the same observable, namely, T_2 of ^{31}P impurity atoms. There has recently been a comparative study of T_2 times confirming this identity using a pEDMR detected spin-dependent bulk process [6] (a spin-trap process of ^{31}P in c -Si that becomes relevant at high magnetic fields) which showed that both pEDMR and pEPR measured T_2 times reveal an excellent agreement. Thus, in the following, systematic measurements comparing pEPR-detected T_2 times of ^{31}P bulk impurities and pEDMR-detected T_2 times of ^{31}P interface impurities are presented. These measurements are made for three reasons: (i) to extend the previous observation of electrically detected Hahn echoes [4] to c -Si(111) surfaces, (ii) to measure the temperature dependence of the T_2 times, and (iii) to obtain comparable measurements with both pEPR and pEDMR under identical conditions but with completely different detection channels.

3.2.2 Measurement of spin-echo decays

The spin-echo effects shown in Fig. 3.2 are imprints of coherent spin motion on currents or radiation intensities. When a spin ensemble loses coherence during a $\frac{\pi}{2}-\pi$ sequence, the intensity of the spin echo following this sequence decays. Quantifying the decay of Hahn echoes is a direct measure of the coherence time T_2(46). Fig. 3.3 displays a set of electrically detected Hahn echoes as well as a plot of the integrated echo intensities obtained from them, recorded on a sample with P =10^{16} cm^{-3} at magnetic fields in resonance with the high-field ^{31}P peak at T = 10 K and $\theta = 90°$, and with a sample current of I =250 μA.

One can clearly see the gradual decay of the echo intensity with increasing pulse separation time. The solid line of the plot in Fig. 3.3 displays a set of the intensity data with a modified exponential function

$$I(2\tau) = e^{-\frac{2\tau}{T_2}-\frac{8\tau^3}{T_S^3}} \tag{3.3}$$

which contains a contribution due to a single exponential T_2 decay as well as the stretched exponential contribution due to the isotopical influence of the ^{29}Si which causes spin-diffusion with time constant T_S [6, 7]. The plot in Fig. 3.3 exhibits a good agreement of the echo decay with the fit function and thus, by using this

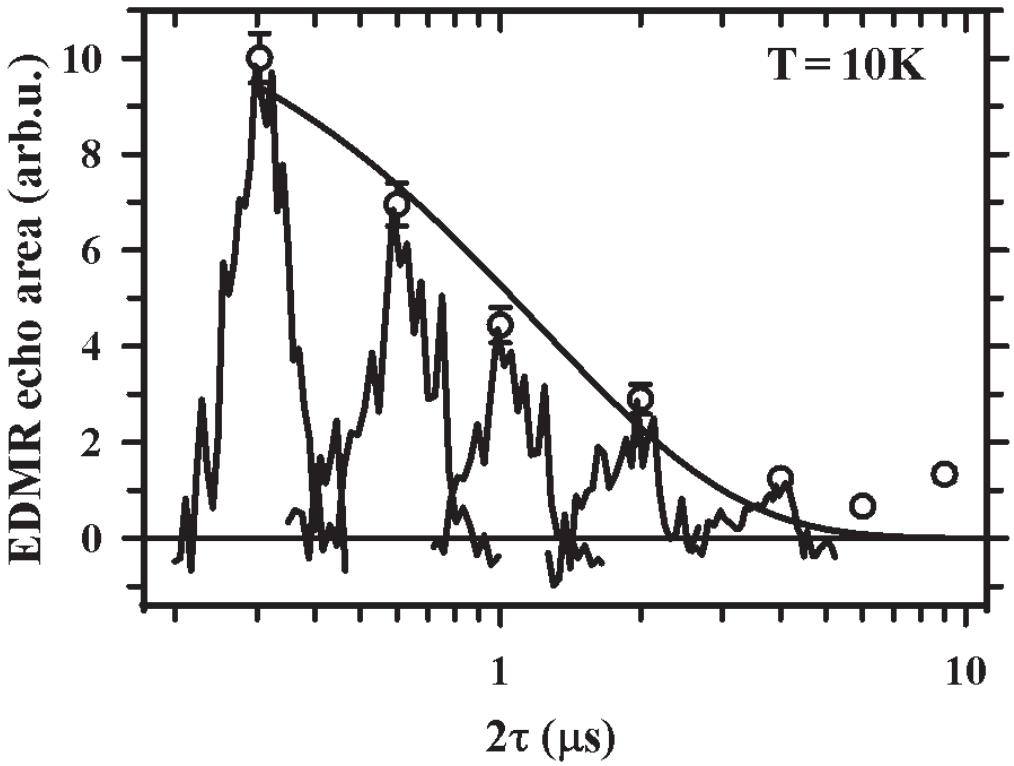

Figure 3.3: Plot of integrated intensities of the electrically detected echoes as a function of 2τ recorded with pEDMR on a c-Si:P/SiO_2 sample with [P] = 10^{16} cm^{-3} on resonance with the low field ^{31}P line. The solid line represents a fit with a modified multi-exponential decay function (see text), the small inset plots represent plots of echo data sets.

method for both pEDMR as well as pEPR-detected echo decay measurements, the T_2 times of ^{31}P impurities can be determined for the c-Si:P bulk and the c-Si:P/SiO_2 interface, respectively. Note that all pEPR-detected and most pEDMR-detected echo measurements were conducted on the low field peak of the hyperfine split ^{31}P resonance.

In order to confirm that the spectral proximity of the P_b-peak to the low field ^{31}P resonance under the given experimental conditions does not distort the electrical T_2 measurements, control measurements were carried out on the high field ^{31}P peak for $T = 5K$. The values obtained under these conditions are $T_2 = 1.2(3)\mu$s for the low field peak and $T_2 = 1.9(8)\mu$s for the high field peak. Within the given error margins, the results of these control measurements (Fig. 3.4, blue solid diamonds) are in agreement with the measurements obtained from the low field ^{31}P resonance and also, they are in good agreement with the measurements conducted at c-Si (100) surfaces [4] which had been treated in a similar manner (native oxide).

3.2.2.1 Temperature dependence of T_2 times

The measurement of T_2 as described above was repeated for the low field resonance on the same sample with pEPR at temperatures $T = 5$ K, 8 K, 10 K, 11 K, 12 K, 13 K, 15 K and with pEDMR at temperatures of $T = 5$ K, 10 K, 13 K. The integrated echo intensities of these measurements are plotted in Fig. 3.4 along with the results of their fit with Eq. 3.3. The comparison of the pEDMR and the pEPR data sets shows that while there is a strong temperature dependence of the echo decay for the pEPR data, the pEDMR decay is faster and, within the range $T = 5$ K to 13 K, nearly constant. In order to analyze these observations quantitatively, the fit results for T_2 are plotted for both the pEDMR and the pEPR measurements in an Arhenius plot in Fig. 3.5.

The coherence time of the bulk ^{31}P donors, T_2, determined via pEPR, is well fit with a function of the form:

$$\frac{1}{T_2} = Ae^{\frac{-\Delta E}{k_B T}} + \frac{1}{T_0} \tag{3.4}$$

where ΔE is an activation energy, and $1/T_0$ a constant relaxation rate independent of temperature. The best fit occurs with $\Delta E = 9.1 \pm 0.5$ meV and $1/T_0 = 10 \pm 1$

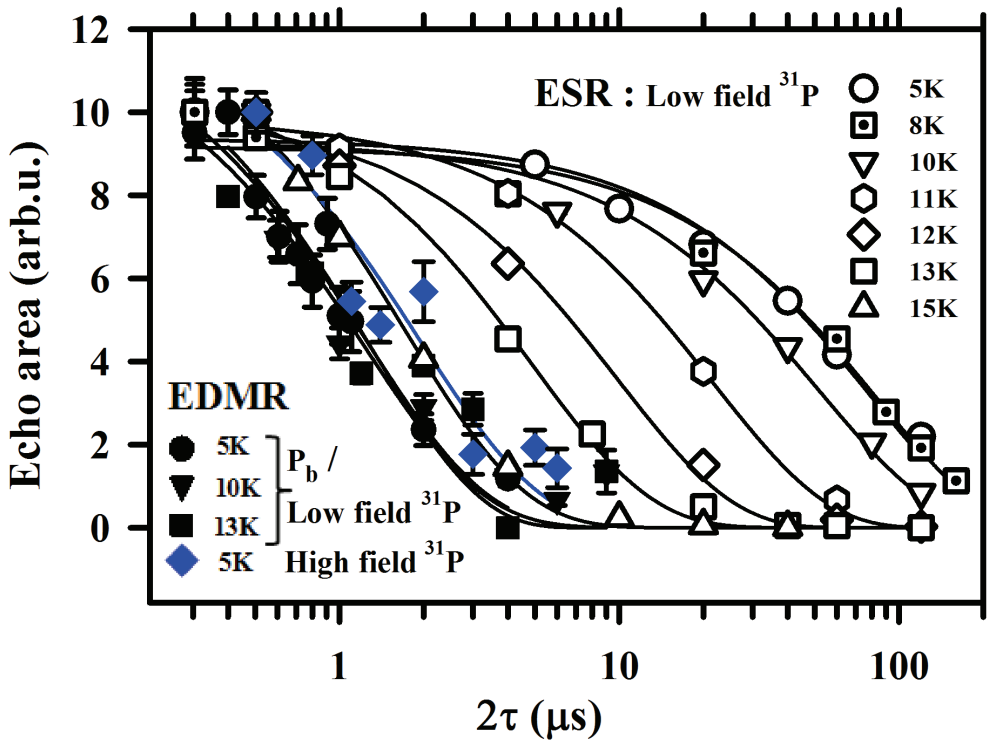

Figure 3.4: Plot of the normalized integrated echo intensity of pEPR and pEDMR detected Hahn echoes as a function of the logarithms of the pulse separation time τ for various temperatures. The data sets were fit with the modified exponential function given by Eq. (3.3). All pEDMR and pEPR measurements were conducted on the same samples during the sample experimental run. Most of the data points were recorded on resonance with the low field phosphorous line except for the blue colored data points which were recorded on resonance with the low field phosphorous line.

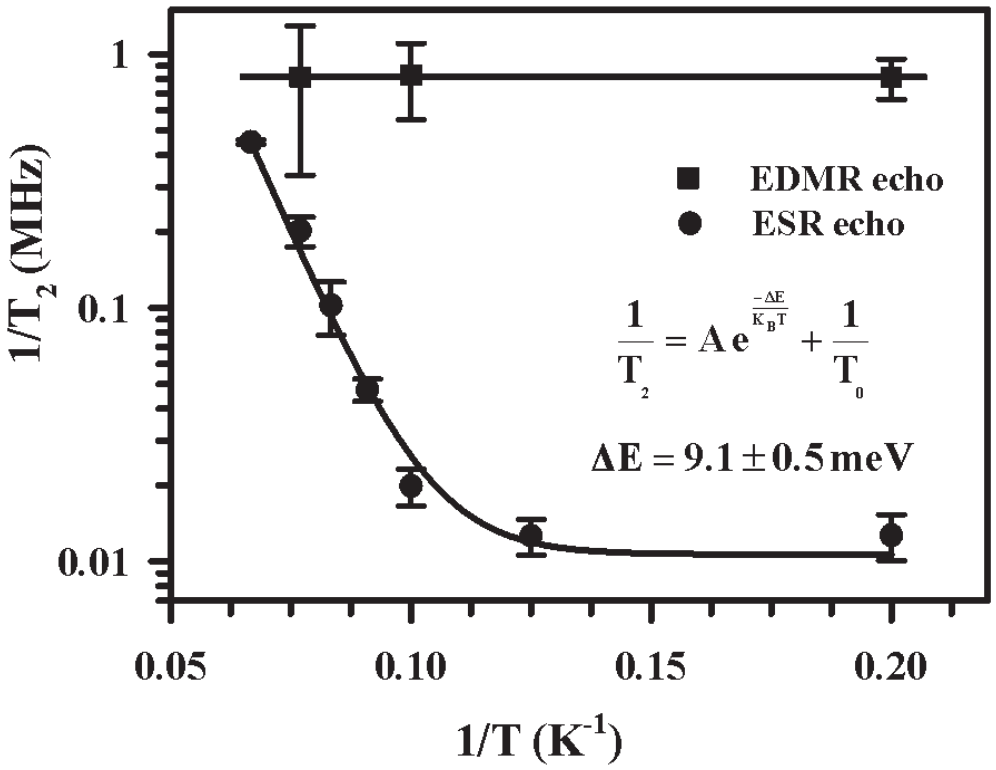

Figure 3.5: Plot of the logarithm of coherence decay rate T_2^{-1} obtained from the data shown in Fig. 3.4 as a function of the inverse temperature T^{-1}. The solid lines are fits of the data. The pEDMR data are fit with a constant function. The pEPR is fit with a combination of a constant function and a temperature-activated Boltzmann factor.

kHz.

3.2.2.2 Discussion

As the pEDMR and the pEPR data displayed in Fig. 3.5 were collected on the same sample in the same experimental run, it is clear that the pEDMR measured T_2 times of ^{31}P donor spins in close proximity to interface defects are significantly shorter than the pEPR measured T_2 times and, within the error, independent of the temperature. At the same time, the pEPR measured T_2 of the bulk ^{31}P donor spins is not only longer than the pEDMR measured ^{31}P donor spins, it is also highly temperature dependent. In the temperature range from $T = 5$ K to 15 K, the coherence time changes by about a factor of 50, exhibiting a good agreement with the previously demonstrated thermal activation [7] of ^{31}P in a *c*-Si environment with a natural abundance of the ^{29}Si isotope.

The comparison of T_2 of ^{31}P in proximity to interface defects with those in the bulk therefore shows that interface defects significantly shorten the donor electron spin coherence time. Within the given temperature range, T_2 appear to be pinned at ≈ 1.3 μs, a value which has been observed previously for electrically detected ^{31}P spins in *c*-Si samples with different surface orientations, donor concentrations and experimental conditions [3, 4].

The independence of the donor spin coherence time of near interface defect ^{31}P atoms from experimental conditions, including temperature, suggests that in contrast to bulk donors, T_2 of the near-surface donors is not determined by (^{31}P-^{31}P) spin-spin or spin-lattice interactions but by processes directly related to the interface defects in their immediate proximity.

We identify two possible origins for the drastic quenching of the ^{31}P donor electron spin T_2 time in proximity of interface defects described above:

(i) The electronic transition between the ^{31}P donor state and the P_b center. This occurs when the donor electron falls into the doubly occupied interface ground state. The electronic transition leaves both the ^{31}P donor and the interface state diamagnetic since there is no donor spin present after the transition and the interface state is a doubly occupied singlet state.

(ii) Spin flip-flops of interface states which significantly quench the T_2 relaxation of ^{31}P donor spins in their proximity, as suggested by de Sousa. [8].

The electronic transition is a limitation to both T_1 as well as T_2 processes of the spin-pairs as it destroys the pairs. When the electronic transition determines the measured T_2 times, both the electrically measured T_2 and T_1 times should be equal. This is in contrast to the general case of spin relaxation in absence of electronic transitions when $T_2 \leq 2T_1$ and also in contrast to the case when the interface state induced enhancement of the ^{31}P T_2 relaxation keeps the T_1 either unchanged or significantly slower than the T_2 time. In this latter scenario, the electronic transition time will be longer than the P_b induced T_2 time and thus, the electrically measured T_1 time will be given by either the real T_1 time or the electronic transition time and it should therefore be significantly longer than the electrically measured T_2 times.

For clarity, Table 3.1 shows the expected measurement outcomes for electrically detected Hahn echo and inversion-recovery experiments, for a number of different relationships between the underlying T_1, T_2 and electronic transition times T_{elec}. Note that the term "electronic transition time" used here refers to the singlet transition probability.

Since the permutation symmetry of the resonantly excited pairs shuttles back and forth between singlet and triplet states during Rabi-nutation experiments (and thus, during both Hahn echo and inversion recovery experiments), its is the dominating singlet transition, not the slow triplet transition, which determines the measured decay times when electronic transition times are shorter than any spin relaxation time.

3.2.3 Comparison of T_2 and the longitudinal relaxation time T_1 of ^{31}P donor electrons at the *c*-Si:P/SiO$_2$ interface

3.2.3.1 Electrical detection of spin inversion

In order to probe T_1 of near interface ^{31}P, electrically detected inversion recovery experiments were carried out at a temperature of $T = 5$K, where pEPR measurements of bulk ^{31}P donor spins reveal large differences between T_1 and T_2 times [7]. The idea behind the inversion recovery experiment [5] is to invert the steady state spin

Table 3.1: Expectation for the observed time constants in electrically detected inversion-recovery and Hah-echo experiments for a number of different relationships between the T_1, T_2 and electronic transition times. We note that in the main text, the expected results are refereed to as T_1 and T_2, respectively, even when they may be due to electronic transitions.

relationship	^{31}P		low field ^{31}P/P$_b$	
	Inversion-Recovery	Hahn Echo	Inversion-Recovery	Hahn Echo
$T_{\text{elec}} << T_2^{^{31}P}, T_2^{P_b} << T_1^{^{31}P}, T_1^{P_b}$	T_{elec}	T_{elec}	T_{elec}	T_{elec}
$T_2^{^{31}P}, T_2^{P_b} << T_{\text{elec}} << T_1^{^{31}P}, T_1^{P_b}$	T_{elec}	$T_2^{^{31}P}$	T_{elec}	$T_2^{P_b}$
$T_2^{^{31}P}, T_2^{P_b} << T_1^{^{31}P}, T_1^{P_b} << T_{\text{elec}}$	$\frac{T_1^{^{31}P} T_1^{P_b}}{T_1^{^{31}P} + T_1^{P_b}}$	$T_2^{^{31}P}$	$\frac{T_1^{^{31}P} T_1^{P_b}}{T_1^{^{31}P} + T_1^{P_b}}$	$T_2^{P_b}$

polarization and to then observe transiently the gradual return toward the equilibrium due to T_1 processes. Thus, the experiment consists of an initial inversion pulse, a defined delay time τ'' during which the spin ensemble undergoes T_1 relaxation and a subsequent polarization measurement which is typically conducted by utilization of a Hahn echo sequence with fixed pulse separation time τ. Fig. 3.6 displays a sketch of the pulse sequence used for the electrical inversion recovery measurements presented in the following. Similar to the Hahn echo decay measurements, the Hahn echo is measured with pEDMR by repetition of the experiment whilst applying projection pulses which are gradually swept through the echo sequence. The data in Fig. 3.6 show an inverted Hahn echo recorded with a short $\tau = 252$ ns and an even shorter delay time $\tau'' = 52$ ns producing strong inversion. The experimental data were collected at a B_0-field in resonance with the high field ^{31}P line which is well separated from the P$_b$ resonances. It shows that in contrast to the positive spin echo as detected for a simple Hahn echo sequence, the sign of the echo is negative. To the knowledge of the authors, the data shown in Fig. 3.6 are the first demonstration of an electrically detected spin inversion experiment. Similar to the T_2 times discussed above, the variable T_1 is used in the following for all recovery times of inversion recovery experiments since the pEPR detected inversion recovery of the bulk donor electrons represents the longitudinal

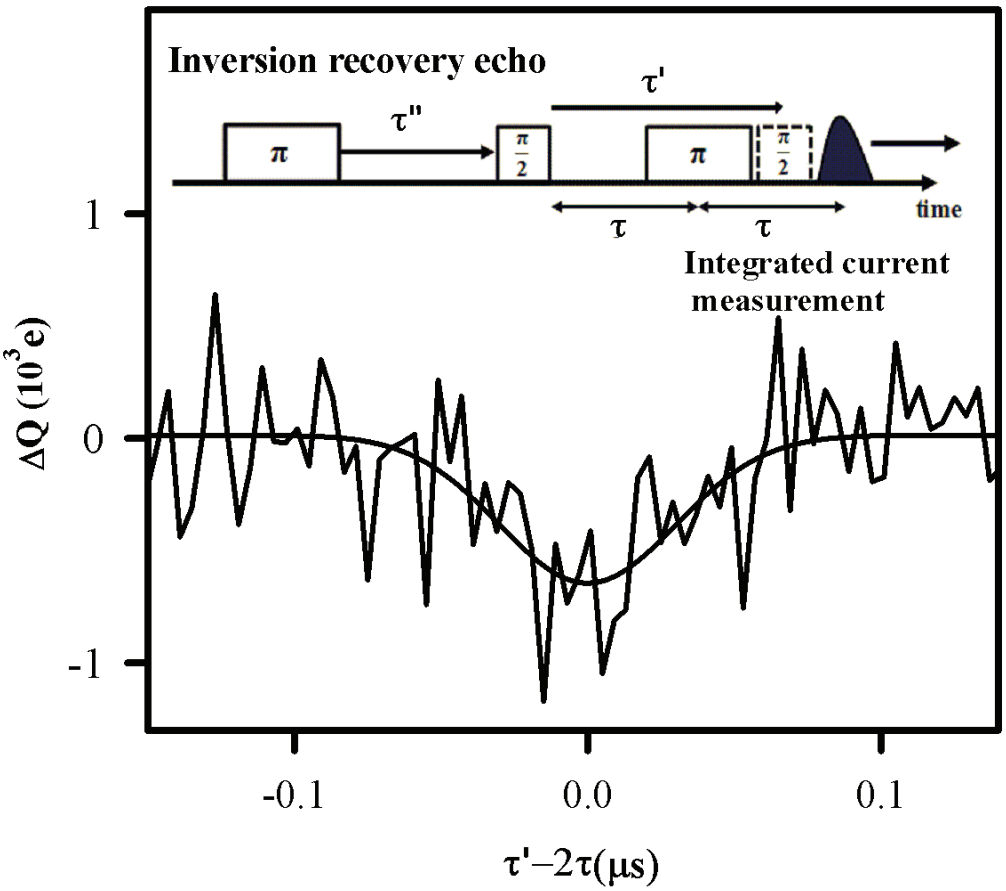

Figure 3.6: Demonstration of an electrically detected spin inversion recovery experiment. The inset is a sketch of the inversion recovery pulse sequence which consists of the Hahn echo sequence that is preceded by an inversion (π-) pulse at a time τ'' before the Hahn echo sequence begins. Similar to the electrically detected Hahn echo shown in Fig. 3.2, a projection pulse is shifted through the sequence during different repetitions of the experiment. The main plot displays an echo recorded by plotting Q as a function of the difference $\tau' - 2\tau$ between the projection pulse begin τ' and the echo maximum at 2τ.

relaxation time T_1. It is important to note that by using this notation for the pEDMR detected inversion recovery times, T_1 may actually quantify a process of completely different physical origin than longitudinal relaxation, such as the electronic transition between the phosphorous and the interface defect. The possible relationship between the measured times and the underlying processes are summarized in Table 3.1.

3.2.3.2 Inversion recovery of near interface defect ^{31}P donor electrons

In order to determine the T_1 times of the ^{31}P donor electron, the experiment shown in Fig. 3.6 was repeated for seven values of τ'' in the range of 52ns $\leq \tau'' \leq 20\mu$s. The results of these experiments are displayed in Fig. 3.7. They show that the polarization inversion that exists directly after the inversion pulse (τ'' is very small) exponentially approaches the steady state polarization with increasing τ''. The integrated echo amplitudes were obtained from a fit of the echo data with Gaussian functions. Their dependence on τ'' shows an excellent agreement with an exponential decay function with a negative offset

$$M(\tau'') = M(0)\left[1 - 2e^{-\frac{t}{T_1}}\right]. \tag{3.5}$$

The time constant $T_1 = 4.0(5)$ μs obtained from this fit is more than six orders of magnitude shorter than the previously investigated bulk T_1 times [7] which shows that the proximity of P_b centers leads to dramatically reduced T_1 times.

3.2.3.3 Discussion

The measurement of $T_1 = 4.0(5)$ μs of ^{31}P donor electrons in proximity of interface defects reveals a value that is quenched by orders of magnitude compared to bulk ^{31}P T_1 times. It can therefore be concluded that the measured T_1 of ^{31}P donor electrons near interface states times is governed not by the same T_1 processes that act on bulk donor electrons but instead by the spin-dependent ^{31}P-P_b transition.

The electrically detected T_1 time is longer than the electrically detected T_2 times for the two ^{31}P resonance peaks that were measured at a temperature of $T = 5$K. Note that the EDMR signal of the low field ^{31}P peak overlaps with interface defect signals which explains why its value of $T_2 = 1.2(3)$ μs differs from the high field ^{31}P which shows $T_2 = 1.9(8)\mu$s. The differences between T_1 times and the two T_2

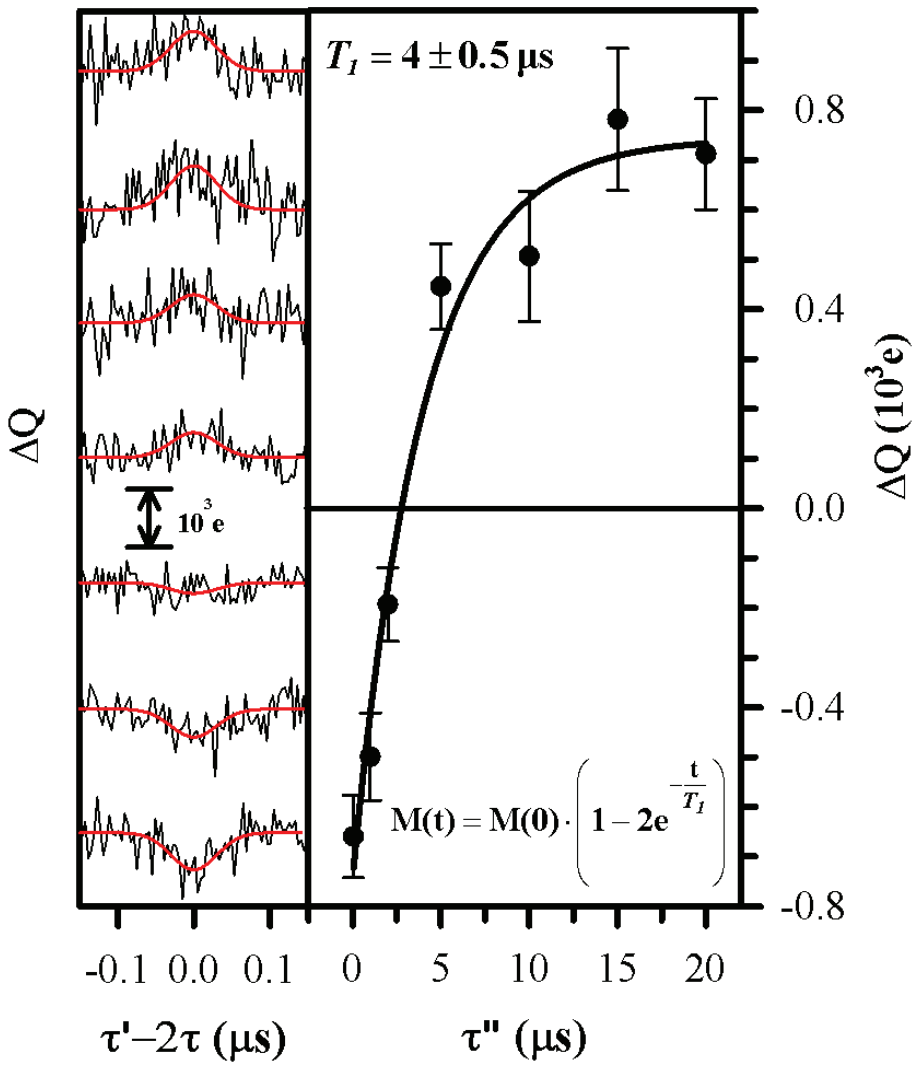

Figure 3.7: Plot of the integrated echo intensity detected with the pulse sequence shown in Fig. 3.6 as a function of the inversion recovery time τ''. The solid line represents a fit of the data with a single exponential function. Note that the inverted echo for small τ'' changes into a noninverted echo with equal magnitude for large τ''. The inset plots on the left show the raw data of the various echo measurements as well as fits with Gaussian functions which are the basis for the integrated echo intensities.

values reveals 2.8(6) μs and 2.1(9) μs, for the low field and high field ^{31}P resonances, respectively. Thus, while it is likely that $T_2 < T_1$, there is only limited statistical support for the measured difference between the T_1 and T_2 times.

3.2.4 Comparison of T_2 and T_1 times at different interface defect densities and different pair-partner resonances

In order to corroborate the observation that electrically detected ^{31}P donor electron relaxation times $T_2 < T_1$, and that T_1 and T_2 are independent, electrically detected Hahn echo decay and inversion recovery experiments were repeated on the high and low field resonance lines of the ^{31}P donor electrons on a sample with a different interface defect density.

3.2.4.1 Testing the independence of T_1 and T_2 relaxation times

In order to test the conclusions given in section 3.2.3.3, the Hahn echo and inversion recovery experiments presented above were repeated on a sample with identical ^{31}P density ($[^{31}\mathrm{P}]=10^{16}\mathrm{cm}^{-3}$) but reduced interface defect density. This was accomplished by preparing the pEDMR sample in an identical way to the sample used for the measurements in Section 3.2.3, followed by a thermal anneal at $T = 500$K. It is well known [9] that the thermal activation of c-Si(111)/SiO_2 interface leads to a structural relaxation which greatly reduces the number of interface states. Based on the parameters used [10], we estimate a reduction of the interface state density by a factor of four, thus increasing the average distance between interface defects by a factor of two.

Two outcomes of this decrease in defect density are anticipated. First, the increased separation between defects may lead to an increase in the defect T_1 time. Second, the decreasing defect density should also increase the "main-pair distance" (as defined in Section 1.4) monotonically (but nonlinearly). As this would reduce the transition times between the ^{31}P donor and the interface defect, we expect the electrically detected T_1 time to increase, if they are determined by the transition time. In both cases, we expect the T_1 time measured using an electrically detected inversion recovery experiment to increase when the defect density is reduced. We do

not, however, expect to increase the measured T_2 times in the same way if they are dominated by the local interface fields. In contrast, when T_2 is mostly governed by the electronic transition, it is expected to follow the changes of the T_1 times.

Fig. 3.8 displays the results of pEDMR-detected inversion recovery experiments measured on both the ^{31}P high field and low field/P_b resonances of the annealed sample. The data are plotted on integrated echo intensity scales which are normalized to the noninverted Hahn echoes (for large τ''). As for the data in Fig. 3.7, the integrated echo intensities were determined using a Gaussian fit. Because the low field ^{31}P and the P_b signals overlap, the low field ^{31}P/P_b echo signals have different signal strengths and thus different relative noise levels exist for the two resonances. The plots of the echo intensity as a function of the inversion time τ'' confirms again the presence of an inverted signal directly after the inversion pulse, which gradually changes into a noninverted Hahn echo as τ'' is increased. The two measurements reveal echo inversion times of $T_1 = 13.3(3)$ μs and $T_1 = 14.3(3)$ μs for the low field and high field signals, respectively. In spite of the fact that the low field measurements included contributions from the ^{31}P and the P_b signals, both measurements are within two standard deviations (the difference is 1.0(5) μs) and at the same time they are significantly longer than the T_1 times measured on the nonannealed sample as expected for an interface with a reduced density of interface states.

In order to compare the T_1 times and the T_2 times of the annealed sample, we conducted Hahn echo decay measurements on both ^{31}P resonances. In contrast to the T_1 measurements, these echo decays were measured at various temperatures between $T = 5$K and $T = 12$K. The echo decay functions were fit with the same procedure used for the nonannealed sample (see Section 3.2.2). The results of these fits are plotted in Fig. 3.9. For the low field ^{31}P/P_b resonance, they confirm the observations made on a native oxide qualitatively and quantitatively - the value of T_2 is independent of the temperature at $\approx 1\mu$s. The measurements also confirm that T_2 measured solely on ^{31}P (by measuring on the high field resonance) is increased and, due to the improved relative errors, one can state that it is significantly longer than the value measured on the high field ^{31}P/P_b peak and significantly shorter than the measured T_1 time. The high field ^{31}P T_2-time also remains constant between $T = 5$K and $T = 8$K. At higher

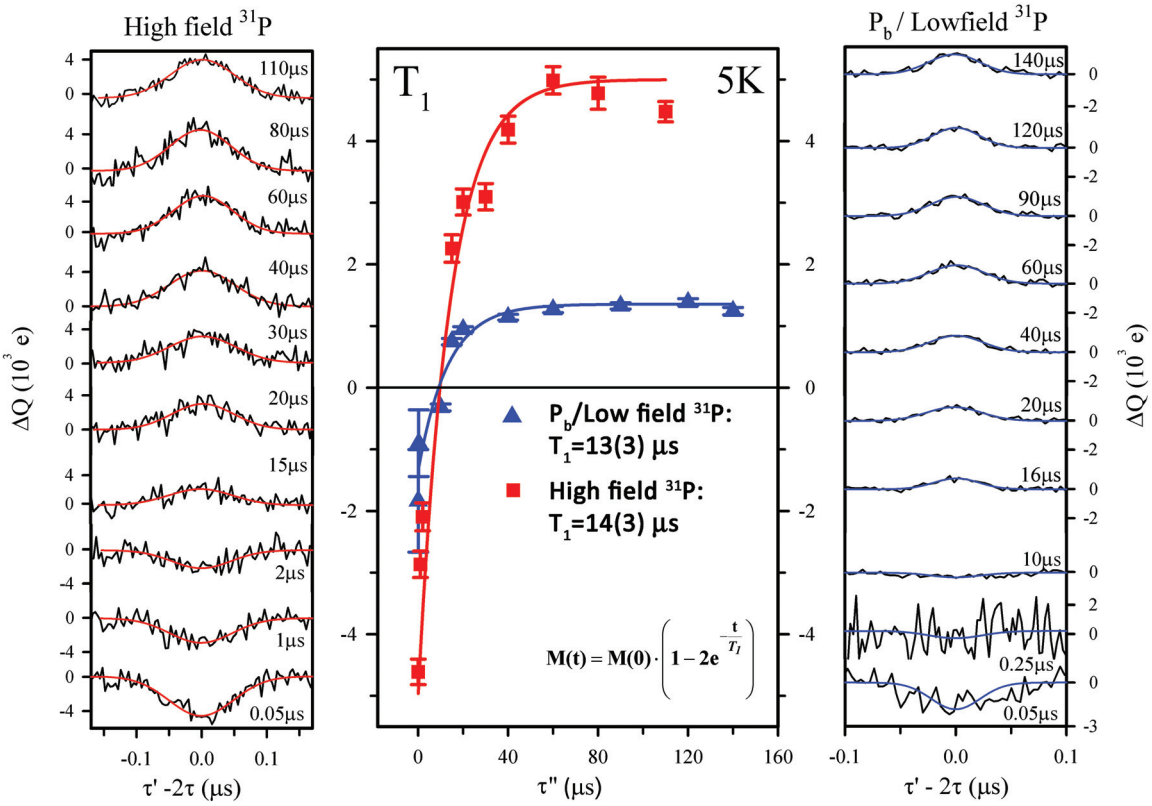

Figure 3.8: Electrically detected inversion recovery measurements of electron spins on the low field ^{31}P/P$_b$ resonance and the high field ^{31}P resonance measured on an annealed sample at $T = 5$K. The values of τ'' are listed next to the plotted echoes. The data are normalized to the echo measured with large τ''. Within the given error ranges, the two data inversion recovery plots show similar T_1 time. This T_1 times are increased in comparison to the T_1 time of the nonannealed sample.

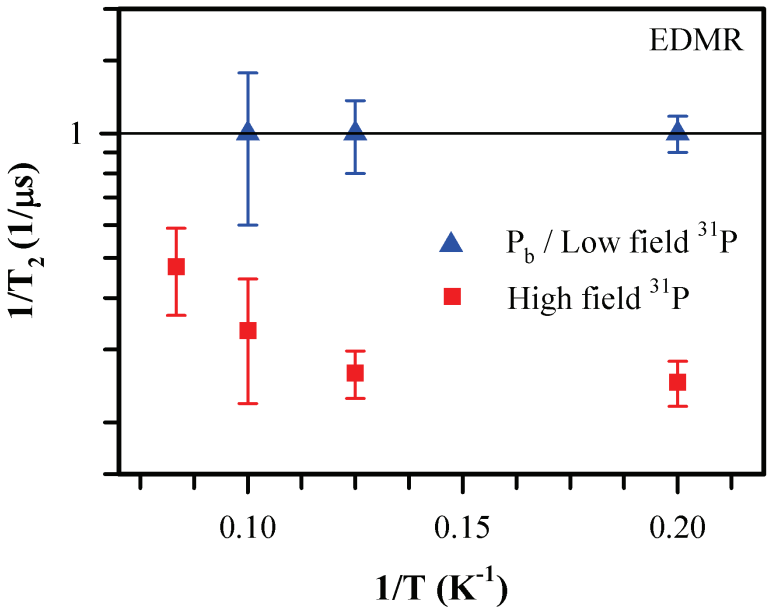

Figure 3.9: The results of electrically detected Hahn echo decay measurements of electrons spins at on the low field $^{31}\mathrm{P}/\mathrm{P}_b$ resonance and the high field $^{31}\mathrm{P}$ resonance measured on an annealed sample at temperature between $T = 5\mathrm{K}$ and $T = 12\mathrm{K}$.

temperatures, the value decreases, as seen in conventional pEPR experiments [7].

3.2.4.2 Discussion

Table 3.2 summarizes the the results of T_1 and T_2 measurements for both the low field ^{31}P/P$_b$ and high field ^{31}P resonance, for the two different interfaces, at a temperature of $T = 5$K. The measurements made on the annealed sample confirm qualitatively the behavior of T_1 and T_2 times obtained from the nonannealed sample: The T_2 times of ^{31}P donor electrons near interface defects are significantly shorter than the T_2 times of ^{31}P donor electrons in the bulk.

The identical measured T_1 times seen for both the ^{31}P and P$_b$ may be explained in two ways, as can be seen from Table 3.1 In one case, the electronic transition may be much faster than the underlying T_1 process. Here, the electronic transition time, T_{elec}, determines the measured T_1 time, and corresponds to the faster of the two spin-pair decay times, namely the singlet electronic transition.

An alternate explanation is that one (or both) of the pair-partners has an underlying T_1 time faster than the electronic process. In that case, the electrically detected inversion recovery measurement will reflect that time for experiments undertaken on *either* partner, as we measure the relative orientation of the two spins, and not the absolute orientation observed in conventional EPR experiments. Indeed, T_1 times measured in any pair-system using the electrically detected inversion recovery method described here should always result in identical T_1 times for both pair-partners. We are thus unable to distinguish the underlying cause of the measured reduction of the ^{31}P T_1 time - it may be due to a real reduction of the T_1 time due to its environment, the intrinsic T_1 of the partner P$_b$ spin, or the electronic transition between them. We note that, if the electrically measured T_1 and T_2 times had been identical, we would be confident that the electronic transition was the dominant mechanism.

3.3 Conclusions

The data presented and discussed above strongly supports the model for spin-dependent recombination via ^{31}P donors and interface defects that was presented by Stegner et al. [3]. Whilst this explanation for the observed EDMR signal has become commonly accepted, and is further supported by the results presented here,

Table 3.2: PEDMR detected inversion recovery times (T_1) and Hahn echo decay times (T_2) recorded on the high and low field resonances at a temperature $T = 5$K for both the nonannealed (native) and the annealed silicon-to-silicon dioxide interface.

resonance line	high field ^{31}P		low field ^{31}P/P$_b$	
interface condition	native	anneal	native	anneal
pEDMR T_1	4.0(5)μs	14(3)μs	–	13(3)μs
pEDMR T_2	1.9(8)μs	4.0(5)μs	1.2(3)μs	1.0(2)μs

the possibility remains that other processes also contribute to the resonant changes in current. Given the now significant evidence supporting the ^{31}P-P$_b$ model [3, 4, 11], we agree with the conventional understanding and conclude here that we are indeed observing spin-dependent transitions between ^{31}P donors located close to P$_b$ defects at the Si(111)/SiO$_2$ interface.

The measurement of the T_2 times of ^{31}P near c-Si(111)/SiO$_2$ interface defects with electrically detected echo decay experiments shows that the T_2 times of the two weakly spin coupled pair-partners are significantly different, and that both are significantly shorter than the T_1 times. We conclude from this observation that the measured T_2 times of the P$_b$ center and the ^{31}P donor electron are not primarily governed by the electronic transition and that due to the weak spin coupling, the transverse spin relaxation of the two pair-partners are determined by different mechanisms.

Since T_2 of ^{31}P in interface defect proximity is quenched drastically compared to bulk ^{31}P, and since this quenching is not due to the electronic transition, we conclude that the interface state-induced T_2 process described by De Sousa [8] is responsible for the observed ^{31}P-T_2 times. The description of this mechanism predicts a relationship $T_2 \propto \frac{1}{\sqrt{n}}$ between the transverse spin relaxation time T_2 of near interface ^{31}P donor electrons and the interface density n. For the given anneal parameters, literature [10] predicts a ratio $\frac{n_n}{n_a} \approx 4$ between the native interface density n_n and the annealed interface density n_a. Thus, the literature values of the T_2 times before and after anneal is expected to be $\frac{T_2^a}{T_2^n} \approx 2$. The experimentally observed value of $\frac{T_2^a}{T_2^n} = 2.1(9)$ as obtained from the high field ^{31}P peak measurements in Table 3.2 is in full agreement with these predictions.

The confirmation of the De Sousa model allows a prediction of the distance of

the interface from those ^{31}P atoms which contribute to the observed pEDMR signals. Assuming a native oxide interface state density of $n_n = 10^{13}$ cm^{-3}, we arrive at a ^{31}P to interface distance of $d \approx 4$ nm. Given the size of the s-shaped ^{31}P donor electron wave-function envelope, we conclude that this is a reasonable value. We note, however, that this agreement occurs even though we are violating one of the assumptions of the De Sousa model - in these experiments, the average distance between interface defects is smaller than the distance of the ^{31}P from the interface.

Our results have implications for quantum information concepts which aim to utilize ^{31}P donor spins close to the c-Si(111)/SiO_2 interface as qubits. The data presented above show that, without the ability to oppress the noise induced by interface defects, the extremely long coherence times of the ^{31}P qubits seen in bulk ^{31}P measurements are completely obliterated. This insight is particularly important for interface defect-based readout concepts. Even if ways are found to reduce the incoherence induced by these interface states, incoherence due to electronic transitions into the interface states will still need to be controlled, e.g. by control of the coupling between target and probe spins. This may be achieved by utilizing the Stark effect, as electric fields will have a stronger effect on the localization of the slightly delocalized ^{31}P donor wave function in comparison to the extraordinary strongly localized deep interface defects. Whether these different electric field sensitivities have a significant impact on the exchange coupling between the ^{31}P donor interface states in close proximity at sufficiently low fields remains to be seen.

Finally, we note that the ability of spin-dependent transitions to reduce coherence times need to be considered for other potential ^{31}P readout mechanisms discussed in the literature, such as spin-dependent scattering of conduction electrons by donor spins in two-dimensional electron gasses [12–17].

3.4 Summary

In summary, we have investigated spin-dependent processes at the c-Si:P/SiO_2 interface using pEDMR, and shown that spin-dependent ^{31}P-to-interface defect recombination takes place at the c-Si(111) surface in a similar way to that seen with c-Si(100) surfaces. The imprints of spin-dependent recombination on interface cur-

rents reveal EPR resonances of the hyperfine split ^{31}P resonance and P_b defects. At least one other defect is also seen, previously unobserved in ^{31}P doped samples, and assigned here to the unrelaxed E' defect in the SiO matrix. The correlation measurements of the dynamics of these pEDMR detected signals strongly support the model that recombination transitions between ^{31}P and the interface defect states occur.

By electrical detection of spin-echoes, measurement of the coherence times, T_2, as well as the longitudinal relaxation time, T_1, of interface defects and ^{31}P donor spins in proximity to them, was possible. These measurements revealed that $T_2 \approx 1.3$ μs for the P_b defect, independent of the applied temperature in the range $5\text{K} \leq T \leq 13\text{K}$. The T_2 time of ^{31}P donor electrons is slightly longer, and depends on the interface state density as described by De Sousa [8]. The longitudinal relaxation time T_1 is consistently longer then the T_2 times and depends strongly on the P_b density. The measured T_1 for both P_b and ^{31}P is the same, as expected for electrical readout using a spin-dependent electronic transition.

The observations contrast the pEPR measured T_1 and T_2 of bulk ^{31}P which are significantly longer and strongly temperature dependent. The implications of these findings for possible applications of the ^{31}P-interface defect transition as spin ^{31}P readout for proposed potential spin electronics or quantum information applications have been discussed.

3.5 References

[1] A. Gliesche, C. Michel, V. Rajevac, K. Lips, S. D. Baranovskii, F. Gebhard, and C. Boehme. *Physical Review B*, 77:245206, 2008.

[2] C. Boehme and K. Lips. *Physical Review B*, 68:245105, 2003.

[3] A. R. Stegner, C. Boehme, H. Huebl, M. Stutzmann, K. Lips, and M. S. Brandt. *Nature Physics*, 2:835, 2006.

[4] H. Huebl, F. Hoehne, B. Grolik, A. R. Stegner, M. Stutzmann, and M. S. Brandt. *Physical Review Letters*, 100:177602, 2008.

[5] A. Schweiger and G. Jeschke. *Principles of pulse electron paramagnetic resonance*. Oxford University Press, Oxford, UK ; New York, 2001.

[6] G. W. Morley, D. R. McCamey, H. A. Seipel, L. C. Brunel, J. van Tol, and C. Boehme. *Physical Review Letters*, 101:207602, 2008.

[7] A. M. Tyryshkin, S. A. Lyon, A. V. Astashkin, and A. M. Raitsimring. *Physical Review B*, 68:193207, 2003.

[8] R. de Sousa. *Physical Review B*, 76:245306, 2007.

[9] G. Lucovsky, Y. Wu, H. Niimi, V. Misra, and J. Phillips. *Applied Physics Letters*, 74:2005, 1999.

[10] A. Stesmans. *Physical Review B*, 48:2418, 1993.

[11] D. R. McCamey, H. Huebl, M. S. Brandt, W. D. Hutchison, J. C. McCallum, R. G. Clark, and A. R. Hamilton. *Applied Physics Letters*, 89:182115–3, 2006.

[12] R. N. Ghosh and R. H. Silsbee. *Physical Review B*, 46:12508, 1992.

[13] C. C. Lo, J. Bokor, T. Schenkel, A. M. Tyryshkin, and S. A. Lyon. *Applied Physics Letters*, 91:242106, 2007.

[14] L. H. Willems van Beveren, H. Huebl, D. R. McCamey, T. Duty, A. J. Ferguson, R. G. Clark, and M. S. Brandt. *Applied Physics Letters*, 93:072102, 2008.

[15] G. K. Lewis and W. L. Olbricht. *Review of Scientific Instruments*, 80:114704, 2009.

[16] M. Sarovar, K. C. Young, T. Schenkel, and K. B. Whaley. *Physical Review B*, 78:245302, 2008.

[17] R. de Sousa, eacute, rio, C. C. Lo, and J. Bokor. *Physical Review B*, 80:045320, 2009.

CHAPTER 4

ELECTRICALLY DETECTED CRYSTAL ORIENTATION DEPENDENT SPIN-RABI BEAT OSCILLATION OF *c*-Si(111)/SiO_2 INTERFACE STATES

The data presented in Chapters 1 to 3 have shown that next to the ^{31}P and the P_{b2} states, there is at least one additional paramagnetic center at the *c*-Si/SiO_2 interface which can influence recombination currents [1, 2], namely the E' state, a silicon dangling bond in the SiO_2 bulk [3]. However, it is not known from these experiments whether the E' center is involved in intermediate pair spin-processes [4] and whether ^{31}P and P_b could be the pair-partner, or whether it is due to other spin-dependent mechanisms which do not involve intermediate pairs [5]. Similarly, for the ^{31}P and P_b centers as well as the E' center, it is unknown if these states also allow transitions between identical centers [6].

4.1 Experimental details

In the following, experimental evidence is presented which shows that the beating of spin-resonantly driven Rabi-oscillation within pairs of paramagnetic *c*-Si/SiO_2 interface states can be detected electrically. As summarized in Appendix B, the beating is an unambiguous indicator for a pair identity: By bringing two spin-resonant states into a Rabi nutation at the same time, the spin-dependent rate will not reflect beating unless both spins are involved in the same transition [7]. This effect has recently been used to identify the nature of excitonic precursor pairs consisting of polaron states in an organic semiconductor [8]. Following the same experimental approach, pulsed electrically detected magnetic resonance experiments were con-

ducted on (111) oriented phosphorous doped ([^{31}P]= 10^{16} cm^{-3}), 300 μm thick, Cz-grown c-Si samples with a native oxide surface. The samples had lithographically structured contacts designed to not distort the microwave modes needed for magnetic resonant excitation [2]. All experiments discussed in the following were performed at a temperature of $T = 5$K, with optical injection of excess charge carriers by infrared filtered white light and under a bias of 3V. For the details of the sample preparation and the experimental conditions see Ref. [2]. For the coherent magnetic resonant excitation and the transient current detection, a Bruker E580 pulsed EPR facility with a low-Q cylindrical dielectric cavity was used.

4.2 Spin g factor distributions in the interface

Fig. 4.1 (a) illustrates a stick and ball model of the c-Si/SiO_2-interface and the paramagnetic states found thereat. The ^{31}P donor state is fully isotropic and slightly delocalized, while the P_b and the E' centers are both highly localized and anisotropic, with different main axis g-factors. At the (111) surface, the P_b center exists only in one orientation with the centers' main axis parallel to the (111) crystal axis. Thus, in spite of the anisotropy, all P_b states at the (111) surface have an identical g-factor. Figure 4.1 (b) shows the changes of an applied excess charge carrier current (optically induced as described in Ref. [2]) 20 μs after a short microwave pulse (length 320 ns, $f \approx 9.74$ GHz), as a function of the magnetic field. The spectrum reveals the expected magnetic resonances, the hyperfine coupled ^{31}P and the P_b resonance (for an angle of $\theta = 90^o$ between the (111) crystal axis and the B_0-field) [9] as well as the E' center [1, 2].

Note that in spite of a g-factor anisotropy of the E' state, its ensemble spectrum will always be isotropic due to the random orientation of the E' within the amorphous SiO_2 as well as bond-angle and bond-length distributions which lead to additional g-factor broadening. In contrast, the P_b state will shift throughout the spectrum as θ is changed. The blue arrow in Fig. 4.1 (b) represents the g-factor range accessible by choosing different orientation angles θ. Spectra for a range of different θ can be found in Ref. [2].

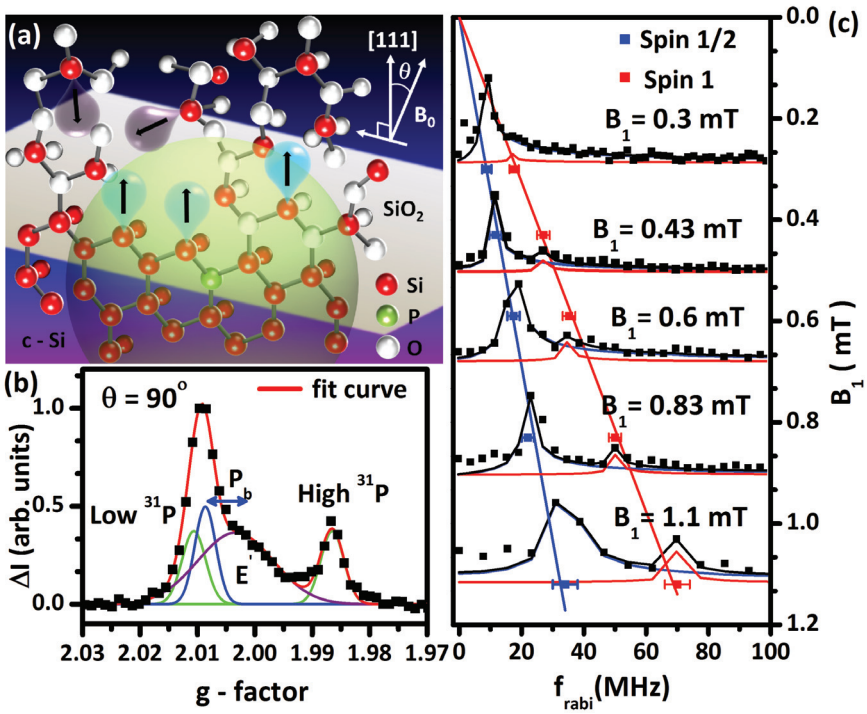

Figure 4.1: Atomic structure of the c-Si(111)/SiO_2 interface and the resultant spin-Rabi beat nutations. (a) Sketch of the atomic scale structure of the c-Si(111)/SiO_2 interface. The ^{31}P donor state (large green shaded circle) is significantly larger than the highly localized dangling bond defect states (blue balloons:P_b centers, purple balloons:E' centers). The orientation of the interface is defined by the angle between the externally applied B_0 magnetic field and the (111) crystal axis which is perpendicular to the crystal surface. (b) Electrically detected g-factor spectra of c-Si(111):P/SiO_2, measured at $\theta = 90°$ in temperature 5 K. Blue arrow represents that P_b resonance (blue line) shifts at different interface orientations. (c) Each linear plot represents B_1 field dependence of Rabi frequency of spin $\frac{1}{2}$(blue) and spin 1(red). Five plots of FFT (fast fourier transformation) of Rabi oscillation as a function of charge Q and Rabi frequency f_{Rabi}, which are measured with different B_1 field strengths. Solid curves in each plot are fit curves for spin $\frac{1}{2}$(blue) and spin 1 (red).

4.3 Electrically detected spin-Rabi beat effect

The detection of the spin-dependent current shown in Fig. 4.1 (b) allows us to scrutinize the previous experimental verification [10] that the ^{31}P-P$_b$ process involves weakly-coupled pairs of ^{31}P and P$_b$ states. For a crystal orientation of $\theta = 90°$, the P$_b$ peak has its maximal overlap with the low field ^{31}P peak. It is therefore possible to simultaneously induce Rabi nutation for both spin resonances. Figure 4.1 (c) displays plots of Fast Fourier transforms (FFT) of electrically detected spin-Rabi nutation measurements conducted at the resonance maximum of the spectrum displayed in Fig. 4.1 (b) (B_0 = 3463 G) for different B_1 values. The experiments were carried out as pulse length dependence measurements of a simple one-pulse experiment, as described before [8]. In the FFT data, two local frequency maxima can be fit with Fourier transformed integrated Bessel functions [11] (blue and red for the higher and lower frequency components, respectively). The results of these fits are plotted as a function of B_1 in Fig. 4.1 (c), together with fits of linear functions which reveal good agreement for proportionality factors of the gyromagnetic ratio γ (blue) and 2γ (red). The oscillation with frequency $\Omega = 2\gamma B_1$ gradually disappears as B_1 is reduced, showing that it is due to a beat oscillation [8, 12] of weakly coupled pairs, and not exchange coupled pairs (which lead to a B_1-independent $2\gamma B_1$ oscillation [13, 14]). Thus, the observed Rabi beat effect confirms the previous description of the ^{31}P-P$_b$ process as a pair of two weakly coupled spins s=1/2 [9, 10].

The electrically detected beating shown in Fig. 4.1 (c) is caused by weakly coupled $s = 1/2$ states whose spectral separation ΔB [1] is within the power broading interval of the excitation field ($\Delta B \leq B_1$) [7].

4.3.1 FFT of Rabi beat nutation data

Fig. 4.2 (a) displays the FFT of electrically detected Rabi nutation measured under similar conditions as the data in Fig. 4.1 (c) ($\theta = 90^o$, $B_1 \approx 0.54$ mT) as a function of the applied magnetic field B_0, expressed in Landé-(g)-factor units. The plot shows significant nutation at the two hyperfine split ^{31}P resonances, with the low

[1] The spectral separation is the difference $\Delta B = \Delta g \mu_B B_0$ between the on-resonance magnetic fields of the pair-partners. Here, Δg denotes the g-factor difference within the pair and μ_B the Bohr radius

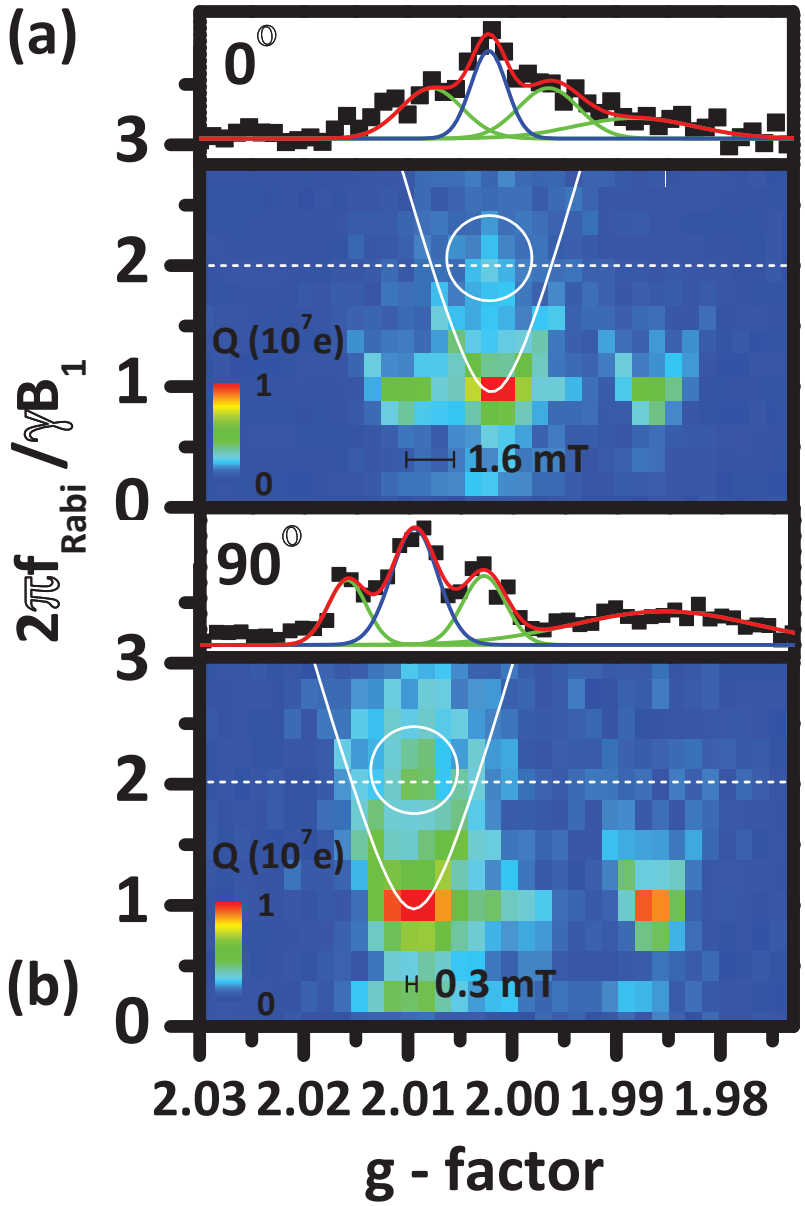

Figure 4.2: g-factor dependence of FFT of spin-Rabi oscillations measured at (a) 0° (upper) and (b) 90° (below) interface orientation. The plots present charge Q as a function of Rabi frequency (normalized by $\frac{2\pi}{\gamma B_1} f_{Rabi}$) and g-factors. Inset plots show the pEDMR spectra measured at each orientation (0° and 90°), in which one blue line, three green lines are Gaussian functions to fit data and the red line is resultant fit curve. 1.6 mT in (a) and 0.3mT in (b) represent Larmor separations between ^{31}P and P_b spins at 0° and at 90°.

field resonance appearing broader due to its overlap with the P_b resonance that has a nearly identical g-factor for the given θ. The $2\gamma B_1$-frequency components (white dashed line) of this data set are plotted in the inset as a function of g. They exhibit a symmetric feature with three maxima around $g \approx 2.01$ (corresponding to the low field ^{31}P and P_b resonances). The three maxima are fit by Gaussian distributions. Stegner et al. [9] previously showed that the two satellite peaks can be identified as the nutation signal of a detuned (=off-resonantly excited) spin using Rabi's frequency formula. [2] To confirm this, we note that the frequencies predicted by Rabi's frequency formula (see plot of white solid hyperbola in Fig. 4.2 (a)) overlap $\Omega = 2\gamma B_1$ at g-factors that coincide with the maxima of the two satellite peaks.

In contrast, the center peak occurs at the average g-factor of the low field ^{31}P and the P_b resonance. The inset of Fig. 4.2 (a) shows that while significant beating is detected close to the low field ^{31}P resonance, which nearly perfectly overlaps with the P_b center, only a very weak signal occurs around the high field ^{31}P resonance. This again is consistent with the ^{31}P-P_b model: For pairs involving ^{31}P with a nuclear spin that causes the high field donor spin resonance, the Larmor separation is close to the ^{31}P hyperfine splitting (≈ 42 G $\gg B_1$) and thus, beating is weak (it is discussed in Appendix B). Note, however, while the $2\gamma B_1$ signal is weak, it does not vanish entirely outside of the three large Gaussian features. Similar as for the off-center peaks close to the low field ^{31}P and the P_b resonances, these signals are not due to a beating effect as they can be verified to be due to the nutation of detuned spin $s = 1/2$ resonances.

To further scrutinize the beat effect shown in the inset of Fig. 4.2 (a), we repeated these measurements with a crystal surface perpendicular to the magnetic field ($\theta = 0$). Under these conditions, the P_b resonance has the largest separation from the low field ^{31}P and $\Delta B \approx 1.6$ mT $> B_1$. Hence, no beating due to the ^{31}P-P_b model is expected. The results of these measurements, shown in Fig. 4.2 (b), display for the on-resonance $s = 1/2$ nutation frequency $\Omega = \gamma B_1$ three well-separated peaks for the ^{31}P at $g \approx 2.01$ and $g \approx 1.986$ as well as P_b at $g \approx 2.002$ at $\theta = 0^o$. In contrast to Fig. 4.2 (a), no significant contributions are seen at both ^{31}P hyperfine lines for

[2] $\Omega = \sqrt{(\gamma B_1)^2 + (\omega - \omega_L)^2}$, ω denotes the excitation frequency, ω_L the Larmor frequency of the exited $s = 1/2$

$\Omega = 2\gamma B_1$. However, we observe (i) a significant beat component at the P_b resonance, as well as weaker contributions due to the off-resonant signals of all beat components. Since beating can only occur due to pairs with $\Delta B < B_1$, spin-dependent transitions involving P_b centers and other resonances with Landé-factors separated by less than B_1 must occur. These processes could involve transitions between adjacent P_b centers as previously seen under high magnetic fields [6] but also P_b to E' processes due to the overlap between the P_b and the broad E' resonance at $\theta = 0^o$ (see Fig. 4.1 (b)).

4.4 Orientation dependence of spin-Rabi beating

We have repeated the measurements shown in Fig. 4.2 (a) and (b) for 10 different crystal orientations for $0^o \leq \theta \leq 90^o$. Figure 4.3 (c) displays all of the FFT of the electrically detected Rabi nutation measurement recorded at g-factors where the $2\gamma B_1$ signal reached a maximum.

All examples (as all other measurements shown in the following) in Fig. 4.3 display a nutation signal that is much stronger than the beat signal. The reason for this is that the line widths of the all resonance peaks (see Fig. 4.1 (b)) are large compared to the applied $B_1 \approx 0.54$ mT. Thus, only for a small fraction of spin-pairs (referred to as "fraction of beating spins" or ξ_{beat} in the following [3]) can both pair partners be exited simultaneously. Because of the large magnitude of the nutation signal and the broad frequency distributions of both the nutation as well as the beat signal (they are Fourier transformed modified Bessel functions), a strong overlap of the beat signal and the nutation signal occurs at $2\gamma B_1$. Nevertheless, it is possible to deconvolute these superimposed frequency components with high accuracy (= small relative error on ξ_{beat}) by fitting the two distinct shapes of the superimposed frequency distributions.

The blue and red lines in Fig. 4.3 correspond to fit results for nutation and beat components, respectively. The results of these fits show that the beat component is maximal at crystal orientations close to $\theta \approx 20^o$ and $\theta = 90^o$ when the P_b center resonance overlaps with the maxima of the E' peak and the ^{31}P peak, respectively (see the blue arrow in Fig. 4.1 (b)). At $\theta \approx 43^o$, the g-value of the P_b center is out of

[3] As explained elsewhere [11], $\xi_{\text{beat}} = 2I_{\text{beat}}/(I_{\text{nut}} + 2I_{\text{beat}})$, with I_{nut} and I_{beat} being the currents of the nutation and the beat signal, respectively.

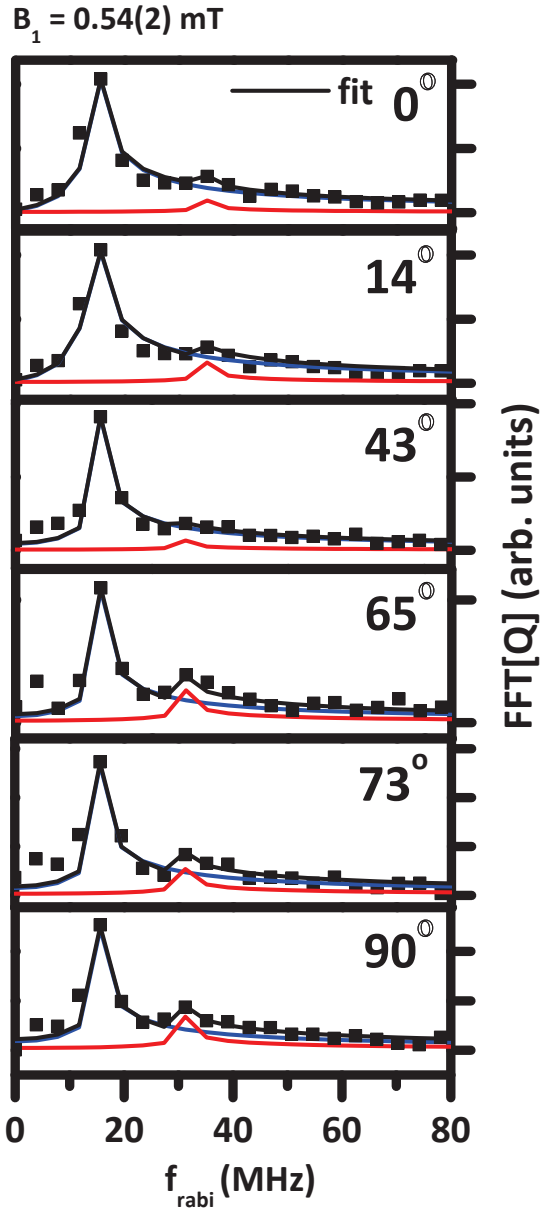

Figure 4.3: FFTs of spin-Rabi oscillations measured at different orientations (0°, 14°, 43°, 65°, 73° and 90°) with same B_1 field strength.(B_1= 0.54(2) mT) Each Rabi oscillation is measured on the B_0 field where the Rabi beating signal is maximized. The black solid lines demonstrate final fit curves while the blue and red lines represent fit curve for spin 1/2 Rabi nutation and for spin 1, beat nutation.

resonance with both peak maxima and thus, the beat oscillation reaches a minimum.

4.4.1 Predictions and pair transition models

Figure 4.4 displays plots of the g-factor where maximal beating was observed, while Fig. 4.5 shows the "fraction of beating spins" as functions of the crystal orientation (black data points). We compared these results with calculated predictions (following a procedure described in the supplementary information [15]) for these values based on two spin-dependent transition models, the ^{31}P-P$_b$ process (red) as well as the P$_b$-E' process (blue). The calculated values were based on the convolutions of the line-shapes and line-intensities of a pairs resonance partners as obtained from B_0 spectra similar to the one shown for $\theta = 90^o$ in Fig. 4.1 (b). Next to the calculated values, the panels of Fig. 4.4 also display the literature g-factors for ^{31}P, P$_b$ and E' (solid black lines). Figure 4.4(a) shows that when pairs of broadly distributed peaks (E') and narrow peaks (P$_b$) are formed, the beat signal follows the g-factor of the narrow peak. The main beat contribution from well-separated peaks of equally narrow peaks (like the P$_b$ and ^{31}P) appears somewhere between the two resonances, depending on the g-factor distributions of the pair partners.

4.4.2 Comparison and discussions

The comparison of the calculated values for the beating g-factor and ξ_{beat} with the beat experiment reveals that each of the two tested pair hypothesis is in agreement with the experimental data in a certain orientation range: At low angles ($0^o \leq \theta \leq 43^o$) the predictions for the ^{31}P-P$_b$ transition fits well with the experimental data, while at high angles($43^o \leq \theta \leq 90^o$), a match for the P$_b$-$E'$ pair transition is observed. Likewise, the measured ξ_{beat} agrees with calculated values for the two pair models for the same respective angular ranges. Even at $\theta \approx 43^o$, where the P$_b$ resonance is off-resonance with the E' and the low-field ^{31}P resonances, the beating does not vanish entirely. This is due to the large width of the E' resonance.

The data in Fig. 4.4 and Fig. 4.5 confirm the observation made from Fig. 4.3 that at different sample orientations, different processes dominate. Since the sum of beating currents for two tested models matches the experimental data, we conclude that spin-dependent processes other than P$_b$-E' and the ^{31}P-P$_b$ are not significant at the

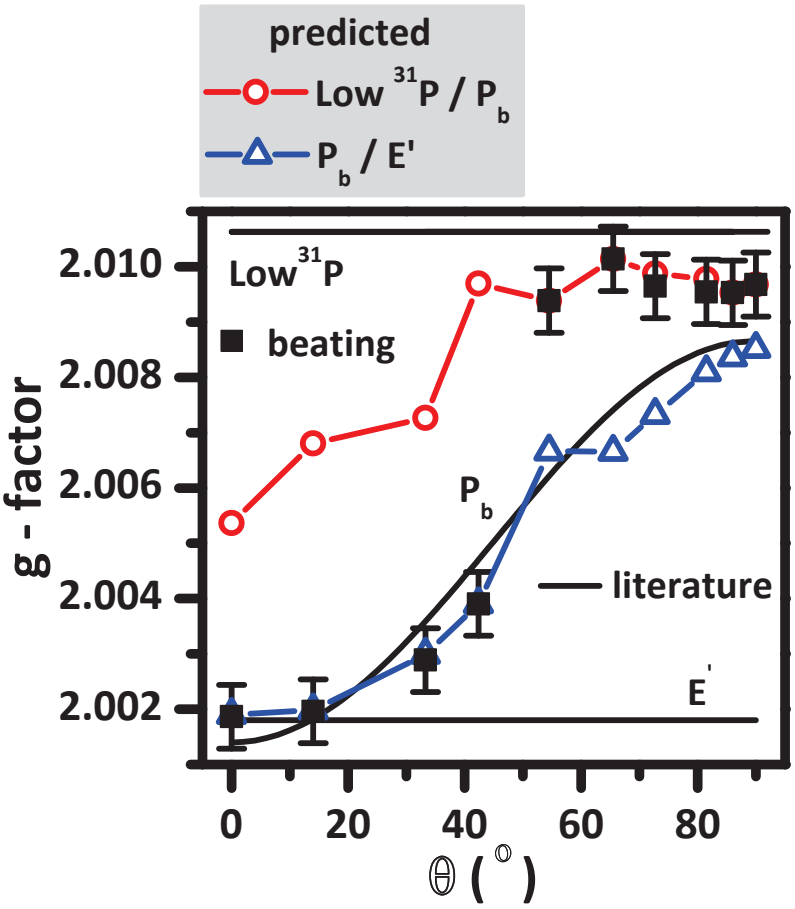

Figure 4.4: Black dots show measured g-factors of spin-Rabi beat oscillations as a function of interface orientations. Each solid line represents literature g-factors of ^{31}P, P$_b$ and E' defect, while red plot represents g-factors predicted based on the ^{31}P-P$_b$ spin-pair transitions and blue plot shows g-factor predictions of P$_b$-E' pair transitions.

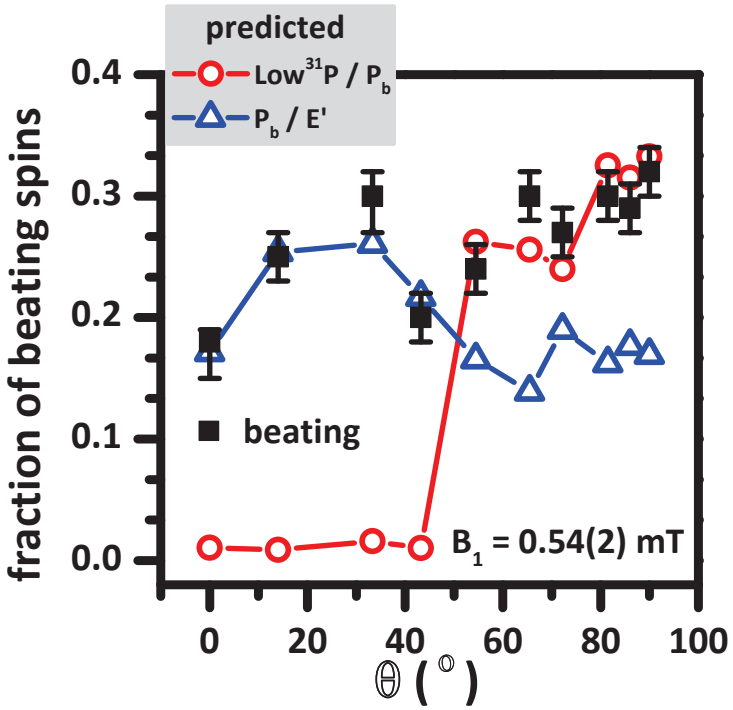

Figure 4.5: Fractions of beating spins in the excited spin-pairs. Black dots represent fraction of beating spin in the measured Rabi oscillation data at different orientations. Red plot shows the fraction of beating spins from the predicted spin-Rabi oscillation by ^{31}P-P$_b$ pair transitions, while blue plot shows the predictions of beating spin fraction by P$_b$-E' pair transitions and green plot represents the prediction of ^{31}P-E' spin-pair transitions in the interface.

c-Si(111)/SiO_2 interface. We speculate that the low field ^{31}P-E' process is negligible due to the small interaction probability of two bulk states from opposite sides of the interface (detailed discussion about low field ^{31}P-E' transition is in Appendix B). Transitions of the three centers with themselves could be weak because the ^{31}P concentration is not high enough for mutual interaction [15], while the overlap between adjacent P_b and adjacent E' states [6] may be weak due to the strong localization and the absence of percolation paths within the SiO_2 matrix. While this argument may be equally applicable to the low field P_b-E' process, it is clear from the experiments that this process does contribute significantly.

4.5 Conclusion

In conclusion, we report on the electrical detection of crystal orientation-dependent spin-Rabi beat oscillation of paramagnetic interface states at the c-Si(111)/SiO_2 interface. It has been demonstrated that using the well-known anisotropy of the P_b's g-factor, one can tune the Larmor separations within pairs of interface spins. Consequently, one can switch the spin-Rabi beat effect by means of B_0 field orientation. This tunable spin-beat effect could potentially be important for the selective manipulation of localized spin-states in silicon-based quantum information devices. Here, this effect is used for the experimental verification of the involvement of ^{31}P, P_b and E' states in different spin-dependent pair transitions. We identify the previously confirmed ^{31}P-P_b as well as the previously hypothesized P_b-E' interface recombination processes.

This material is based upon work supported by the NSF CAREER program under grant-♯0953225.

4.6 References

[1] C. Boehme and K. Lips. *Physica B: Condensed Matter*, 376-377:930–935, 2006.

[2] S. Y. Paik, S. Y. Lee, W. J. Baker, D. R. McCamey, and C. Boehme. *Physical Review B*, 81:075214, 2010.

[3] P. M. Lenahan and J. J. F. Conley. *Journal of Vacuum Science and Technology B*, 16:2134–2153, 1998.

[4] D. Kaplan, I. Solomon, and N. F. Mott. *J. Physique Lett.*, 39:51–54, 1978.

[5] D. J. Lepine. *Physical Review B*, 6:436, 1972.

[6] D. R. McCamey, G. W. Morley, H. A. Seipel, L. C. Brunel, J. van Tol, and C. Boehme. *Physical Review B*, 78:045303, 2008.

[7] C. Boehme and K. Lips. *Physical Review B*, 68:245105, 2003.

[8] D. R. McCamey, K. J. v. Schooten, W. J. Baker, S.-Y. Lee, S.-Y. Paik, J. M. Lupton, and C. Boehme. *Physical Review Letters*, 104:017601, 2010.

[9] A. R. Stegner, C. Boehme, H. Huebl, M. Stutzmann, K. Lips, and M. S. Brandt. *Nature Physics*, 2:835, 2006.

[10] F. Hoehne, H. Huebl, B. Galler, M. Stutzmann, and M. S. Brandt. *Physical Review Letters*, 104:046402, 2010.

[11] S.-Y. Lee, S.-Y. Paik, D. R. McCamey, J. Yu, P. L. Burn, J. M. Lupton, and C. Boehme. *Journal of the American Chemical Society*, 133:2019–2021, 2011.

[12] V. Rajevac, C. Boehme, C. Michel, A. Gliesche, K. Lips, S. D. Baranovskii, and P. Thomas. *Physical Review B*, 74:245206, 2006.

[13] A. Gliesche, C. Michel, V. Rajevac, K. Lips, S. D. Baranovskii, F. Gebhard, and C. Boehme. *Physical Review B*, 77:245206, 2008.

[14] S.-Y. Lee, S.-Y. Paik, D. R. McCamey, J. Hu, F. Zhu, A. Madan, and C. Boehme. *Applied Physics Letters*, 97:192104–3, 2010.

[15] G. Feher and E. A. Gere. *Physical Review*, 114:1245, 1959.

APPENDIX A

THEORETICAL AND TECHNICAL FOUNDATIONS OF PULSED EDMR EXPERIMENTS

The pulsed electrically detected magnetic resonance experiments discussed in Chapters 1 to 4 are based on the measurement of the transient changes of spin-dependent currents which are controlled by weakly coupled pairs of electron spins with $s = 1/2$. The nature of the different observed transitions follow the common behavior that before a spin-selective transition takes place, an exclusive intermediate pair is formed [1]. The intermediate pair formation is an important step which crucially determines the quantitative behavior of the transitions rates (relative rate change, dynamics after magnetic resonant manipulation of the involved spin states). This rate scheme of the intermediate pair model is sketched in Fig. A.1. It was first described by Kaplan, Solomon, and Mott in 1978 [2] and it has been successfully used since then for the accurate description of many spin-dependent recombination and transport processes in inorganic and organic semiconductors. Note, the rate picture displayed in Fig. A.1 does not contain densities of spin-pair eigenstates but simply densities for permutation symmetries, namely the singlet and triplet densities. Detailed descriptions of ensembles of spin states require the use of density matrices $\hat{\rho}$ (which for the case of a two spin $s = 1/2$ system contains 16 elements) [1]. The rate picture with two densities is nevertheless correct as long as it describes only the two permutation symmetry states of the fully dephased spin ensemble, so $n_S = \mathrm{Tr}\{\hat{\rho} \mid S\rangle\langle S \mid\}$ and $n_T = \sum_{i\in\{-,0,+\}} \mathrm{Tr}\{\hat{\rho} i \mid\rangle\langle i\mid\}$. Therefore, while the description given in Fig. A.1 is not suitable for the description of the transition rates during a short, coherent spin-resonant excitation of the spin ensemble, it is applicable to the dynamics of the transition rate after a short excitation pulse on a long, incoherence

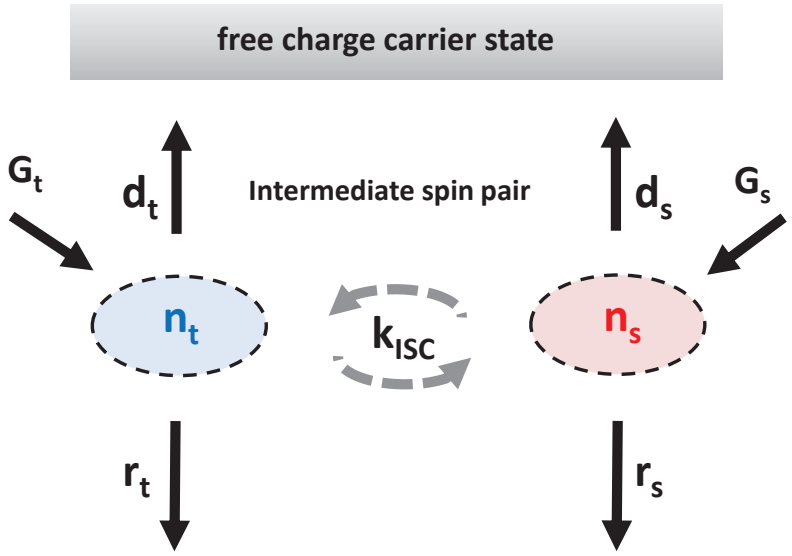

Figure A.1: Sketch of the intermediate pair recombination model by Kaplan, Soloman, and Mott (KSM). The sketch illustrates triplet or singlet densities among the spin-pair ensemble which are influenced by constant generation rates G_t and G_s, respectively, and two different pair annihilation processes, namely recombination with recombination probabilities r_t, r_s and pair dissociation into free charge carriers with probabilities d_t and d_s. [1, 2]. Interactions of spin-pairs with their environment can cause spin-relaxation, also called spin mixing or intersystem-crossing (ISC, with rate k_{ISC}).

time scale.

A.1 The transient behavior of spin-dependent currents controlled by spin $s = 1/2$ pairs after magnetic resonant excitation

The application of the rate model in Fig. A.1 shows that the conductivity change $\Delta\sigma$ measured by pEDMR depends on six parameters, the singlet and triplet recombination rate coefficients r_s, r_t, the pair dissociation coefficients d_s, d_t, the intersystem crossing rate k_{ISC}, and the fermi Dirac distribution between singlet and triplet states, which is given as

$$\rho = \frac{1}{1 + e^{\frac{\Delta E}{kT}}}. \tag{A.1}$$

ρ approaches zero at low temperature and 1/2 in the high temperature limit.
Following Fig. A.1, we see that the rate equations for singlet and triplet spin-pair densities are defined by the rate equations

$$\frac{dn_s}{dt} = G_s - C_s n_s + \alpha(n_t - n_s) - k_{ISC}(n_s - \rho n_s) + k_{ISC}(n_t - (1-\rho)n_t, \tag{A.2}$$

$$\frac{dn_t}{dt} = G_t - C_t n_t + \alpha(n_s - n_t) - k_{ISC}(n_t - (1-\rho)n_t) + k_{ISC}(n_s - \rho n_s), \tag{A.3}$$

where C_s and C_t are singlet and triplet pair annihilation rate coefficients, respectively, which consist of recombination and dissociation rates, $C_{s,t} = r_{s,t} + d_{s,t}$. The conductivity change $\Delta\sigma$ will then become

$$\Delta\sigma \propto d_s n_s + d_t n_t. \tag{A.4}$$

Exact solutions of the rate equations A.2, A.3 and the current transients after a magnetic resonant change of the spin-pair states can be found elsewhere [3, 4]; the conductivity change during a pulsed EDMR experiment becomes

$$\begin{aligned} \Delta\sigma &= \sigma - \sigma_0 = \mu e \tau (d_s n_s(t) + d_t n_t(t)) \\ &= \mu e \tau \left\{ \sigma_1 e^{-m_{12} t} + \sigma_2 e^{-m_{22} t} \right\}. \end{aligned} \tag{A.5}$$

with σ_0 being the steady state conductivity, μ, e, and τ are the mobility, the unit charge as well as the charge carrier lifetime, respectively, while

$$m_{12} = \frac{C_s + \omega_{12} + C_t + \omega_{22} - \sqrt{(C_s + \omega_{12} - C_t - \omega_{22})^2 + 4\omega_{12}\omega_{22}}}{2}, \quad \text{(A.6)}$$

$$m_{22} = \frac{C_s + \omega_{12} + C_t + \omega_{22} + \sqrt{(C_s + \omega_{12} - C_t - \omega_{22})^2 + 4\omega_{12}\omega_{22}}}{2} \quad \text{(A.7)}$$

and

$$\sigma_1 = \Delta n k_1, \quad \text{(A.8)}$$

$$\sigma_2 = \Delta n k_2 \quad \text{(A.9)}$$

represent the time constants and prefactors of the two exponential decay functions which determine the biexponential relaxation of the conductivity change back towards the steady state after the spin excitation has taken place. Note that

$$\omega_{12} = k_{ISC}(1 - \rho), \quad \text{(A.10)}$$

$$\omega_{22} = k_{ISC} \cdot \rho, \quad \text{(A.11)}$$

$$\text{(A.12)}$$

and

$$\begin{aligned} k_1 &= \mu e \tau \cdot \left\{ \frac{-d_s(m_{12} - C_t)}{m_{22} - m_{12}} + \frac{d_t(m_{12} - C_s)}{m_{22} - m_{12}} \right\}, \\ k_2 &= \mu e \tau \cdot \left\{ d_s(1 + \frac{m_{12} - C_t}{m_{22} - m_{12}}) - d_t(1 + \frac{m_{12} - C_s}{m_{22} - m_{12}}) \right\}. \end{aligned} \quad \text{(A.13)}$$

The biexponential decay function is nicely reproduced by the experimentally measured conductivity transient as displayed in Chapter 1. Note that these results for pulsed EDMR transients are equally applicable to pulsed optically detected magnetic resonance experiments when spin-dependent intermediate pair processes control optical emission, for instance, via radiative recombination. The transient photoluminescence (PL) rate after a brief magnetic resonant spin excitation will follow a similar biexponential relaxation transient

$$\begin{aligned} \Delta PL &= I(t) - I_0 = r_s n_s(t) + r_t n_t(t) \\ &= I_1 e^{-m_{12}t} + I_2 e^{-m_{22}t}. \end{aligned} \quad \text{(A.14)}$$

A.2 pEODMR experimental setup

For the experiments presented above, an experimental setup was needed which allowed a fast, reliable, and reproducible execution of pEDMR experiments. For the magntic resonant excitation, a pulsed electron spin resonance spectrometer (Bruker Elexsys E580) was employed together with a cylindrical, dielectric, low-Q (for sharp pulses) pulse microwave resonator. The resonator allowed the generation of homogeneous, up to approx. 1mT strong microwave pulses, as short as 4ns and with rise times in the sub ns-range. As this setup was designed for electron spin resonance spectroscopy, the commercially available equipment did not facilitate pEDMR or pODMR measurements. Part of the work presented here was therefore the development of a pEDMR/pODMR probehead that allowed us to conduct simultaneously both EDMR (electrically detected magnetic resonance) and ODMR (optically detected magnetic resonance) measurements. The sketch in Fig. A.2 (a) displays this probehead which is equipped with a fiber bundle for optical excitation of the sample and the detection of photoluminescence. As shown in Fig. A.2 (c), the fiber bundle consists of an excitation fiber (diameter is 100 μm) in the center, and four detection fibers (400 μm diameter) around the excitation fiber. The total diameter of the fiber bundle inside the resonator is less than 1 mm, and the fiber is fixed by a thin channel in a custom made printed circuit board (PCB) extension above the sample. Outside the resonator, the excitation fiber is attached to an SMA connector so that a light source can easily by coupled into the fiber. Likewise, the four detection fibers are tied up in an SMA connector that can be coupled to an optical detector. The entire fiber bundle is coupled to the pEDMR/pODMR sample surface via a thin mirror attached which is located at the end of the PCB extension (see Fig. A.2 (d),(e)). This mirror reflects the incident light into a direction perpendicular to the sample surface, and similarly, the optical signal from the sample is directed into the detection fibers.

A.3 Design of PCBs within the EODMR sample holder

The purpose of the PCBs in the probehead shown in Fig. A.2 (b) is to establish electrical contact between the electrodes of the sample and the electronic setup. Figure A.3 shows the composition of the PCBs and how metal pads on the PCBs

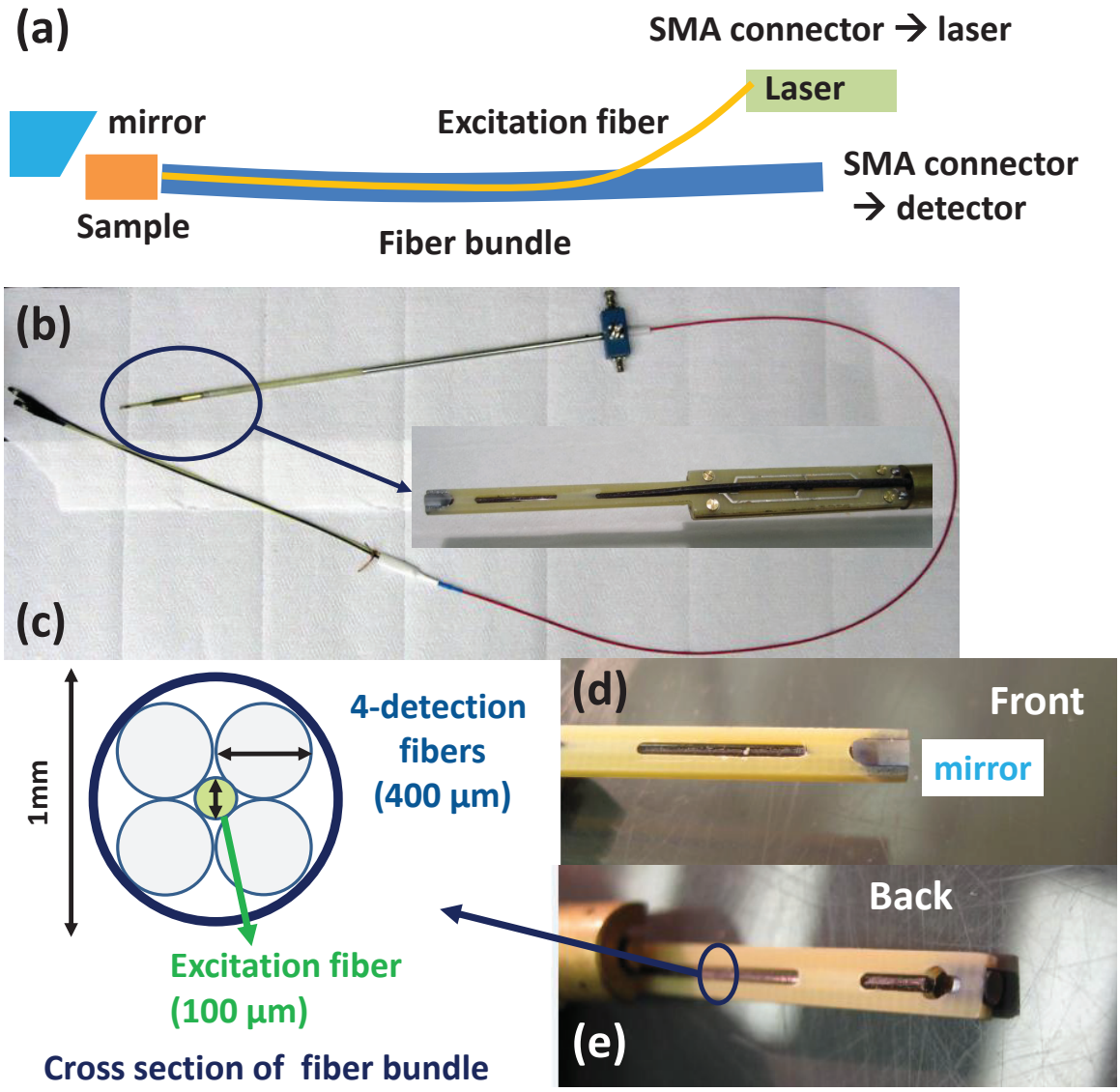

Figure A.2: The experimental setup for pEDMR and pODMR experiments. (a) Schematic diagram of the optical setup. (b) Fiber bundle and the PCB sample holder with mirror. (c) Cross-sectional diagram of fiber bundle. (d), (e) Fiber bundle as aligned in the channel of the PCB.

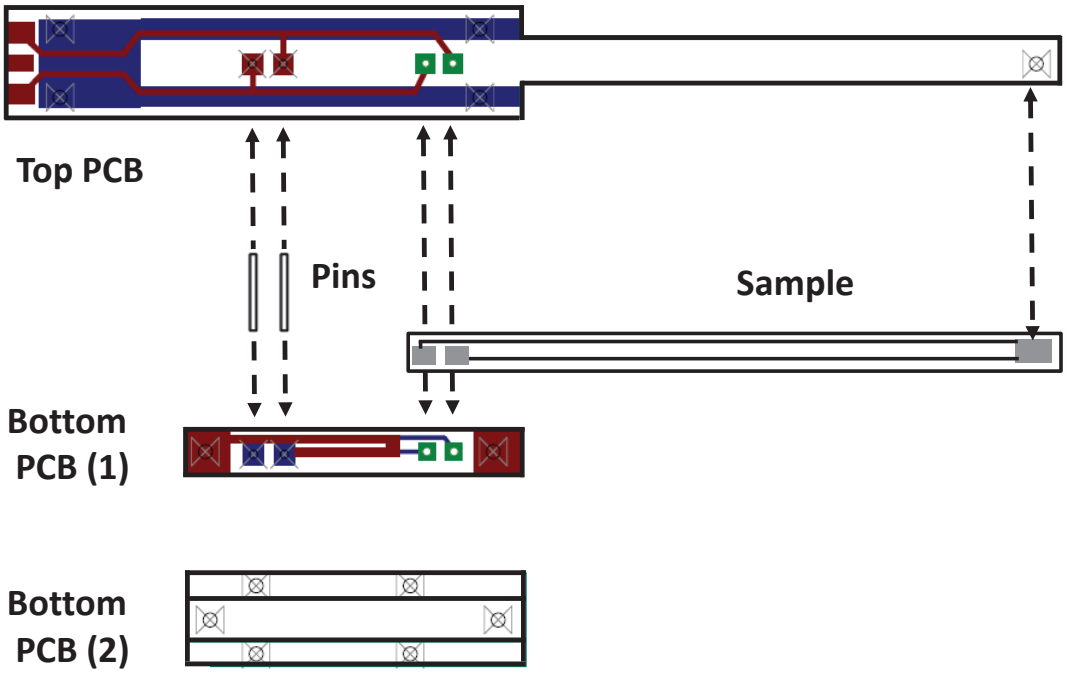

Figure A.3: PCB design for pEDMR and pODMR experiments. The PCB of pE-ODMR probehead consists of three different PCB layers which are called top PCB, bottom PCB (1) and bottom PCB (2). For pEDMR or pODMR experiments, the sample is placed between the top PCB and the bottom PCB (1). The top PCB has an extension with a small mirror (on the right side in the figure) to attach an optical fiber bundle. Two pairs of metal pads and thin silver wires for electric circuit combination are located on the surfaces of the top and bottom PCBs. The bottom PCB (2) is made to support the sample and the other PCBs. It is connected by four screws to the brass holder of the probehead.

are connected to the electrodes of the sample.

The PCB part consists of three small PCBs, which are called Top PCB, bottom PCB (1), and bottom PCB (2). In order to attach all the PCBs and the sample to the brass holder, the bottom PCB (2) is placed beneath the bottom PCB (1) and fixed by small screws on the tuning fork-shaped brass part (see Fig. A.4 (a)). On the extended part of the top PCB, we made a narrow (1 mm) channel to fix the optical fiber bundle on the sample surface, and a mirror is attached on the 2 mm diameter hole at the end of Top PCB extension. Since the mirror is thin aluminum coating that is significantly thinner than the microwave penetration depth, the B_1 microwave field is nearly undistorted by the mirror.

Figure A.4 shows how the PCBs of the pEDMR/pODMR probehead are assembled with the tuning fork shaped brass part and the fiber bundle of the sample holder: (a) Fix the bottom PCB (2) on the brass part with four screws. (b) Place the bottom PCB (1) in the channel of brass part. (c) Put a proper spacer (whose geometry depends on the sample thickness) on the bottom PCB (1). (d) Stick two pins into the metal pads of the bottom PCB (1). (e) Put a second spacer to fix the sample position in right and left. (f) Plug the completed PCB-brass part sample holder to the brass part of sample rod, and fix them with screws. (g) Place the sample and the top PCB on the bottom PCB (1), and fix the top PCB onto the brass part with four screws. Insert the fiber bundle through the channel on the top PCB until the tip of fiber bundle reaches at the top of the sample.

Figure A.4: Assembling procedure of EODMR sample holder, which is combined with three kinds of PCBs and a tuning fork shaped brass part. For details see text.

A.4 References

[1] C. Boehme and K. Lips, Phys. Rev. B 68, 245105 (2003)

[2] D. Kaplan, I. Solomon, and N. F. Mott, J. Phys. Lett. (Paris) 39, L51 (1978)

[3] D. R. McCamey, S.-Y. Lee, S.-Y. Paik, J. M. Lupton, and C. Boehme Phys. Rev. B 82, 125206 (2010)

[4] S.-Y. Lee, pulsed electrically and optically detected magnetic resonance spectroscopy of disordered semiconductors. PhD thesis, Department of Physics and Astronomy, The University of Utah. (2011)

APPENDIX B

ELECTRICAL DETECTION OF SPIN-RABI BEATING

Spin-dependent electronic transition rates which are governed by the permutation symmetry of pairs consisting of two paramagnetic states with spin $s = 1/2$ (intermediate pairs [12]) can reflect a resonantly driven coherent oscillation (Rabi nutation) of these spin states [15]. Electronic transitions are more likely for spin-pair states in the singlet state $|S\rangle$ compared to triplet states, and the transition rate is therefore proportional to $|\langle S|\Psi\rangle|^2$, where $|\psi\rangle$ is some arbitrary state of the spin-pair [15, 18]. This effect allows the observation of spin-Rabi nutation by electrical current measurements as illustrated for the example of spin-dependent c-Si/SiO_2 interface processes in Fig. B.1 (a), (c), and (e).

Figure B.1 (a) displays the spectrum of paramagnetic interface centers along with the excitation spectrum of a short excitation pulse whose frequency and field strength (B_1) have been chosen such that paramagnetic centers within the grey shaded Lorentzian area are excited. The width of this grey Lorentzian shaped area is proportional to B_1 [15]. As shown in Fig. B.1 (a), the grey area has a significant overlap with the ^{31}P low field resonance (green Gaussian line), but it has only little overlap with the P_b resonance (blue Gaussian line). Therefore, in most weakly coupled $^{31}P/P_b$ pairs, the spin of one of the two pair partners (the ^{31}P) undergoes a Rabi nutation while the spin of the other pair partner (the P_b) remains unchanged and consequently, the permutation symmetry of the spin-pair oscillates with the Rabi nutation frequency of the spin in resonance (γB_1 with γ = gyromagnetic ratio).

When B_1 is increased, the electron spin resonant excitation range of the spin-manipulation pulse increases proportionally. For sufficiently strong B_1, both pair partners are excited by the pulse simultaneously. This is illustrated by the grey Lorentzian shaped area in Fig. B.1 (b), (d). Here, the grey area is much wider and

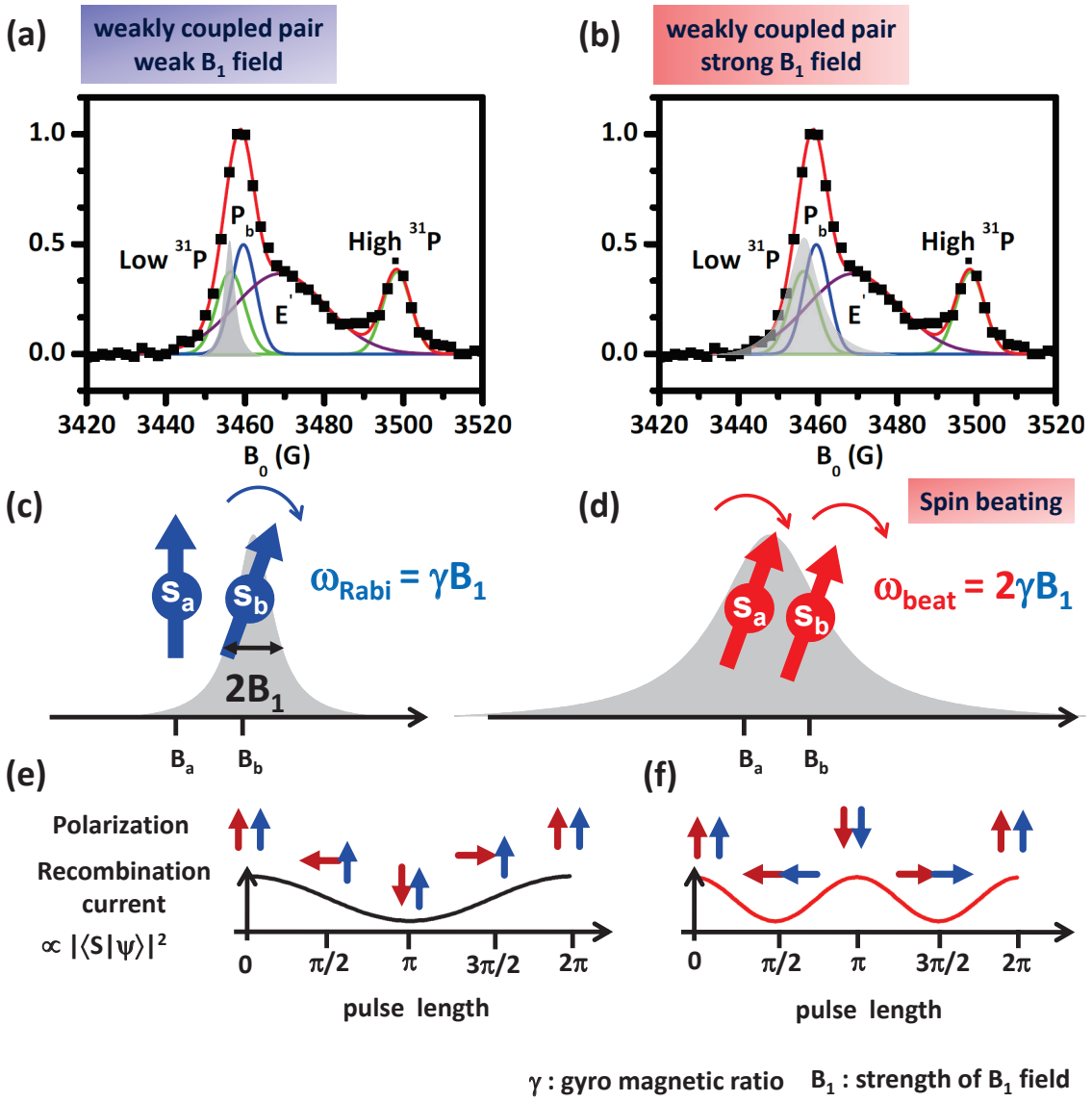

Figure B.1: Rabi-beat nutation (a) B_0 field spectrum of c-Si(111)/SiO_2 interface. Grey colored Lorentzian line represent excitation B_1 field. The weak B_1 field excites small portion of spins inside the line area. (b) Strong B_1 field excitation. (c) Conceptual sketch of spin-Rabi nutation for the weakly coupled spin-pair. With weak B_1 field excitation, only a spin in the pair nutates with Rabi frequency. (d) Both spins in the pair are excited at the same time by the strong B_1 field (spin beating). (e) Evolution of spin orientations during B_1 pulse excitation and electrically measured recombination current for the weak B_1 field and (f) for the strong B_1 field.

both the ^{31}P and the P_b resonances are excited at the same time, and both spins nutate. Due to the weak coupling nature of the pairs, spin states corresponding to the $|\rightarrow\rightarrow\rangle$ and the $|\leftarrow\leftarrow\rangle$ states (which are noneigenstates) have a higher transition probability than the $|\uparrow\uparrow\rangle$ and $|\downarrow\downarrow\rangle$ states [15, 16, 18]. Consequently, the spin-dependent rate now oscillates with twice the frequency (i.e. $2\gamma B_1$). This illustrates the nature of the beat effect [16]. Electrically detected spin-beating can occur when linked to intermediate pair processes; its observation is therefore proof of the presence of intermediate pairs. Note that the beat frequency $2\gamma B_1$ can be observed not only due to beating of weakly coupled pairs but also from pairs with significant exchange interaction [19]. However, this effect is independent of B_1 and, therefore, an increasing beating component with increasing B_1 is proof for beating due to spin-dependent electronic transitions between weakly spin-spin coupled intermediate pairs of paramagnetic centers with $s = 1/2$.

B.1 Deriving a prediction of the spin-Rabi beat signal strength from EDMR line spectra

The number of beating spin-pairs is strongly dependent on the strength of B_1 as well as the spectral separation of the paramagnetic states within the intermediate pairs. Thus, the magnitude of the observed beating currents and charges [1] depend on these parameters, too [16, 17]. Thus, when the magnetic resonance spectra of paramagnetic states involved in spin-dependent transitions are known, predictions for the beat current can be obtained for any hypothesized pair scenario. A confirmation of this pair hypothesis can then be obtained by comparison of the calculated beat signals and experimentally observed beat signals.

For the electrically detected magnetic resonance (EDMR) spectrum in Fig. B.1, all resonances are inhomogeneously broadened and their g-factor distributions can be described by Gaussian functions

$$G_i = A_i exp\left(-\frac{(B_0 - c_i)^2}{2 \cdot w_i^2}\right) \tag{B.1}$$

where $i = P_b$, E', the low field ^{31}P, or the high field ^{31}P. The variables c_i represent the distribution centers, w_i the widths of the Gaussian functions, and A_i the magnitude

[1] For EDMR experiments, transient spin-dependent currents are usually integrated into charges [4]

of the Gaussian distribution that corresponds to the number of paramagnetic centers $N_i = \sqrt{2\pi} w_i A_i$ that are involved in spin-dependent processes. When the excitation distribution is dominated by power broadening, the excitation probability can be described by a Lorentzian function

$$L = \frac{B_1^2}{(B_0 - B_c)^2 + B_1^2} \tag{B.2}$$

where the peak center $B_c = \frac{h\nu}{\mu_B g}$ is defined by the pulse frequency ν (μ_B is Bohr's magneton and h Planck's constant). For each resonance line, the expectation value of the number n_i of spins excited by the given B_1 field is therefore,

$$n_i = \int_{-\infty}^{+\infty} L \cdot G_i dB_0. \tag{B.3}$$

For a given microwave pulse (defined by B_1 and B_c)), the fraction P_i of excited spins of the type i can therefore be obtained by

$$P_i = \frac{n_i}{N_i} = \frac{n_i}{\sqrt{2\pi} \cdot A_i \cdot w_i} \tag{B.4}$$

while the probability to observe a beat signal from pairs consisting of spins types i and j is

$$P_{beat} = P_i \cdot P_j. \tag{B.5}$$

For spin-Rabi beating to occur, two spins i and j must be excited simultaneously. Note that the resonance peak areas of spin species belonging to pairs are identical in EDMR spectra [15] unless at least one of the pair partners are also involved in other spin-dependent processes. For any given spin-dependent pair process, the number of spin-pairs involved is therefore limited by the spin species with the smallest integrated peak area. Since the current measured in an EDMR experiment is proportional to the number of electronic transitions, and this number corresponds to the number of intermediate pairs which decay, the amplitude of the Rabi beating signal Q_{beat} is

$$Q_{\text{beat}} = e \cdot \frac{P_i \cdot P_j (2 \cdot n_i)}{2} = e P_i P_j n_i \tag{B.6}$$

where $i \neq j$, and $n_i \leq n_j$ without confinement of generality (e is the electron charge). The factor 1/2 comes from the fact that beating signals require twice as many spins for the same signal intensity as a spin-1/2 nutation signal [15, 18].

We can calculate the EDMR nutation signal (the γB_1 component) in presence of a beat signal involving spins species i and j by

$$Q_{\text{nut}} = e\sum_i n_i - 2Q_{\text{beat}} \tag{B.7}$$

$$= e\left(\sum_{i\neq j} n_i + n_j\{1 - 2P_i \cdot P_j\}\right) \tag{B.8}$$

where we simply count all spins which are excited and subtract those pairs which contribute to the beating signal (note that numbers of spin species are subtracted here, not numbers of charge carrier. This is the reason for the factor 2).

The four spin resonances found to involve spin-dependent transitions around the c-Si(111)/SiO_2 interface allow for six combinations of possible spin-pair transitions (between nonidentical paramagnetic centers). Using the lineshape parameters obtained from EDMR spectra, we derived predictions for the beat signal intensities (the "fraction of spin-pairs") and the beat signal g-factors. As the high field ^{31}P is well-separated spectrally from the other defects (which therefore does not allow for beating), we compared the results of these calculations only for the low field ^{31}P-P$_b$, the low field ^{31}P-E' and the P$_b$-E' hypothesis. Among these three models, the predictions based on the low field ^{31}P-P$_b$ transition and the P$_b$-E' transition matched well with the measured results. Since low field ^{31}P and E$'$ are separated by a θ-independent magnetic field, a θ-independent beating offset due the low field - P$_b$-E' hypothesis is expected for magnetic fields between the two resonances. This predicted low field ^{31}P-E' beating signal is not consistent with the measured data at any orientation. Thus, ^{31}P-P$_b$ and P$_b$-E' pair transitions appear to be the only dominant spin-dependent transitions occuring at the interface.

B.2 Proof that the observed spin-Rabi beat oscillation is due to weakly couple spin-pairs

The interpretations of the experimental data discussed in this study have been based on the assumption that the observed pairs of electronic spins states are mutually weakly coupled. "Weak" in this regard is defined as a spin-coupling strength (e.g. exchange of magnetic dipolar coupling) between two paramagnetic states whose

magnitude is below the Larmor separation (= difference between the Zeeman energies of the two spins). Weak coupling is not a requirement for the existence of spin-Rabi beat oscillation, in fact it has been shown [19] that strongly exchange coupled pairs also produce an electrically detectable beat signal and thus, the observation of beating cannot exclude the possibility that one of the main assumptions for the data interpretation is wrong.

Gliesche et al. [19] have shown that in presence of strong exchange, the observed beat signal becomes independent from the driving field strength B_1. This is in contrast to the weakly coupled case where the beat signal intensity monotonically increases with B_1. Thus, for the verification of the weak coupling regimes, we measured the magnitude of the spin-beating signal as a function of B_1.

In Fig. B.2, blue and red dots represent the fraction of spin-pairs which do not exhibit beating but solely a spin $s = 1/2$ Rabi nutation (blue dots) and the fraction of spin-pairs which does exhibit spin-Rabi beat oscillation (red dots). The relative magnitudes are obtained from the fit results of the measured Rabi nutation transients (See Fig. 4.3). As we explained in Chapter 4, the fraction beating pairs is increased with B_1. One can see in Figure B.2, the fraction of beating spin-pairs is exceedingly small ($\sim$ 10%) in the weak excitation regime $B_1 \approx 0.3$ mT. For larger B_1, it is increased and reaches a maximum at ($\sim$ 40%) at $B_1 = 1.1$ mT. This is clear evidence that the spin-dependent processes at the c-Si/SiO_2 interface are weakly coupled.

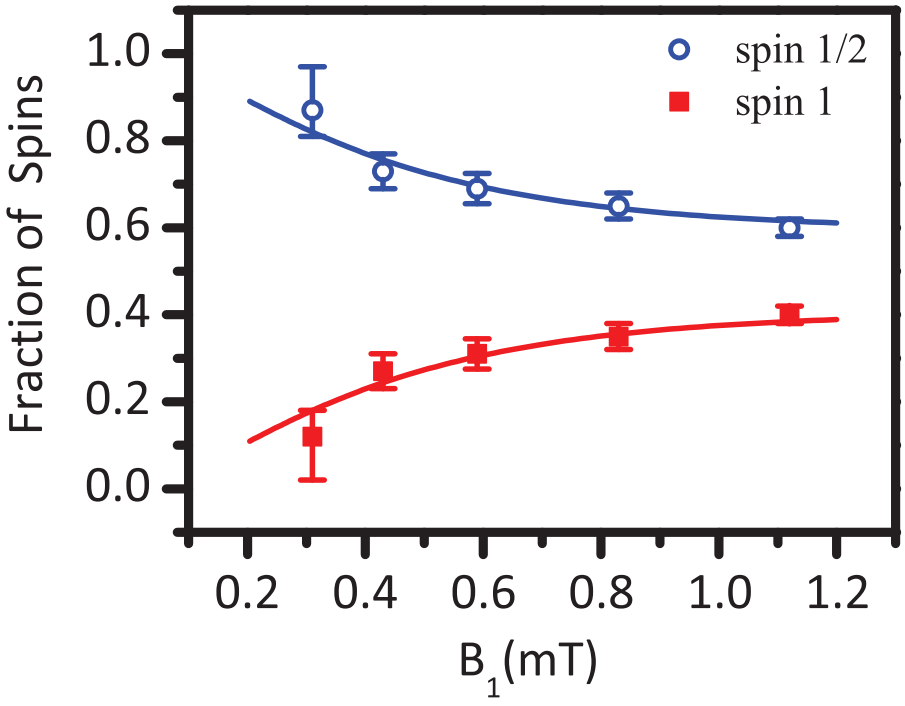

Figure B.2: Plot of the fraction of spin-pairs exhibiting spin-Rabi beating as a function of B_1. The blue dots represent the fractions of pairs which do not exhibit beating, the red dots represent the fractions of spin-pairs which do exhibit beating. The blue and red solid lines show the predicted values for the respective spin-pair fractions based on the g-factor distributions.

B.3 References

[1] F. Hoehne, L. Dreher, H. Huebl, M. Stutzmann, and M. S. Brandt, Phys. Rev. Lett. 106,187601 (2011).

[2] J. J. L. Morton, A. M. Tyryshkin, R. M. Brown, S. Shankar, B. W. Lovett, A. Ardavan,T. Schenkel, E. E. Haller, J. W. Ager, and S. A. Lyon, Nature 455, 1085 (2008).

[3] C. Boehme and K. Lips, Phys. Status Solidi B 233, 427 (2002).

[4] A. R. Stegner, Nature Phys. 2, 835 (2006).

[5] D. R. McCamey, Appl. Phys. Lett. 89, 182115 (2006).

[6] H. Morishita, L. S. Vlasenko, H. Tanaka, K. Semba, K. Sawano, Y. Shiraki, M. Eto, and K. M. Itoh, Phys. Rev. B 80, 205206 (2009).

[7] F. Hoehne, H. Huebl, B. Galler, M. Stutzmann, and M. S. Brandt, Phys. Rev. Lett. 104, 046402 (2010).

[8] S.-Y. Paik, S.-Y. Lee, W. J. Baker, D. R. McCamey, and C. Boehme, Phys. Rev. B 81, 075214 (2010).

[9] H. Huebl, F. Hoehne, B. Grolik, A. R. Stegner, M. Stutzmann, and M. S. Brandt, Phys. Rev. Lett. 100, 177602 (2008).

[10] C. Boehme and K. Lips, Physica B 376, 930 (2006).

[11] P. M. Lenahan et al., J.Vac.Sci.Technol.B 16, 2134 (1998)

[12] D. Kaplan, I. Solomon, and N. F. Mott, J. Phys. Lett. (Paris) 39, L51 (1978)

[13] D. J. Lepine, Phys. Rev. B 6, 436 (1972).

[14] D. R. McCamey, G. W. Morley, H. A. Seipel, L. C. Brunel, J. van Tol, and C. Boehme, Phys. Rev. B 78, 045303 (2008).

[15] C. Boehme and K. Lips, Phys. Rev. B 68,, 245105 (2003).

[16] D. R. McCamey, K. J. van Schooten, W. J. Baker, S.-Y. Lee, S.-Y. Paik, J. M. Lupton, and C. Boehme, Phys. Rev. Lett. 104, 017601 (2010).

[17] S.-Y. Lee, S.-Y. Paik, D. R. McCamey, J. Yu, P. L. Burn, J. M. Lupton, and C. Boehme, Journal of the American Chemical Society 133, 2019 (2011).

[18] V. Rajevac et al., Phys. Rev. B 74, 245206 (2006)

[19] A. Gliesche, C. Michel, V. Rajevac, K. Lips, S. Baranovskii, F. Gebhard, and C. Boehme, Phys. Rev. B 77, 245206 (2008).

[20] S.-Y. Lee, S.-Y. Paik, D. R. McCamey, J. Hu, F. Zhu, A. Madan, and C. Boehme, Applied Physics Letters 97, 192104 (2010).

[21] G. Feher, Phys. Rev. 114, 1219 (1959).

APPENDIX C

FIT PROCEDURE FOR LIGHTLY CONVOLUTED PEDMR SPECTRA

In order to interpret the frequency components of the Fast Fourier transformed (FFT) Rabi nutation data, we compared the experimental results with predictions of various pair processes which were based on the g-factor distributions assigned to the pair-partners of the tested hypothesis. These g-factor distributions were obtained from B_0 field dependence EDMR spectroscopy measurements (see Chapter 1). Since the Larmor separations (the differences of Larmor frequencies within given spin-pairs) influence the magnitude of a given beating signal, and since these Larmor separations depend strongly on the properties of the resonance peaks associated with a pair (intensity, width, center), EDMR signals can be used to predict the strength of Rabi beat nutation for a given pair hypothesis. Therefore, before conducting electrically detected spin-beat experiments, we performed the B_0 field dependence EDMR spectroscopy measurements in order to obtain the g-factor distributions of the paramagnetic centers which could potentially be involved in the observed beating signal. Spin-beat experiments were conducted using comparatively low B_1 fields ($B_1 \approx 0.3$mT, pulse length = 320ns), in order to minimize power broadening effects.

C.1 PEDMR measurements as a function of the crystal orientation

A self built goniometer attached to the sample rod outside the microwave resonator was used to adjust angles between the sample surface and the B_0 field. As the absolute sample orientation angle was difficult to determine from the sample rod orientation due to occasional random misalignment of the sample with regard to the outer sample rod (this could occur after the sample was introduced into the cryostat/resonator

setup and produce random misalignment of up to 30°), we determined the absolute angles by comparison with fit results of P_b B_0 field spectrum. The angular accuracy of this procedure was $< 0.5°$.

In Figure C.1, fit results of spectra measured at different sample orientations are shown. Note that the g-factors of E' centers (purple dots) are distributed in the range of $2.0004 \sim 2.003$. The predicted g-factors for maximized spin-beat signals are shown in Figure A.1. The red circles, blue triangles, and green diamonds represent predictions for low field ^{31}P-P_b, P_b-E' and low field ^{31}P-E' pair transitions, respectively. As discussed in Chapter 4, we confirmed that the sample surface orientation determined which spin-pair transition contributed dominantly to the observed spin-Rabi beat signal. By comparing the calculated values with the measured beat signals we see that at low orientation angles, the P_b-E' pair transition produces the strongest beating signal, while the low field ^{31}P-P_b pair transition becomes most dominant for beating at higher sample orientation angles.

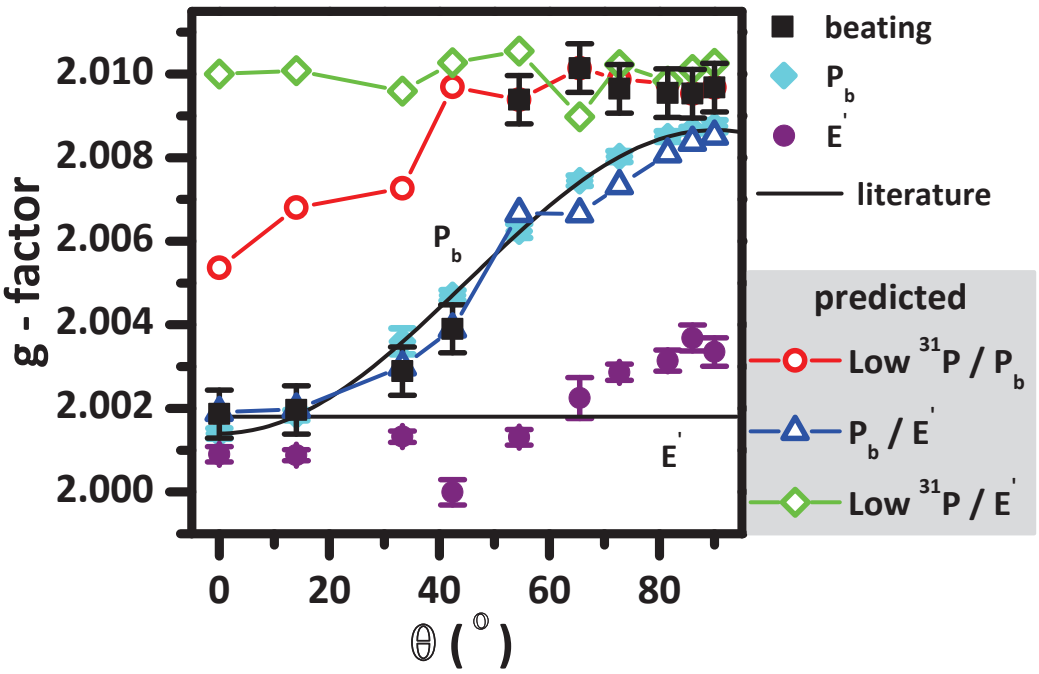

Figure C.1: Black dots display measured g-factors where a maximal spin-Rabi beat oscillation is observed, as a function of the interface orientation. Each solid line represents literature g-factors of ^{31}P, P_b and E' defect, respectively. The red plot represents g-factors predicted by the ^{31}P-P_b transition, the blue plot represents g-factors predicted by the P_b-E' transition.

LIST OF PUBLICATIONS

Publications first-authored by the author

Electrically detected crystal orientation dependent spin-Rabi beat oscillation of *c*-Si(111)/SiO_2 interface states
S.-Y. Paik, S.-Y. Lee, D. R. McCamey, and C. Boehme
submitted for publication (2011).

T_1- and T_2-spin relaxation time limitations of phosphorous donor electrons near crystalline silicon to silicon dioxide interface defects
S.-Y. Paik, S.-Y. Lee, W. J. Baker, D. R. McCamey, and C. Boehme
Phys. Rev. B **81**, 075214 (2010).

Publications co-authored by the author

Tuning hyperfine fields in conjugated polymers for coherent organic spintronics
S.-Y. Lee, S.-Y. Paik, D. R. McCamey, J. Yu, P. L. Burn, J. M. Lupton and C. Boehme
J. Am. Chem. Soc. **133**, 072019 (2011).

Spin-dependent processes in amorphous silicon-rich silicon-nitride
S.-Y. Lee, S.-Y. Paik, D. R. McCamey, J. Hu, F. Zhu, A. Madan, and C. Boehme
Appl. Phys. Lett. **97**, 192104 (2010).

Spin-dependent dynamics of polaron pairs in organic semiconductors
D. R. McCamey, S.-Y. Lee, S.-Y. Paik, J. M. Lupton, and C. Boehme
Phys. Rev. B **82**, 125206 (2010).

Hyperfine-field mediated spin beating in electrostatically-bound charge carrier pairs D. R. McCamey, K. J. van Schooten, W. J. Baker, S.-Y. Lee, S.-Y. Paik, J. M. Lupton, and C. Boehme
Phys. Rev. Lett. **104**, 017601 (2010).

Pulsed electrically detected magnetic resonance in organic semiconductors
C. Boehme, D. R. McCamey, K. J. van Schooten, W. J. Baker, S.-Y. Lee, S.-Y. Paik, J. M. Lupton
Phys. Stat. Sol B. **246**, 11-12, 2750 (2009).

Spin-Rabi flopping in the photocurrent of a polymer light-emitting diode
D. R. McCamey, H. A. Seipel, S. -Y. Paik, M. J. Walter, N. J. Borys, J. M. Lupton and C. Boehme

Nature Materials, **7**, 723 (2008).

Understanding the modulation frequency dependence of continuous wave optically/electrically detected magnetic resonance
Sang-Yun Lee, Seoyoung Paik, Dane R. McCamey, and Christoph Boehme (2011).
submitted for publication (2011).